POLITECNICO DI TORINO

Corso di Laurea Magistrale
in Ingegneria Aerospaziale

Tesi di Laurea Magistrale

Effect of porosity on the wall-pressure fluctuations on a wing profile immersed in a turbulent flow

***Relatore*:**
Prof. Renzo Arina

***Candidata*:**
Martina Spadon

***Correlatori*:**
Prof. Domenic D'Ambrosio
Prof. Christophe Schram
Dr. Riccardo Zamponi

Anno accademico 2019/2020

VON KARMAN INSTITUTE
FOR FLUID DYNAMICS

Chaussée de Waterloo, 72
B-1640 Rhode Saint Genèse - Belgium

Short Training Report 2021

Effect of porosity on the wall-pressure fluctuations on a wing profile immersed in a turbulent flow

M. Spadon

Supervisor: C. Schram
Advisor: R. Zamponi

April 2021

A mamma e papà,
per avermi insegnato a non mollare mai.

Acknowledgments

First of all, I would like to warmly thank my advisor Riccardo Zamponi for the constant support and the immense willingness provided during all these months, from the first to the last day. His passion and his commitment have been for me a source of inspiration and determination in pursuing goals without ever giving up. Even when things were not going right, he always continued to believe in me and in my abilities: the understanding and encouragement received at that moment made me realize that I was very lucky to be able to work with him. I could not have found a more valid person to accompany my STP and I am really grateful to him for everything.

I would like to dedicate a heartfelt thanks to prof. Christophe Schram for his valuable advice and for the engaging enthusiasm shown during the aeroacoustics team meetings, despite being done online due to health restrictions. A special mention also goes to Simone Tamaro, who helped me to approach the experimental activity thanks to his previous experience.

Then, I would like to thank prof. D'Ambrosio who first believed in my academic background, supporting me in applying for this experience abroad: because of the way he interfaces with students, I felt he was the most suitable teacher to put my trust on. Last but not least, I would like to express my deep gratitude to prof. Arina for having accepted to be the supervisor of this thesis, despite there was no way to meet us in person.

Prima di procedere con la trattazione, vorrei dedicare qualche riga a tutti coloro che mi sono stati vicini in questo percorso di crescita personale e professionale.

In primis, vorrei ringraziare infinitamente i miei genitori per avermi dato la possibilità di proseguire gli studi e per aver sempre creduto in me. Non c'è stato momento in questi cinque anni in cui io non abbia sentito il vostro amore, il vostro sostegno e la vostra partecipazione. Avete condiviso con me gioie, delusioni, ansie e preoccupazioni. Mi avete supportato in ogni scelta, giusta o sbagliata che fosse, e mi avete sopportato durante tutte le sessioni d'esame, anche se sono certa che vi mancherà sentire la mia voce soave ripetere formule e concetti in giro per casa. Nonostante la mole di studio, ho cercato di impegnarmi sempre al massimo non solo per me, ma anche e sopratutto per voi e sentirvi così vicini mi ha dato la giusta forza e determinazione per superare ogni difficoltà. In particolare, ringrazio mia mamma per essere la donna più buona, più generosa e più forte che io conosca: spero che questo giorno importante possa regalarti un po' della serenità che ti meriti. Dedico un pensiero particolare al mio papà, che oggi più che mai avrei voluto avere al mio fianco pronto a battermi il cinque: io ho rispettato la previsione della laurea ad aprile, tu potevi aspettare ancora un po' che ora mi tocca aprire la bottiglia di spumante da sola. So quanto avete investito su di me e sul mio futuro in questi anni e quanta fiducia avete riposto nei miei confronti: mi avete insegnato che i sacrifici prima o poi vengono ricompensati e spero che questo traguardo possa ripagare una parte di tutto quello che avete fatto per me. Siete il mio esempio.

Allo stesso modo, un doveroso grazie alla mia bellissima famiglia sparsa per tutta Italia. Nonostante la distanza che in questo periodo si fa sentire ancora più forte, mi ritengo davvero fortunata ad avere zii e cugini che mostrano il loro affetto e il loro appoggio anche con un semplice messaggio. Ero così contenta all'idea di riunirvi tutti in occasione della mia laurea per passare un po' di tempo insieme, ma purtroppo tocca rimandare i festeggiamenti a un momento migliore: so comunque che sarete con me con il cuore e non potrei desiderare nulla di più.

Vorrei ringraziare enormemente la mia migliore amica Sabrina, che senza ombra di dubbio è una delle persone più importanti della mia vita. Le parole non bastano a spiegare quello che tu rappresenti per me: sei il mio punto di riferimento, la mia confidente, la mia prima sostenitrice. Hai dimostrato in questi anni un'infinita pazienza che con me è oltremodo necessaria, mi hai sempre fatto ragionare mettendo un freno alla mia impulsività e non ti sei mai limitata nel dirmi come la pensavi realmente. Su molti aspetti sei l'esatto contrario della mia persona e proprio per questo non posso fare a meno della tua amicizia, perchè completi quelle mie mancanze che altrimenti rimarebbero tali. Non abbiamo bisogno di sentirci ogni giorno e non dobbiamo ripeterci ogni tre per due quanto ci vogliamo bene, ma sappiamo entrambe che per qualsiasi cosa ci saremo sempre l'una per l'altra. Grazie di cuore mia dolce Trallallà!

Vorrei continuare ringraziando Sara, Ilaria e Laura per le risate e la spensieratezza che mi hanno regalato da quando ci conosciamo. Nonostante i cambiamenti, siete rimaste nel tempo colonne portanti della mia quotidianità su cui fare completo affidamento per un semplice consiglio o per un momento di leggerezza. Vi ringrazio per la semplicità e per i piccoli gesti con cui mi dimostrate il vostro affetto e la vostra vicinanza: non abbiamo bisogno di effetti speciali o occasioni particolari, sono sufficienti del buon vino e qualche puntata di Temptation Island per passare insieme una piacevolissima serata e aggiornarci sulle ultime novità. Siete davvero uniche e credo tanto nell'amicizia che abbiamo costruito.

Inoltre, vorrei ringraziare di vero cuore due persone speciali che hanno continuato a camminare al mio fianco in questi anni. La prima è Amalia che, inconsciamente, fin dalle scuole medie ha deciso di riporre la sua fiducia in me facendosi trasportare nel magico mondo della pallavolo. Come ci siamo dette dopo quella videochiamata infinita, anche senza sentirci spesso non ci perdiamo mai perchè la nostra amicizia ha fondamenta talmente solide da non poter essere abbattuta facilmente. Se neanche i perenni ritardi per arrivare al Poli hanno scalfito il nostro rapporto, significa che siamo a prova di bomba! La seconda è Rebecca, capace di trasmettere la sua energia e simpatia a tutti quelli che la circondano. Sei un vero e proprio raggio di sole e ti ringrazio per la ventata di positività e umorismo che ogni volta porti con te. Te vojo bene, core.

Ya que dos idiomas no eran suficientes, me gustaría agradecer a mi pequeñita Alba por estar tan presente en mi vida que parece tenerla a mi lado en cada momento. Si pudiera teletransportarme a Granada de vez en cuando sería más fácil, pero nuestra amistad sigue siendo la misma a pesar de la distancia. Siempre estás lista para escuchar mis audios sin fin y darme valiosos consejos sobre cualquier tema: eres una amiga fantástica, con quien estoy feliz de compartir fragmentos de mi vida. Gracias por todo, te quiero un montón preciosa.

Non posso che essere grata a questi cinque anni di università per avermi fatto incontrare delle persone stupende, che da semplici colleghi sono diventati veri e propri amici. Ringrazio Enza, Riccardo, Federico, Fabio, Mario, Giuseppe, Alessia, Elisa, Pierangela, Edoardo, Daniel e Fabiano per le risate in aula, per i caffè al volo nel cambio d'ora, per i pranzi all'aperto, per gli intensi pomeriggi di studio, per i meme divertenti sul gruppo whatsapp e per le serate indimenticabili al Borsellino. Abbiamo condiviso ogni istante di questo percorso e ci siamo supportati a vicenda in ogni difficoltà, facendoci coraggio l'un l'altro per andare avanti e raggiungere prima o poi il traguardo finale. Siete stati la mia ancora di salvezza in questo mare di disperazione e fatica, ma il forte legame che ci unisce rappresenta sicuramente la parte più bella di questo percorso. Purtroppo non l'abbiamo concluso insieme come volevamo e la distanza geografica non aiuterà a mantenere lo stesso rapporto coltivato in questi anni, ma sono sicura che non appena ci sarà occasione riusciremo a ritrovarci sempre. Non voglio fare distinzioni perchè ognuno di voi ha lasciato un segno importante, ma è necessario un ringraziamento particolare al mio compagno di disagio Riccardo per aver condiviso in tutto e per tutto l'esperienza di studio in Belgio: non sto qua a ripetere quello che ti ho già detto e scritto, ma sei stato davvero un amico eccezionale e un aiuto fondamentale per questi mesi lontani da casa.

Infine, non posso concludere senza ringraziare la family Zanellato per tutto quello che abbiamo condiviso in questi anni: dai sabato sera a casa alle grigliate in montagna, dai capodanni insieme alle gite fuori porta. Siete proprio gli amici di una vita di cui parlano nei film e sono contenta di poter contare sempre su di voi. Anche oggi, penso si possa esclamare "è una bellissima giornata".

Abstract

The turbulence impinging on an airfoil generates aeroacoustic noise, also referred to as leading-edge noise, which plays an important role in industrial sectors such as wind energy, aviation and cooling/ventilation. For its mitigation, one of the proposed solutions involves the integration of porous materials into the structure of the wing profile. Since the physical mechanisms responsible for the noise reduction have not been defined yet, the aim of this work is to investigate how porosity affects the surface-turbulence interaction and the evolution of the wall-pressure fluctuations radiating into the far-field to provide new information for a better understanding of this phenomenon.

The investigation is performed by post-processing large-eddy simulations data that have been provided by a group of researchers from the RWTH Aachen University: these data are based on an experimental setup already implemented at VKI, which involves the comparison between a porous NACA-0024 profile equipped with melamine foam and an identical solid configuration, both subjected to a turbulent flow generated by an upstream circular rod. Wall-pressure fluctuations are reduced by up to 6 dB along the porous surface, particularly just downstream of the stagnation point, and flow structures show less spanwise coherence than the solid design. Results of the power spectral densities (PSDs) indicate an attenuation of the pressure and velocity fluctuations in the porous model, which mainly affects the low-frequency range. The most important result comes from the calculation of surface-normal velocity, whose PSD shows for the porous case a similar reduction of the wall-pressure fluctuations in the same frequency range: this correspondence demonstrates that the attenuation of turbulence distortion due to porosity is one of the mechanisms associated with leading-edge noise reduction, at least for thick airfoils.

For the experimental validation, a fast and in-situ calibration procedure for microphones embedded on the surface of both solid and porous airfoils has been designed and implemented to investigate how the wall-pressure fluctuations are affected by porous media. The results are promising in terms of repeatability, but require further investigations in order to be used for quantitative analysis.

Contents

List of Figures

List of Tables

List of Symbols

Acronyms

AUSM	Advected Upstream Splitting Method
B&K	Bruel & Kjaer
CAA	Computational Aeroacoustics
CAD	Computer-Aided Design
CPSD	Cross Power Spectral Density
ESA	European Space Agency
fft	Fast Fourier Transform
LES	Large-Eddy Simulation
NACA	National Advisory Committee for Aeronautics
NATO	North Atlantic Treaty Organization
PIV	Particle Image Velocimetry
PSD	Power Spectral Density
RDT	Rapid Distortion Theory
RWTH	Rheinisch-Westfälische Technische Hochschule
TF	Transfer Function
TI	Turbulence Intensity
TKE	Turbulent Kinetic Energy
VANS	Volume Averaged Navier-Stokes equations
VKI	von Karman Institute
VPP	Peak-to-Peak Voltage

Roman symbols

a	Speed of sound	[m s^{-1}]
c	Airfoil chord	[m]
c_F	Forchheimer coefficient	[-]
d	Rod diameter	[m]
Da	Darcy number	[-]
f	Frequency	[Hz]
F	Porous drag	[N]
G_0	Free-field Green's function	[-]
k	Permeability	[m^2]
L	Reference length	[m]
M	Mach number	[-]
n	Surface-normal vector	[-]
p	Pressure	[Pa]
r_{LE}	Leading-edge radius	[m]
R	Causality correlation coefficient	[-]
Re	Reynolds number	[-]
S	Fluid-domain surface	[m^2]
St	Strouhal number	[-]
t	Time	[s]
t^*	Retarded time	[s]
T_{ij}	Lighthill's stress tensor	[Pa]
u	Streamwise velocity component	[m s^{-1}]
U	Flow velocity	[m s^{-1}]
v	Upwash velocity component	[m s^{-1}]
V	Surface-normal velocity component	[m s^{-1}]
w	Spanwise velocity component	[m s^{-1}]
x	Streamwise coordinate	[m]
y	Upwash coordinate	[m]
z	Spanwise coordinate	[m]

Greek symbols

α	Tortuosity	[-]
γ	Ratio of specific heats	[-]
γ^2	Spatial coherence	[-]
Γ_2	Vortex core identification function	[-]
δ_{ij}	Dirac delta function	[-]
θ	Angle between U and the tangent to the airfoil	[rad]
μ	Dynamic viscosity	[kg m^{-1} s^{-1}]
ρ	Density	[kg m^{-3}]
σ	Static air flow resistivity	[Pa s m^{-2}]
τ	Time shift	[s]
τ_{ij}	Viscous stress tensor	[Pa]
ϕ	Wall-pressure fluctuations phase	[rad]
φ	Porosity	[-]
Φ_{pp}	Cross power spectral density function	[Pa^2 Hz^{-1}]
ω	Vorticity	[s^{-1}]
Ω	Fluid-domain volume	[m^3]

Subscripts and superscripts

$'$	Referred to the fluctuations around the mean value
$^-$	Referred to the mean value
$_0$	Referred to the stagnation point
$_\infty$	Referred to the free-stream conditions
$_{ref}$	Referred to the reference microphone
$_{rms}$	Referred to the root mean square
$_s$	Referred to the sampling parameters
$_z$	Referred to the direction of the z axis

Chapter 1

Introduction

1.1 Document outline

The present document constitutes the Master's Degree thesis of the Aerospace Engineering course attended at the Politecnico di Torino. The entire work has been carried out at the von Karman Institute for Fluid Dynamics (VKI), in Rhode-Saint-Genèse near Brussels, during the internship period which lasted four months. The main purpose has been to evaluate the benefits of porosity on the reduction of the aeroacoustic noise, produced by the interaction between a turbulent flow and the leading-edge of an airfoil. The study is based on the post-processing of numerical data from Large-Eddy Simulations (LES), analyzed using the MATLAB software. A second part describes the methodology implemented at the VKI, to reproduce and experimentally investigate the same phenomenon: unfortunately, this part of the work has not been completed due to the second European lock-down, linked to the ongoing Covid-19 health emergency.

The present document is divided into five main parts, in the following order:

1. This first chapter briefly introduces the main topic of the thesis, contextualizing the aim of the work concerning the phenomenon of turbulence-interaction noise and the problems encountered so far.

2. The second chapter focuses on the theoretical background behind the generation of leading-edge noise and the use of porous materials as a possible strategy to mitigate this disturbance. Previous studies are presented to explain which aspects are already known and which are the limitations to overcome. Furthermore, the methodologies used for the LES and the laboratory experimentation are mentioned.

3. The third chapter collects all the results obtained from the post-processing of numerical data. The analysis of wall-pressure fluctuations confirms a sig-

nificant reduction for the porous case, which is reflected in the leading-edge noise mitigation. From the calculation of the surface-normal velocity fluctuations, however, a similar attenuation is observed in the same frequency range of the pressure and this leads to confirm that the different turbulence distortion, due to porosity, constitutes one of the noise reduction mechanisms.

4. The fourth chapter concerns the laboratory activity and, in particular, shows the results obtained from the calibration of the microphones installed on the airfoil model. This is an experimental configuration designed and implemented at the VKI, on which the numerical simulations are based and that would be useful for the experimental verification of the theoretical results.

5. The last chapter summarizes the conclusions drawn from the results of numerical post-processing and those of the calibration chain, as well as providing some ideas for future studies and developments.

1.2 Aim of the present work

In recent years, the study of aeroacoustics has become one of the fundamental topics in the field of aeronautical engineering given the increasing problem related to noise pollution. As a result of the enhancement in air traffic, near the airports, an unbearable noise is complained of due to aircraft approaching and departing from the runway. Furthermore, stricter regulations have been issued on the design of new aircraft to reduce noise emissions by 50% in the coming years. The noise produced by the engines, for example, is easily measured in a laboratory but finding a solution to this problem is not immediate, until the acoustic source is identified. The challenge becomes more complicated when the noise is aerodynamically produced by the interaction between the airflow and a body, such as the wing of an airplane: in this case, the noise production mechanism is known but the problem related to the identification of the sources of unsteady pressure fluctuations is even more evident. For this reason, the aeronautical industries have begun to take an interest in aeroacoustics, developing both numerical and experimental research and tests to simulate the analyzed phenomenon.

It has been verified that a wing profile immersed in a turbulent flow generates aeroacoustic noise, characterized by three different contributions such as unsteady-tip flows that produce the *tip noise*, scattering of boundary layer vortical disturbances linked to the *trailing-edge noise* and turbulence-interaction related to the *leading-edge noise*. The present work focuses only on the turbulence-interaction with the leading-edge of the airfoil, because it constitutes the predominant noise source when the incoming flow is strongly turbulent. In research studies, this sound production mechanism can be achieved in several ways, for example by inserting fixed grids that generate vortical structures once crossed by the flow. In this case, however, the rod-airfoil configuration was chosen, which provides for the arrangement of a cylinder upstream of the wing profile: the incoming air stream surrounds the surface of the rod until separation occurs, which determines periodic extraction of eddies. These eddies constitute the required turbulence and continue downstream up to the airfoil leading-edge. Their interaction is an aeroacoustic noise source that is propagated not only near the body but also in the far-field: the airfoil undergoes a broadband perturbation characterized by a shedding frequency, similarly to what is observed in the acoustic spectra of turbo-machinery applications.

In practical applications, it is not always possible to remove upstream objects that produce turbulence and, therefore, it is necessary to find other solutions that make the acoustic response of the wing profile less sensitive to the turbulence. Different strategies for mitigating the leading-edge noise have been analyzed: the one proposed in this work corresponds to the use of porous media. In previous studies, the application of these materials in the airfoil structure has shown an attenuation of sound radiation, but the physical mechanisms involving this reduction are still not clear. Therefore, the strong interest behind this work is to understand the physics of the leading-edge reduction mechanism.

In order to arrive at a possible explanation of the mitigation phenomenon due to porosity, the trends of the velocity and pressure fluctuations have been analyzed in the stagnation region and along the surface of the airfoil. Numerical simulations are implemented with the same computational setup, but using two airfoils with the same dimensions but different materials: one solid and the other porous. From the data post-processing, it is possible to compare the two configurations to highlight the most significant variations in pressure and velocity. The results obtained from the numerical analysis should also be verified experimentally, reproducing the same rod-airfoil configuration in the wind tunnel. Concerning the velocity, previous articles have reported good agreement between the LES data and the laboratory acquisitions, carried out using the hot wire anemometry technique. Thus, the ultimate goal of the work was to study the flow pressure characteristics through microphones installed on the surface of an airfoil: this is an innovative setup, which requires a daily calibration of the microphones before testing. At the moment, the calibration chain designed at VKI is promising in terms of repeatability and robustness, but the resulting transfer functions do not guarantee yet the proper efficiency to proceed with the tests in the facility.

1.3 The von Karman Institute for Fluid Dynamics

VKI is a non-profit international educational and scientific organization, hosting three departments that are Aeronautics and Aerospace, Environmental and Applied Fluid Dynamics, and Turbomachinery and Propulsion. It provides postgraduate education in fluid dynamics through several offers such as Research Master, Doctoral Program, Short Training Program, and lecture series. Extensive studies on experimental, computational and theoretical aspects of gas and liquid flows are carried out at the von Karman Institute under the direction of the faculty and research engineers, sponsored mainly by governmental and international agencies as well as industries.

VKI has a permanent staff of approximately 106 persons, among them 29 research engineers and 18 professors; moreover, about 190 students and temporary researchers are involved in the different academic programs. It is funded in part by the contributions from 15 NATO countries and these are represented at several levels in the governance bodies of the Institute.

Figure 1.1: The von Karman Institute for Fluid Dynamics.

The von Karman Institute is recognized as a world-class research center of excellence by its peers because it has about fifty different wind tunnels, turbomachinery and other specialized test facilities, which are renowned and in some cases unique. As an example, VKI and the European Space Agency (ESA) have signed a Memorandum of Understanding in November 2011 under which the Institute acts as a reference laboratory for ESA. This agreement involves 10 research staff and more than 20 PhD students in a continuous effort devoted to the present space transportation missions and the challenges of future space explorations. Furthermore, it organizes each year eight to twelve one-week Lecture Series on specialized fluid dynamics topics and these courses have gained over the years worldwide recognition for their high quality.

Chapter 2

Literature review and methodology

2.1 Theoretical background: aeroacoustic analogies

To describe the framework of the proposed study, it is essential to introduce the aeroacoustic analogies that allow to theoretically model the aerodynamic noise generated by the non-linearities of a turbulent flow, which act as acoustic sources that emit into the surrounding space.

2.1.1 Lighthill's analogy

Since in the 1950s the use of turbojet engines on airplanes become more frequent, research studies focused on jet problems, such as the noise raise that occurred by increasing the output speed. Lighthill [28] proposed an acoustic analogy to estimate the sound radiated by a free fluid flow, like a jet. The main idea is to distinguish the source region and the propagation region in the fluid domain Ω to manipulate the Navier-Stokes equations, in order to obtain a formulation that resembles the linearized wave equation: this procedure is useful for applying integral solution methods that involve Green's functions.

The non-homogeneous wave equation, obtained from the linear combination of the Navier-Stokes equations, constitutes the starting point of the theory:

$$\frac{\partial^2 \rho}{\partial t^2} - a_\infty^2 \frac{\partial^2 \rho}{\partial x_i \partial x_j} = \frac{\partial^2}{\partial x_i \partial x_j}\Big(\rho u_i u_j + (p - a_\infty^2 \rho)\delta_{ij} - \tau_{ij}\Big) \tag{2.1}$$

where a_∞ indicates the free-stream speed of sound, δ_{ij} is the Dirac delta function, and τ_{ij} represents the viscous stress tensor. If instead of using the absolute quantities, the fluctuations of the same variables calculated with respect to the reference value that defines a uniform medium at rest are introduced, the following Lighthill's equation is obtained:

$$\frac{\partial^2 \rho'}{\partial t^2} - a_\infty^2 \frac{\partial^2 \rho'}{\partial x_i \partial x_j} = \frac{\partial^2 T_{ij}}{\partial x_i \partial x_j} \tag{2.2}$$

where T_{ij} is defined as Lighthill's stress tensor. This source term fully describes the flow and, in it, all the physical phenomena that contribute to the generation of noise are collected: convection, propagation and refraction of the acoustic signal through the flow, fluctuations dissipation due to viscosity and thermal conduction. From the listener's point of view, the source term T_{ij} is equivalent to the sound produced by a turbulent flow and this concept is the basis of Lighthill's analogy.

To easily solve Equation 2.2, it is necessary to apply the approximation that derives from high-Reynolds number flows: in these cases, the viscous contribution and thermal effects are considered negligible and the Lighthill's stress tensor is reduced to $\rho u_i u_j$. Replacing this simplification, the equation is rewritten in an explicit form that can be solved through the free-field Green's function, obtaining the far-field acoustic fluctuations induced by the non-linear term:

$$a_\infty^2 \rho'(\mathbf{x}, t) = \frac{\partial^2}{\partial x_i \partial x_j} \int_\Omega \frac{T_{ij}}{4\pi |\mathbf{x} - \mathbf{y}|} \, d\Omega \tag{2.3}$$

The result of this study is that, when the flow is incompressible (i.e. at low Mach number), free isentropic turbulent flows without solid bodies can be described as a quadrupolar source.

2.1.2 Curle's analogy

Lighthill's analogy cannot be immediately applied to a wing profile, since it does not consider the presence of solid boundaries or surfaces within the fluid domain. Curle [10] proposed an extension of this analogy to include their effects, such as reflection and diffraction. By indicating with S the solid surface present in the control domain and with n its normal direction, the solution of Lighthill's equation, in this case, is modified as:

$$a_\infty^2 \rho'(\mathbf{x}, t) = \int_{-\infty}^{+\infty} \int_\Omega \frac{\partial^2 T_{ij}}{\partial y_i \partial y_j} G_0 \, d\Omega d\tau + \int_{-\infty}^{+\infty} \int_S \left(G_0 \frac{\partial \rho'}{\partial y_i} - \rho' \frac{\partial G_0}{\partial y_i} \right) n_i \, dS d\tau \tag{2.4}$$

The two terms on the right-hand side represent respectively the incident acoustic field and the one generated by the response and vibration of the solid surface.

In order to write Curle's formulation, first it is necessary to integrate by parts the volume integral and then use the definition of the T_{ij} tensor and the momentum conservation law:

$$\begin{aligned} a_\infty^2 \rho'(\mathbf{x},t) = &\int_{-\infty}^{+\infty} \int_\Omega T_{ij} \frac{\partial^2 G_0}{\partial y_i \partial y_j} \, d\Omega d\tau \\ &- \int_{-\infty}^{+\infty} \int_S G_0 \frac{\partial \rho u_i}{\partial \tau} n_i \, dS d\tau \\ &- \int_{-\infty}^{+\infty} \int_S (p\delta_{ij} - \tau_{ij} + \rho u_i u_j) \frac{\partial G_0}{\partial y_j} n_i \, dS d\tau \end{aligned} \tag{2.5}$$

At this point, to complete the discussion, the free-field Green's function is replaced and the time integrals are removed evaluating the density fluctuations at the retarded time t^*. The final result is Curle's solution for an incompressible and isentropic flow:

$$\begin{aligned} a_\infty^2 \rho'(\mathbf{x},t) = &\frac{1}{4\pi a_\infty^2 |\mathbf{x}|} \frac{x_i x_j}{|\mathbf{x}|^2} \frac{\partial^2}{\partial t^2} \int_\Omega [T_{ij}]_{t^*} \, d\Omega \\ &- \frac{1}{4\pi |\mathbf{x}|} \frac{\partial}{\partial t} \int_S [\rho u_i n_i]_{t^*} \, dS \\ &- \frac{1}{4\pi a_\infty |\mathbf{x}|} \frac{x_j}{|\mathbf{x}|} \frac{\partial}{\partial t} \int_S [(\rho u_i u_j + p\delta_{ij} - \tau_{ij}) n_i]_{t^*} \, dS \end{aligned} \tag{2.6}$$

It is immediately observed that the solution consists of three terms: the first with the T_{ij} tensor corresponds to the same result obtained for Lighthill's analogy, the second identifies the flow rate that crosses the surface and the third represents the pressure variations on the body. From their formulations, these terms are respectively a quadrupolar, a monopolar, and a dipolar source.

For a rigid and impermeable surface, the no-slip condition is valid and the wall velocity is equal to zero. Therefore, in the present discussion, the contribution of the monopole is neglected, since the velocity u_i appears in the term. The acoustic field in a medium at rest is reduced to the sum of the volume integral with the Lighthill's stress tensor, which represents the noise production that occurs in absence of the body, and the distribution of dipoles that reflects the fluctuating forces acting on the fluid. Lastly, the surface integral can be assumed as a compact dipole if the solid body is acoustically compact: this implies that, at low Mach numbers, the quadrupole contribution is negligible and the dipolar source is predominant in the sound field.

2.2 Turbulence-interaction noise

The turbulence-interaction noise is generated by the rapid distortion of vortex structures when they interact with the surface of a body. The result of this interaction is a partial conversion of kinetic energy into sound and, in particular, its greatest effect occurs near singular points on the surface, such as corners or sharp curvatures [38]. This form of noise affects several industrial sectors in the engineering field such as civil, automotive and aerospace: wind turbines, cooling/ventilation systems and aircraft are all devices that must often operate with turbulent airflows. For this reason, research concerning the causes of aeroacoustic noise production has increased significantly in recent years, leading to even more complete and accurate results.

As mentioned in the introductory chapter, concerning an airfoil, the turbulence-interaction noise becomes predominant when the incoming flow is characterized by strong turbulence. In this case, it is also called leading-edge noise because, given the significant curvature, the leading-edge constitutes the region where the variation of the vortex inertia occurs. For this type of application, Amiet's theory [2] represents the first fundamental study on the sound generation mechanism: he proposed a prediction method for the far-field acoustic power spectrum of an airfoil immersed in a subsonic turbulent flow. The two parameters that the author identified as the main contributions to the total sound pressure level in the far-field are the spanwise correlation length and the integral length scale of the upwash turbulent-velocity fluctuations.

One of the earliest experimental works about the leading-edge noise came from the results achieved by Paterson and Amiet [35], who measured the surface pressure fluctuations on a NACA-0012 wing profile and the emitted far-field noise. The authors aimed to obtain experimental data in order to validate the prediction models available at that time. In this case, to create the incoming turbulent flow, the airfoil model was installed downstream of a turbulence grid and the surface and far-field data were acquired simultaneously. In addition to verifying that the leading-edge region constitutes the dominant source of the aeroacoustic noise, they concluded that to accurately predict the turbulence-interaction noise it is necessary to know the turbulence properties and the spanwise cross-spectrum of the velocity fluctuations normal to the airfoil.

Olsen and Wagner [34] tested the influence of thickness on the leading-edge noise, placing wing profiles with different shapes in the turbulent mixing region of a jet. The results obtained from the analysis of the measurements showed an important reduction of the sound pressure levels as the airfoil thickness increased, especially at high frequencies. A similar experimental investigation was carried out by Oerlemans and Migliore [33], who focused on the acoustic fields produced by several wind turbine airfoils with different shapes. The results demonstrated that in absence of inflow turbulence the trailing-edge noise is dominant in the far-field frequency spectrum, whereas the contribution of the leading-edge noise becomes preponderant for all airfoils when a turbulence grid is installed upstream in the test section. Moreover, the authors observed that the sound emission increased as the thickness of the wing profile model decreased.

Moreau et al. [31] proposed an experimental analysis of noise generation by comparing the far-field spectra and the unsteady response function of three different bodies: a flat plate, a controlled-diffusion airfoil and a NACA-0012 profile interacting with a turbulent flow, generated by an upstream turbulence grid, were studied to evaluate the effect of the angle of attack and the body shape. Their results confirmed Olsen and Wagner's findings by recognizing the relevant role of thickness, which once again caused the noise reduction at high frequencies; on the contrary, variations in the angle of attack and camber were found to have limited effects. Another experimental work that comes to the same conclusions just explained was carried out by Devenport et al. [13], who tested three different airfoil models in an anechoic facility equipped with a turbulence grid in order to analyze the effect of thickness, camber and angle of attack. Also, in this case, the thickness represents the most influential parameter on the reduction of the high-frequency sound emitted, even when the ratio between the integral length scale and the maximum thickness is high.

The influence of an airfoil shape on the leading-edge noise was also numerically investigated by Gill et al. [16], using a high-order Computational Aeroacoustics (CAA) methodology to solve the acoustic field around wing profiles with various geometries at zero angles of attack. The results indicated that the stagnation region is the area where the dominant noise generation mechanisms occur. As the airfoil thickness increases, the extension of this region enhances and this implies that the turbulence distortion phenomenon also affects a wider area. This aspect reduces the gradient of the upwash velocity fluctuations in the stagnation region, which according to the authors is an important contribution towards the emitted sound attenuation at high frequencies. Similarly, Kim et al. [23] also analyzed with a numerical method the noise produced by the interaction between a symmetrical wing profile and the homogeneous and isotropic incoming turbulence. As with previous studies, also in this case the acoustic power levels showed an important decrease in the high-frequency range when the airfoil thickness increased, but this attenuation was reduced to higher free-stream Mach numbers: the explanation is given by the greater contribution of streamwise velocity fluctuations to the radiating sound pressure level.

To have an accurate prediction of the leading-edge noise when the airfoil exceeds a certain thickness, it is important to know the effective distortion suffered by the eddies interacting with the surface [12, 31]. Based on the work of Batchelor and Proudman [36], Hunt [21] formulated a theory capable of estimating the turbulence distortion around wing profiles with a non-negligible thickness, called Rapid Distortion Theory (RDT). It was formulated thanks to the author's calculations performed for a turbulent flow around a circular cylinder: he obtained an estimation of the velocity spectra in the particular case of turbulence scale smaller or larger than the characteristic size of the body. This analytical tool could only be applied if the characteristic time of viscous dissipation and inertial forces is greater than that taken by the fluid particle to be moved through the non-uniform flow region. Furthermore, the intensity of turbulent velocity fluctuations must be small to not affect the free-stream flow conditions. Bearman [6] carried out one of the first experimental studies to verify the RDT validity, reproducing the turbulence distortion mechanism that occurs in the stagnation region of a two-dimensional bluff body. More recently, de Santana et al. [12] performed experimental measurements with a NACA-0012 wing profile to investigate the distortion of the vortex structures responsible for the leading-edge noise. The investigation, developed using the Particle Image Velocimetry (PIV) technique, showed that the area affected by the distortion extends around the stagnation point with a dimension of the order of its radius of curvature. Moreover, the turbulence intensity increases significantly as the flow approaches the leading-edge of the airfoil.

2.3 Porous materials for noise mitigation

In order to reduce the turbulence-interaction noise, it is necessary to adopt a specific strategy that makes the surface of the body less sensitive to local vortex disturbances, since it is not always possible to change the intensity of the incoming turbulence. In the present study, the use of porous materials within the airfoil structure is presented as a possible solution, analyzing the extent of the noise reduction in the acoustic spectrum. The idea of applying porous materials to mitigate leading-edge noise has already been examined in recent years and derives from Kroeger's studies [25] on the silent flight of owls. He identified the peculiar feather structure that characterizes the trailing-edge of the owl wings with the term *wing porosity* and classified it as one of the mechanisms responsible for their silent flight.

The implementation of porous media on the airfoil configuration has been treated both numerically and experimentally with successful results. The first to demonstrate its beneficial effects was Lee [27], who numerically analyzed the noise generated by a helicopter blade with a porous leading-edge insert. Comparing the obtained acoustic spectrum with that of a normal solid profile, he observed that the reduction of the emitted sound reached 30% due to the suppression of the wall-pressure fluctuations. Geyer et al. [14] made acoustic measurements on solid and porous airfoils installed downstream of a turbulence grid, using the microphone array technique. Several grids were tested to obtain different inflow conditions and numerous materials were used to design the models: their main purpose was to highlight the influence of the properties of the porous materials on the amount of noise reduction. They observed that static air-flow resistivity was the most influential parameter and the lower its value, the more significant was the attenuation experienced especially at high frequencies. Subsequently, Sarradj and Geyer [41] tried to describe the noise generation for porous airfoils using empirical models based on the tool of symbolic regression. The results showed that the leading-edge noise power was proportional to the square of the turbulence intensity and depended on the fifth to the sixth power of the flow velocity; moreover, the acoustic frequency spectrum was governed by the static air-flow resistivity and the integral length scale of the incoming turbulence.

With the numerous studies carried out over the years, it has been observed that the use of porous materials within the airfoil structure causes a worsening of aerodynamic performance: especially at high angles of attack, lift tends to decrease because the partial penetration of the flow through the internal porosity allows the communication between pressure and suction sides, while the drag seems to increase due to the higher surface roughness compared to the solid case. Sarradj and Geyer [40] came to these conclusions by exposing six airfoil models to a jet flow in an anechoic chamber with no turbulence generators. The authors remarked on the strong deterioration of aerodynamic characteristics experienced by porous airfoils and they observed that porous materials with a high flow resistivity resulted in lower loss of lift without excessively increasing the drag.

Since the main goal of the research is to propose solutions that can one day be implemented in reality, the same aerodynamic performance must be maintained even on a wing profile with porous inserts. Several solutions have been proposed over the years: for example, Roger and Moreau [39] tested a NACA-0012 model filled with steel wool in both grid-airfoil and cylinder-airfoil configurations. A specific design was defined for the porous model by inserting a center plate along the chord line to preserve the aerodynamic properties and a wire mesh to reduce the surface roughness. The results showed significant reductions of the sound pressure level in the far-field up to 6 dB at low frequencies, which was the range linked to the characteristic length of the porous medium; on the contrary, porous treatment is not as effective at mitigating the leading-edge noise at high frequencies. Another similar strategy, proposed by Bampanis and Roger [5], involved NACA-0012 airfoil models designed as a rigid exoskeleton covered with a metal wire mesh and filled with porous materials, which in this case were melamine foam or metal wool. Always to avoid cross-flow between the pressure and suction side of the wing profile, a solid center plate was inserted with variable internal extension according to the different versions. The authors observed from the acoustic spectra that the noise attenuation varied between 4 and 6 dB.

Geyer et al. [15] carried out a numerical and experimental investigation to reduce the turbulence-interaction noise of axial fans, using airfoil models where the solid leading-edge is perforated to create porosity. The results showed a noticeable noise attenuation up to 8 dB in the frequency range between 1 kHz and 4 kHz, but for leading-edges with large pores additional high-frequency noise is generated due to the increased surface roughness. Moreover, the increase in the angle of attack of the porous airfoil leads to greater deterioration of the aerodynamic performance. To mitigate the sound emitted by the interaction between a pylon and a propeller slipstream, Avallone et al. [3] and Sinnige et al. [43] proposed in their studies the installation of a flow-permeable leading-edge on the pylon as an alternative design solution. The velocity spectra showed a 35% reduction for the fluctuations near the surface of the flow-permeable structure, while a lower tonal noise emission from the pylon was measured in the far-field, as a consequence of the decrease in the wall-pressure fluctuations.

Among the most recent studies on how porosity is integrated to achieve the best noise reduction efficacy, the following are the most interesting for the results obtained. Chaitanya et al. [9] experimentally compared the turbulence-interaction noise generated by three different configurations of a porous flat plate, identifying which one produced the greatest attenuation: between the fully porous flat plate, the one with only the leading-edge in porous materials, and the one on which the porous insert was installed downstream of the leading-edge this last solution proved to be the best. A single row of holes downstream of the airfoil leading-edge provides a relevant low-frequency noise mitigation without increasing the radiated noise at higher frequencies. Ayton et al. [4] carried out a numerical investigation on the advantages given by the implementation of smoothly varying chordwise porosity on a finite perforated plate. The authors measured a lower trailing-edge noise for the airfoil where porosity continuously decreased from the trailing-edge towards the leading-edge, instead of keeping its value constant along the entire airfoil. This beneficial effect, given by the progressive variation of porosity, is due to the more intense destructive interference of the back-scattered vortical disturbances generated by a solid leading-edge compared to the porous one [32, 37].

Although all the studies presented above show the promising results obtained from the use of porous materials as a turbulence-interaction noise mitigation technique, a definitive explanation of the physical mechanism behind this reduction has not been formulated yet. A better understanding would allow to clarify some unsolved aspects and improve the design of porous airfoils, which could be used in future industrial contexts. Therefore, the main goal of the present investigation is to improve the current knowledge of the physics involved and overcome the limitations encountered so far: the reference work, which constitutes the starting point for the analysis proposed in this document, will be presented in the next section.

2.4 Methodologies

As explained in Section 2.3, the research and studies carried out in recent years have demonstrated the potential of porous materials in reducing the turbulence-interaction noise, but the physical criterion that explains this beneficial effect has not been found yet; at the moment, two hypotheses have been advanced about the mitigation mechanism. The first reason is based on the fact that the sound propagation in the air is due to the transfer of energy through molecular collisions: when the molecules interact with a solid surface, they are backscattered generating new acoustic waves, while penetrating in the pores of a permeable body they dissipate this acoustic energy by the viscous and thermal losses [26]. The second one is linked to the hydrodynamic absorption experienced by the vortical structures when they interact with a porous surface: the turbulence distortion, responsible for the leading-edge noise, could be influenced by this aspect, causing a reduction in the radiated sound.

The study reported in the present document focuses on the deepening of this second mechanism and constitutes the continuation of the investigations carried out by Zamponi et al. [49] and Satcunanathan et al. [42]. The two separate works compared experimentally and numerically a solid and a porous airfoil, both subjected to the turbulence shed by an upstream circular rod. In both cases, the results showed an alteration of the mean velocity field and a reduction of velocity fluctuations in the vicinity of the airfoil leading-edge, due to the porous treatment. Moreover, from the acoustic far-field measurements obtained using the inverse beamforming technique, an attenuation of about 4 dB in the low-frequency range was observed for the porous configuration, contrary to what occurs at high frequencies where the sound emitted increases probably due to the higher surface roughness. Both studies left open the discussion on the choice of porous materials for the turbulence-interaction noise mitigation, suggesting the possibility of varying the characteristic parameters to find the best solution. Besides, each work required confirmation from the missing numerical or experimental part, respectively.

From the collaboration between these authors, a more complete overview of the examined phenomenon is obtained. Starting from the limitations mentioned above, Zamponi et al. [50] performed further experiments in order to add information on the porosity effects on the turbulence distortion. The study aimed to analyze the motion field around a NACA-0024 profile immersed in a turbulent flow, both in the solid and porous configuration: the investigation consists of an experimental and a numerical part, both based on the rod-airfoil setup implemented at VKI. The porous airfoil model was designed using melamine foam inside the structure together with a solid centerplane, to avoid alterations in the aerodynamic performance. The results of the experimental investigation, carried out using the hot wire anemometry technique, showed significant variations of the fluctuating velocity field in the stagnation region. However, these alterations only occurred at low frequencies and the power spectra, obtained from the numerical data of the large-eddy simulations, confirmed the same trend as the experimental ones. Besides, an important reduction in the far-field noise was observed in the same frequency range, as evaluated by the beamforming measurements. This aspect led the authors to conclude that the flow penetration inside the porous material influenced the distortion of the larger eddies: by applying the RDT, the difference in turbulence distortion due to porosity was interpreted as less efficient conversion of vortical energy into sound.

According to the hypothesis of Zamponi et al. [50], the variation of turbulence distortion can constitute one of the leading-edge noise reduction mechanisms due to porous treatment. The differences in velocity fluctuations, found in the stagnation region between the two configurations, demonstrate that the turbulence distortion phenomenon is attenuated in the case of the porous airfoil. To state that this aspect represents the physical mechanisms underlying noise reduction, first it is necessary to measure the unsteady wall-pressure fluctuations and verify that they are mitigated in the same frequency range as the velocity. Therefore, the lack of a link between the attenuation experienced by these two quantities is the most important limitation of this work.

Another unclear aspect of this investigation is related to Curle's analogy. Equation 2.6, which represents the source terms of the aeroacoustic noise, in the case of a solid airfoil is simplified to the single distribution of dipoles on the surface since the body can be assumed to be acoustically compact and its wall velocity is zero. With the introduction of porosity, the non-penetration condition is no longer respected and the velocity on the surface is not canceled. Therefore, it should be verified whether the contribution of the monopolar source is negligible or not. Moreover, knowing the pressure distribution, it would also be possible to identify the exact position of the dipoles along the surface depending on the point where the fluctuations are maximum. Unfortunately, these two additional issues could not be studied here and remain interesting starting points for future works.

The present study assumes as its reference the work of Zamponi et al. [50] and constitutes its continuation, overcoming some limitations and expanding the results obtained previously. The investigation is again made up of a numerical and an experimental part: the former is based on a new LES campaign, which provides also the pressure data on the airfoil surface, and on their post-processing, while the latter involves the development of innovative technology for the experimental measurements of the wall-pressure fluctuations. Both methodologies used here are described more carefully in the following sections.

2.4.1 Experimental evaluation of wall-pressure fluctuations

The essential aeroacoustics studies, introduced in Section 2.2, have underlined the importance of the unsteady wall-pressure fluctuations to characterize the acoustic properties of a body immersed in a turbulent flow. Indeed, if for the numerical analysis the pressure data are provided by the LES, this is the main motivation behind the experimental part of the current investigation, which consists of measuring wall-pressure fluctuations through microphones embedded on the surface of a solid and a porous airfoil model. Furthermore, from the collected values, the dipole distribution predicted by Curle's analogy could be directly evaluated and the results compared between the two configurations.

From previous work, it is possible to find relevant contributions to the implementation of similar methodologies for unsteady pressure measurements. Paterson and Amiet [35] studied the wall-pressure fluctuations on a NACA-0012 wing profile placed downstream of a turbulence grid. This investigation showed the importance of a correct installation of the microphones, since the discontinuities between the surface of the body and the sensitive interface of the microphones were found to be responsible for the detachment of the boundary layer. For this reason, in the present work embedded microphones were preferred on the airfoil model, rather than flush-mounted ones. This is the same strategy adopted by Mish et al. [30], who performed wall-pressure fluctuations measurements on a NACA-0015 profile model equipped with microphones embedded on its surface and immersed in a turbulent flow, generated by the upstream grid. The main goal was to provide experimental data to validate Amiet's theory and a good agreement between the spectral results and the theoretical predictions was observed. The microphones were connected to the surface through a pressure tap and they were distributed along the chordwise and the spanwise direction. Their calibration was carried out using a special calibrator, consisting of a loudspeaker connected to a cavity necessary to propagate the acoustic signal.

Although wall-pressure fluctuations have already been measured as seen in the studies just described, the novelty introduced in this work is to apply this technique to a porous wing profile, in order to verify also experimentally the effect of porosity on the leading-edge noise reduction. As this is the continuation of the study discussed by Zamponi et al. [50], the solid and porous airfoil models chosen for the experimentation are again NACA-0024 profiles, which however in this case require an innovative design for the installation of the microphones. The porous solution, proposed and manufactured at VKI, is based on an external hard plastic exoskeleton to maintain the airfoil shape and a metallic wire mesh to limit the surface roughness; inside the structure, the volume is filled with melamine foam and a solid centerplane is installed along the chord to ensure the preservation of aerodynamic performance. The arrangement and type of microphones used will be described in detail in Chapter 4.

The most difficult challenge related to the experimental part is to design and implement a robust in-situ procedure for the microphones calibration, which are embedded on a curved surface and not on a flat plate. Encouraging results have been obtained by the work of de Santana et al. [11] in the analysis of wake-airfoil interaction noise. The authors tested low-cost electret microphones flush-mounted on a controlled-diffusion wing profile and they developed a portable, fast and repeatable calibration chain, made up of two different steps. The results of the calibration indicated potential issues that limited the operational frequency range of the microphones, both at low and high frequencies. It has been hypothesized that these problems are related to the geometry of the calibrator and to the way the microphones are installed. Nevertheless, good results in terms of stability and robustness were achieved and based on these the calibration procedure, used in the present work, is designed.

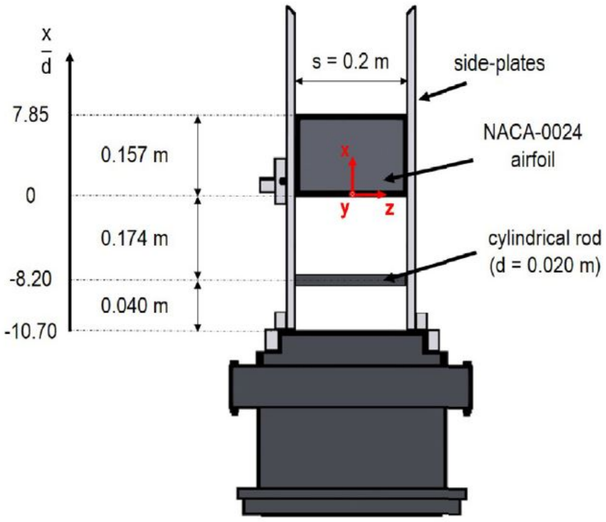

Figure 2.1: Sketch of the rod-airfoil configuration installed in the JAFAR facility of VKI. The red arrows denote the coordinate axes of the reference system. (Zamponi et al. [50])

The ultimate aim of the experimental investigation is to measure and compare the wall-pressure fluctuations between the solid and porous model, to evaluate the effective turbulence-interaction noise attenuation due to porosity. Figure 2.1 shows the rod-airfoil configuration adopted in the JAFAR facility of VKI for the tests carried out by Zamponi et al. [50]. The upstream circular rod, with a diameter of $d = 0.02$ m and immersed in a flow with a free-stream velocity of $U_\infty = 30$ m/s, is necessary for the generation of turbulent flow, because from its surface vortical structures separate alternately and continue downstream. When they get close to the leading-edge of the airfoil model, the eddies suffer the distortion responsible for the emitting sound. After mounting the model in the wind tunnel and calibrating the embedded microphones on the surface, the tests must be repeated in the same way for both the solid and porous airfoils. It is important to indicate the geometric measurements of the experimental setup, because they must be the same also in the numerical simulations so that the correct compatibility of the results is guaranteed.

Unfortunately, due to the European lock-down established to contain the global Covid-19 pandemic, there was a delay in the start of the laboratory activity. The time available was spent entirely in the calibration tests, trying to solve the problems encountered in the designed procedure. Given the unsatisfactory results obtained from the calibrations, it was not possible to proceed with the wind tunnel tests. Therefore, at the moment the post-processing analysis of the numerical data cannot be compared and confirmed experimentally.

2.4.2 Numerical simulations

The post-processing of the numerical data corresponds to the most important part of this investigation, because the results obtained from the various analysis expand the previous knowledge on the airfoil turbulence-interaction noise and for the first time provide the link between the attenuation of wall-pressure fluctuations and the distortion of turbulent structures.

The LES methodology was chosen to numerically study the leading-edge noise problem and the simulations were carried out by a group of researchers from the RWTH Aachen University, who subsequently provided the acquisition database. The computational setup is based on the experimental one, implemented in the VKI facility and already described in Section 2.4.1: it is the same rod-airfoil configuration applied for both solid and porous NACA-0024 profile models, also characterized by the same design parameters. Below is reported a brief explanation of the LES technique application and on how the melamine foam was numerically implemented, but for more details it is advisable to refer to the work of Satcunanathan et al. [42].

Within the LES, the homogeneous and isotropic porous medium is determined by the Darcy-Forchheimer model, which expresses the porous drag F to the incoming flow as follows:

$$F = \underbrace{\frac{1}{Re_k\sqrt{Da}}\varphi\mu\langle\mathbf{U}\rangle_F}_{Darcy} + \underbrace{\frac{1}{\sqrt{Da}}\varphi^2 c_F\langle\rho\rangle|\langle\mathbf{U}\rangle_F|\langle\mathbf{U}\rangle_F}_{Forchheimer} \tag{2.7}$$

Re_k indicates the permeability Reynolds number, defined as $Re_k = Re_d\sqrt{Da}$ and therefore dependent on the Reynolds number based on the rod diameter and the Darcy number, which is expressed as $Da = k/L^2$ where L is some reference length. The formulation also includes porosity φ, dynamic viscosity μ, density ρ and the Forchheimer coefficient c_F, as well as the flow velocity vector $\mathbf{U}$ on which the Favre average is applied, denoted with $\langle\rangle_F$.

In numerical simulations, the Darcy-Forchheimer model is a useful tool to characterize the porous materials through the porosity, the permeability and the Forchheimer coefficient. Moreover, it assumes that the structure of the pores remains rigid, avoiding the coupling effects due to elasticity and thermal issues. However, this model requires a preliminary calibration due to the pressure drop experienced by the equivalent flow setup when it passes through the porous material with a constant volume rate. It is necessary that the parameters, referring to the melamine foam used in the experimental tests, match this pressure drop in the best possible way: in particular, porosity and static air-flow resistivity were considered. From the calibration operations, the values of k and c_F are determined simultaneously and Table 2.1 summarizes all the parameters that characterize the computational porous material.

Table 2.1: Melamine foam parameter obtained from the Darcy-Forchheimer model, setting $L = d$. The permeability is given in terms of Darcy number.

$\boldsymbol{Da}$ [−]	$\boldsymbol{c_F}$ [−]	$\boldsymbol{\varphi}$ [−]	$\boldsymbol{Re_k}$ [−]
5.3×10^{-6}	0	0.986	92

If the characterization of the melamine foam is solved through the Darcy-Forchheimer model, the numerical implementation of the external exoskeleton with the wire mesh as a homogeneous porous material represents a difficult point of the discussion. Since a dominant contribution is expected from the melamine foam placed inside the airfoil, it is assumed that in the porous case the entire structure is made exclusively with the porous medium, which is also able to maintain the shape of the NACA-0024 profile. Consequently, the surface roughness effects are not captured by the simulations.

The LES are based on the resolution of the compressible Volume Averaged Navier-Stokes (VANS) equations using a finite-volume method. These equations are discretized in time through an explicit Runge-Kutta scheme, while in space it is necessary to divide the discretization between inviscid fluxes and viscous fluxes: on the former an Advected Upstream Splitting Method (AUSM) is applied, whilst on the latter a centered discretization is performed. Concerning the treatment of the wall boundaries and the fluid-porous interface, detailed explanations can be found in the study of Satcunanathan et al. [42].

The computational domain extends $90d \times 64d \times \pi d$ along the x, y and z axis respectively, for a total of 186 million mesh points in the solid configuration and 206 million mesh points for the porous one. For the post-processing activity, different data are available depending on the surface considered:

- On the plane at the midspan of both airfoils with the extension shown in Figure 2.2, the values of the three instantaneous velocity components are provided for 1270 successive time instants in the solid case and 1280 in the porous one. These data will be mainly used for the analysis of velocity fluctuations in the stagnation region and for the evaluation of the vorticity field.

- The values of the same instantaneous velocity components are also calculated on three different streamwise-spanwise planes that extend from the surface of the airfoil, as reported in Figure 2.3. The distances between these planes are not random, but correspond to significant points for the following analysis: the first is located exactly at the leading-edge, the second is arranged in the position where the wall-pressure fluctuations are maximum and the third is even more downstream. Also in this case there are 1270 time instants available for the simulation with the solid wing profile and 1280 with the porous one. As will be seen later, the turbulent-velocity power spectra are plotted using these data.

- Compared to the work of Zamponi et al. [50], in the present investigation the LES also provide the instantaneous velocity components, pressure and density data over the entire surface of both airfoils configuration, for 1276 time instants. Moreover, for the porous model, the simulation also includes the values of these quantities on the internal solid centerplane, to analyze its contribution. From the post-processing, it is possible to calculate the unsteady wall-pressure fluctuations and, therefore, the acoustic spectrum in the frequency domain. The results, which will be discussed in Chapter 3, overcome the limitations encountered so far and show the possible link between the attenuation of the leading-edge noise and of the turbulence distortion due to porosity.

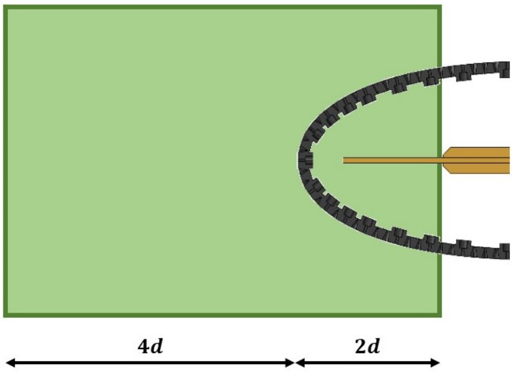

Figure 2.2: Sketch of the plane at the midspan of the NACA-0024 wing profile. Its extension is indicated as a function of the rod diameter, *d*.

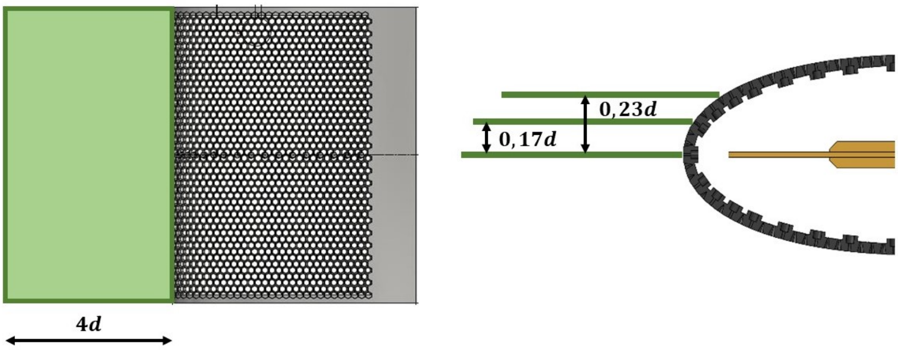

Figure 2.3: Sketch of the three streamwise-spanwise planes extended upstream from the surface of the NACA-0024 wing profile. Their position is defined as a function of the rod diameter, *d*.

Chapter 3

Results of LES data post-processing

As previously mentioned, this chapter includes the main results obtained from the post-processing of the numerical data, generated at the RWTH Aachen University using the large-eddy simulations. To enrich what has already been obtained by Zamponi et al. [50], the new simulation provides additional information regarding the instantaneous velocity and pressure fields along the surface of the NACA-0024 airfoil.

3.1 Analysis of wall-pressure data

The main focus of this work is to demonstrate how the use of porous material in the airfoil structure determines a reduction in the aeroacoustic noise generated by the impact of the turbulent flow on the surface. As explained in Chapter 2, since the sound is produced by small perturbations of the flow field, it is important to investigate the pressure fluctuations which are linked to the production of noise. Indeed, according to Curle's analogy [10], the dipolar term that appears in Equation 2.6 is the main sound source and is due to unsteady wall-pressure fluctuations. Since the instantaneous pressure values are available at each point of the airfoil surface for several instants of time, the corresponding mean value is subtracted from these to derive the fluctuations data.

3.1.1 Pressure fluctuations along the surface

To have a first qualitative comparison between the solid and the porous case, the root mean square of the pressure fluctuations has been calculated and the results for the leading-edge region are shown in Figure 3.1.

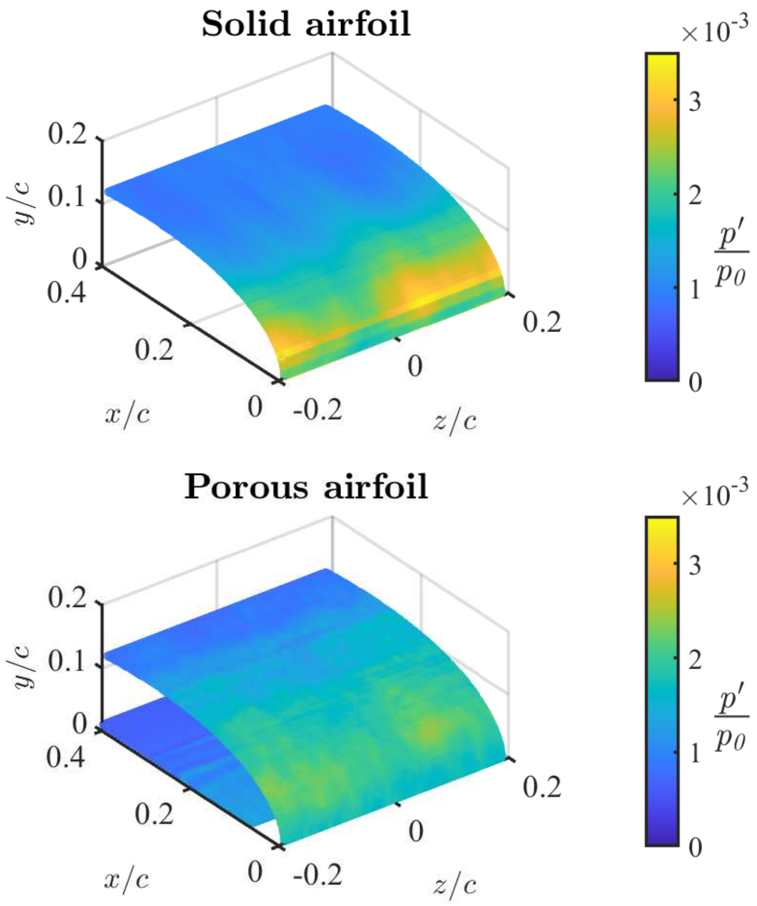

Figure 3.1: Root mean square of pressure fluctuations on the surface of the solid and porous airfoil in the leading-edge region. The p'_{rms} is made dimensionless by the theoretical stagnation value, p_0.

The p'_{rms} values are made dimensionless by the reference value p_0, which is defined as:

$$p_0 = \rho_0 \cdot a_0^2 \tag{3.1}$$

where ρ_0 and a_0 are respectively the density and the speed of sound at the stagnation point, in the theoretical case of inviscid flow. Knowing the free-stream quantities, it is immediate to evaluate these two parameters using the isentropic relations:

$$\rho_0 = \rho_\infty \left(1 + \frac{\gamma - 1}{2} M_\infty^2\right)^{\frac{1}{\gamma-1}} \tag{3.2}$$

$$a_0 = \sqrt{a_\infty^2 + \frac{\gamma - 1}{2} U_\infty^2} \tag{3.3}$$

The plot for the solid airfoil model reveals a maximum of p'_{rms} around $y = 0.17d$ and this differs from what is hypothesized in Curle's analogy, according to which the main acoustic sources are located exactly at the leading-edge. On the other hand, from the map of the porous airfoil, a lack of a peak in the pressure fluctuations can be clearly seen, even if the higher values are recorded around the same coordinate: this denotes an important reduction in terms of aeroacoustic noise that, at this early stage, confirms the beneficial effect of the introduction of porosity.

3.1.2 Spatial coherence in the spanwise direction

To deepen the analysis of pressure data and to better understand the energy content of coherent flow structures as the frequency varies, the coherence between pressure fluctuations values in the spanwise direction has been studied. The spatial coherence function is evaluated between two points with the same x and y coordinates, but different z, and is defined as follows:

$$\gamma^2_{p_i p_j}(f) = \frac{|\Phi_{p_i p_j}(f)|^2}{\Phi_{p_i p_i}(f)\Phi_{p_j p_j}(f)} \tag{3.4}$$

where p_i is the value at $z/r_{LE} = 0$ considered as reference and p_j is the other point at a different spanwise location. $\Phi_{p_i p_j}(f)$ represents the Cross Power Spectral Density (CPSD) between the wall-pressure fluctuations of the two examined points, while $\Phi_{p_i p_i}(f)$ corresponds to the PSD of each one.

Since in Figure 3.1 it is observed that the greatest reduction of the p' fluctuations occurs at $y = 0.17d$, the first evaluation of the spanwise coherence contour was done at this coordinate. Therefore, Equation 3.4 is applied keeping the reference value at $z/r_{LE} = 0$ fixed and varying the other point along the direction with $z/r_{LE} > 0$: the choice to take only the positive part is linked to the two-dimensionality of the field, which would result in analogously also for negative z. Figure 3.2 shows the trend of the spatial coherence not only as a function of the spanwise direction but also of the frequency, expressed through the Strouhal number. This dimensionless parameter is based on the cylindrical rod diameter d and the free-stream velocity U_∞. The St estimated for the vortex-shedding frequency is 0.2 and is indicated on the maps by the dashed line.

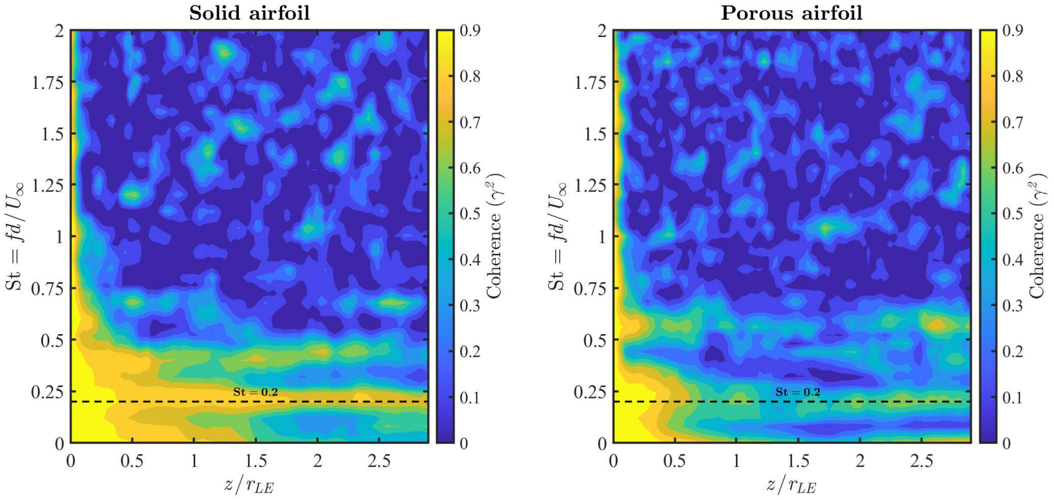

Figure 3.2: Spanwise coherence contour along $y = 0.17d$ of the solid and porous airfoil, using as reference the value at $z/r_{LE} = 0$.

From the maps, it is immediately observed that the greater coherence of the flow structures occurs around the vortex-shedding frequency both in the solid and in the porous case, as already demonstrated by Tong et al. [46]. However, this is the only similarity found between the two models under consideration. Indeed, for the porous airfoil there is a sudden decrease in spatial coherence proceeding along with the spanwise direction: at $z/r_{LE} > 0.5$ the γ^2 value tends to be already around 0.5-0.6, in contrast with what is obtained for the solid case where the coherence is maintained on the values of 0.8 for the entire positive z axis. The significant reduction due to porosity indicates that the turbulent flow structures remain less coherent in the spanwise direction than the solid model and this may have a link with the attenuation of turbulence-interaction noise.

Generally, this type of spatial coherence analysis is also associated with the calculation of the spanwise coherence length, defined as the spanwise distance over which the coherence drops to 0.5 [29]. The Figure 3.3 shows the comparison between the γ^2 trends for the solid and porous models along with the spanwise direction at $y = 0.17d$, extracted at the vortex-shedding frequency: as deduced from the analysis of the maps in Figure 3.2, the values for the solid case remains for the entire range of z at higher values than the porous case, demonstrating the greater coherence of the flow structures. However, while for the former γ^2 gradually decreases along with the spanwise direction, for the latter it starts increasing for $z/r_{LE} > 1.5$.

In this study, following the definition above, the spanwise coherence length could only be calculated for the porous airfoil and if the increase that occurs immediately after is neglected. Nevertheless, the result could not be compared with the solid one given that the value of the spatial coherence never drops below 0.7. This problem could be linked to an insufficient extension of the airfoil in the spanwise direction, which therefore does not allow for the achievement of the value necessary to compute the spanwise coherence length.

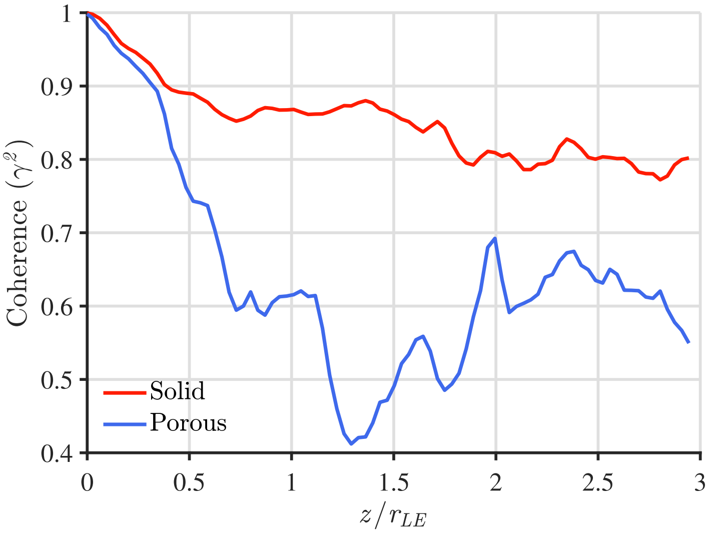

Figure 3.3: Trends of the spanwise coherence for the solid (red line) and porous (blue line) airfoil along $y = 0.17d$ and at $St = 0.2$. The value at $z/r_{LE} = 0$ is used as reference.

In order to draw further conclusions from the spatial coherence analysis, the γ^2 trends are shown in Figure 3.4 as a function of the Strouhal number for four specific locations along the airfoil, identifying four different spanwise distances for each of them. The different positions along the surface are represented in the four columns and the respective coordinates are shown in Table 3.1. On the other hand, each row of Figure 3.4 corresponds to a different spanwise distance which gradually increases with respect to the reference point placed exactly at $z/r_{LE} = 0$; the coordinates of each point along with the z axis are specified in Table 3.2. In each graph both the solid and the porous trend are plotted, so that the comparison between the two configurations is immediate.

As expected from the information obtained above, for all positions along the surface both solid and porous configurations show a reduction in the spatial coherence as the spanwise distance from the reference point increases. Nevertheless, for larger z/r_{LE} a slight increase in the porous curve can be seen, which is a trend already exhibited by the extraction in Figure 3.3. From the results, it is clear that in almost all locations the highest level of spatial coherence occurs at the vortex-shedding frequency and it is precisely there that attention must be focused.

Table 3.1: Positions along the suction side of the airfoil taken into consideration for spatial coherence analysis.

	Column 1	**Column 2**	**Column 3**	**Column 4**
x/r_{LE}	-0.026	0.044	0.34	1.03
y/r_{LE}	0.0088	0.34	0.79	1.26

Table 3.2: Spanwise coordinates of the points used, together with the reference one, to compute the spatial coherence γ^2.

	z/r_{LE}
Row 1	0.31
Row 2	0.80
Row 3	1.50
Row 4	2.49

In the case of the smallest spanwise distance, it is observed that the broadband component of the coherence is so high that the peak that characterizes all the other trends at $St = 0.2$ does not significantly emerge. If for the solid case the curve remains almost unaltered in the four positions, for the porous one it is instead noted that the tonal component relating to the vortex shedding phenomenon appears moving along the surface. This difference highlighted between the two configurations becomes more significant for larger spanwise separations. Increasing the considered z/r_{LE} distance, the γ^2 reduction is evident with respect to the previous trends in particular on the broadband component: the spatial coherence becomes predominantly tonal and decreases at other frequencies, indicating that the 2D flow structures are able to maintain their coherence over a larger spanwise distance than the 3D ones [29].

Besides the fact that the peak at $St = 0.2$ becomes more visible as the spanwise coordinate increases, for $z/r_{LE} = 0.8$ and 1.5 the difference between the solid and the porous trend reaches the maximum value especially in the two locations downstream of the stagnation point. As seen in Figure 3.1 and as will be discussed in Section 3.2 through the PSDs analysis, these two positions along the surface are those where the wall-pressure fluctuations in the porous airfoil decrease more than in the solid one. With the results in Figure 3.4, it is also verified that the turbulent structures lose their coherence on a porous surface and this aspect could be because the flow can partially penetrate inside the body. This leads to the hypothesis that the turbulence distortion also affects the pressure field and may constitute one of the fundamental physical mechanisms for the reduction of leading-edge noise.

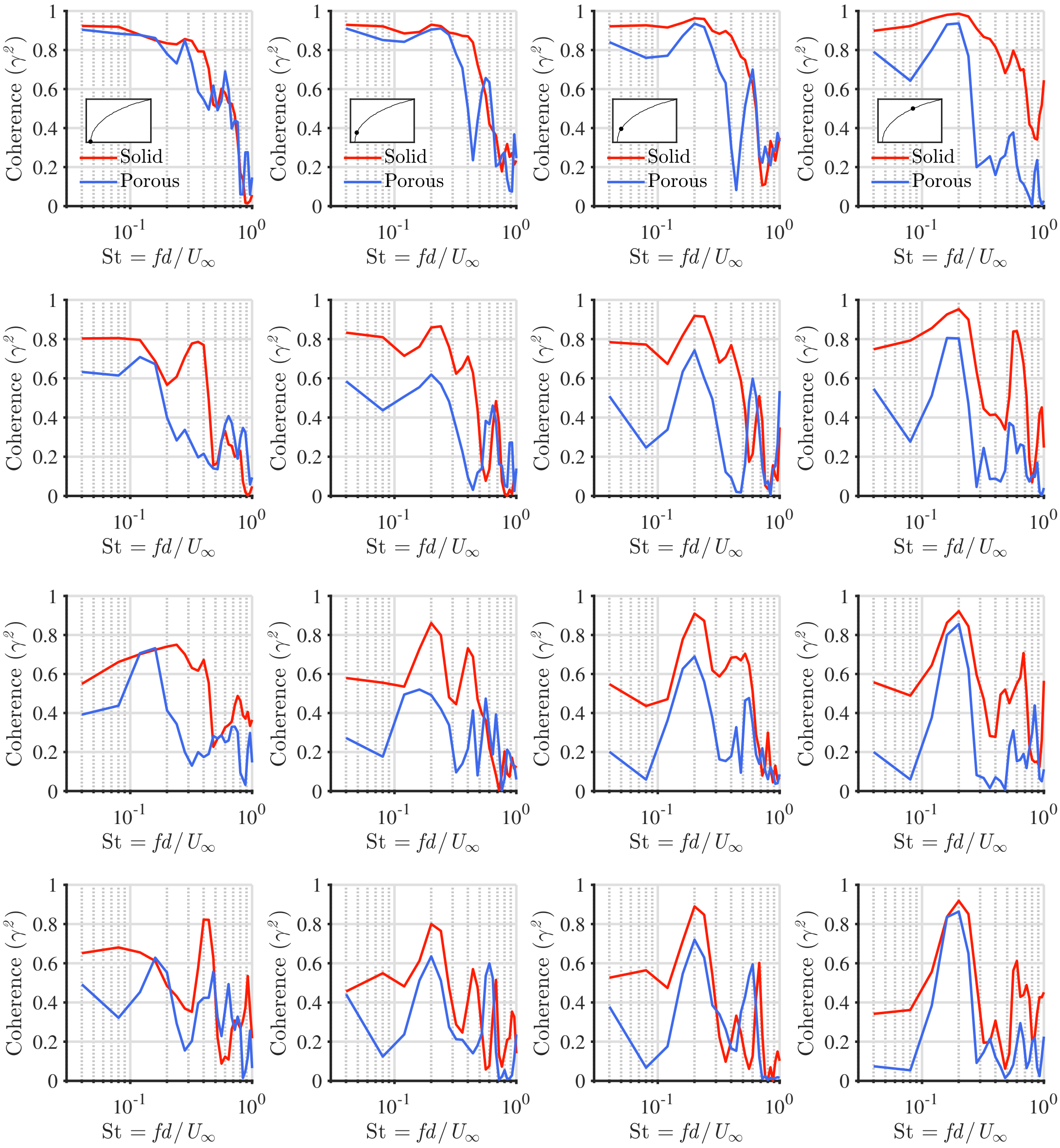

Figure 3.4: Spanwise coherence of the solid (red line) and porous (blue line) airfoil, measured between four spanwise locations (rows) at different positions along the surface (columns). The value at $z/r_{LE} = 0$ is used as reference.

Finally, it is noted that for any z/r_{LE} at the stagnation point there is no peak at the vortex-shedding frequency, which instead appears proceeding along the suction side of the airfoil. Actually, the maximum value of the spatial coherence increases more and more, which is believed to be due to the development of larger turbulent flow structures [29].

The last analysis concerning the spatial coherence that provides useful information is the γ^2 trends extracted for $St = 0.2$ as a function of the spanwise distance, in the same positions along the airfoil indicated in Table 3.1. The results, together with the interpolations using a Gaussian function, are shown in Figure 3.5: only the $0 < z/r_{LE} < 1$ range is considered, because it is the one where the coherence for both configurations decreases continuously without any rises. It is observed in all cases that γ^2 is nearly 1 for small distances along the z axis, indicating that the two signals are perfectly correlated. On the other hand, as expected, the spatial coherence of the pressure fluctuations decreases for larger spanwise distances and this reduction is greater for the porous airfoil, especially at $z/r_{LE} = 0.8$ and 1.5 in agreement with what has already been discussed above. Moreover, it is evident that this parameter decays much more rapidly at the stagnation point, also reaching lower values compared to the further downstream locations: being evaluated at the vortex-shedding frequency, this confirms again that the peak is higher proceeding along the airfoil.

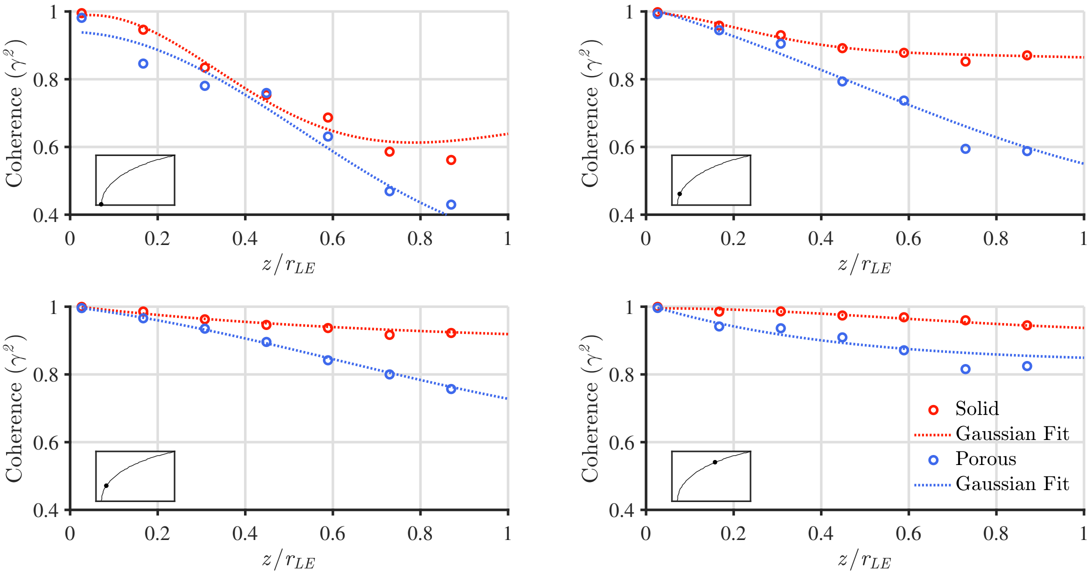

Figure 3.5: Spatial coherence results in terms of the spanwise distance z/r_{LE} at the vortex-shedding frequency at different locations along the surface for the solid (red spots) and porous (blue spots) airfoils. The dotted lines represent the Gaussian fits of the data shown in the graphs.

3.1.3 Pressure fluctuations phase

The distribution of the wall-pressure fluctuations phase is one of the most important analysis that are carried out in every study concerning the serrations, which are structural changes brought on the leading or trailing-edge always to reduce the aeroacoustic noise generated by the impact of turbulence on the airfoil. From the results obtained with this alternative solution [1, 24, 46], it was deduced that the phase variation constitutes one of the noise reduction mechanisms and it has also already been demonstrated experimentally. Therefore, the same analysis was applied to the present case in order to assess whether the porosity significantly affected this quantity.

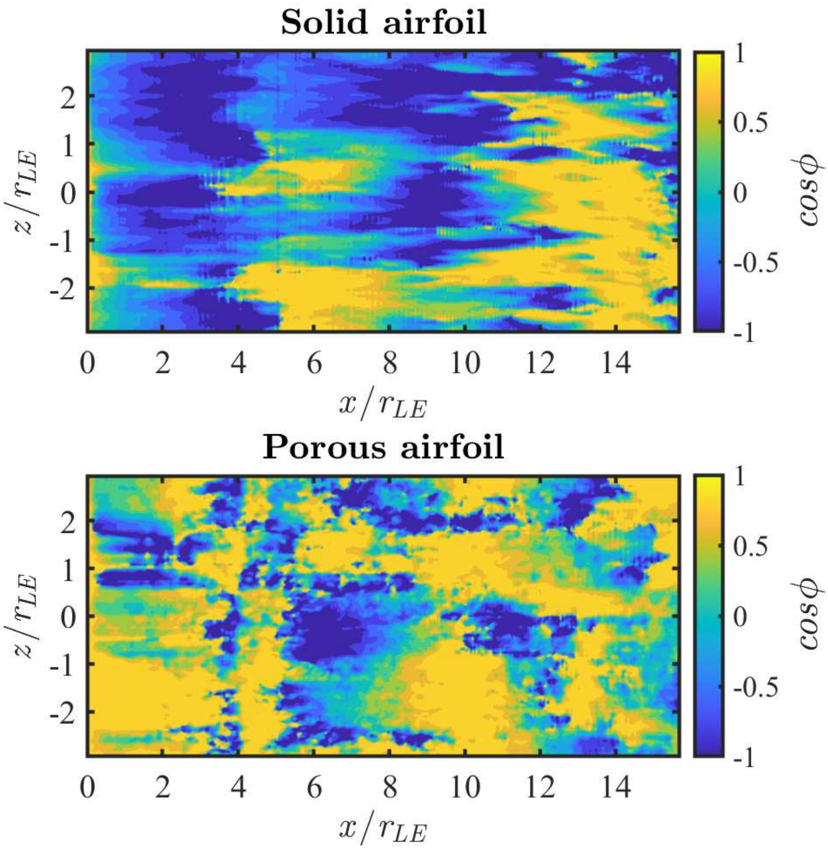

Figure 3.6: Wall-pressure fluctuations phase (expressed using $\cos\phi$) distribution on the airfoil surface at $St = 0.2$ for the solid and the porous configuration. The p' values at $x/r_{LE} = 0$ are used as reference for the calculation of this quantity.

The wall-pressure fluctuations phase is defined as:

$$\cos\phi(f) = \cos\Big(\mathrm{Im}\Big(\Phi_{p_i p_j}(f)\Big)\Big) \tag{3.5}$$

where $\Phi_{p_i p_j}(f)$ is again the CPSD of pressure fluctuations computed between two different positions, one of which is always fixed and located at the stagnation point; indeed, each point on the surface is compared with the corresponding one positioned at $x/r_{LE} = 0$ and at the same z/r_{LE} coordinate. The CPSD returns a complex number, whose imaginary part corresponds to the phase angle ϕ.

Figure 3.6 shows the phase distribution on the suction side of both solid and porous airfoils at the vortex-shedding frequency: more precisely, the $\cos\phi$ value is plotted because it is the most convenient way to comment on the results, varying between 1 and -1. For the solid case, the phase distribution is more uniform along with both streamwise and spanwise directions, whereas it tends to be more complex for the porous one. The alteration between positive and negative regions is more prominent and it is beneficial to reduce the correlation of the sound sources, leading to a destructive interference. Therefore, it seems that the phase variation on the porous surface is greater than that on the solid one, which could indicate a more pronounced destructive phase interference as occurs for the serrations [46].

This aspect could have a significant impact on reducing the noise level in the acoustic far-field and it could be important to conduct similar analysis in future studies, to understand if porosity really generates a destructive phase interference and if this phenomenon represents a mechanism linked to the abatement of leading-edge noise.

3.2 Analysis of velocity data

In addition to the pressure data along the surface of the airfoil, the numerical simulations also provide information on the instantaneous velocity that is considered to evaluate how the flow field is affected by introducing porous materials. With the analysis that will be presented below, the goal is to study the trend of the velocity components and highlight the differences that appear between the two different configurations.

3.2.1 Mean and fluctuating velocity components in the stagnation region

The velocity maps reported in this paragraph have already been presented by Zamponi et al. [50], using a previous numerical data-set based on the same LES simulation. Therefore, this first part of the present section has the purpose of replicating the same type of study to confirm the results already obtained.

Since the simulations include instantaneous velocity data in the vertical plane at the midspan of the airfoil (i.e. passing through $z/r_{LE} = 0$), the maps are based on these values and the stagnation region represented extends between $-8 < x/r_{LE} < 2$ and $-4 < y/r_{LE} < 4$. As can be seen from the coordinates, the plotted area also includes part of the airfoil to investigate the evolution of the different quantities both along the external surface and inside the structure. The latter aspect is especially useful for the porous model, in order to evaluate the flow penetration within the inner volume of the airfoil. For a complete analysis, it is necessary to separate the average component from the fluctuating one according to the Reynolds decomposition: for the former, it is sufficient to calculate the average with all the instants of time available, while to obtain the fluctuations the mean value is subtracted from the instantaneous data. Once the velocity fluctuations at each time instant have been obtained, their root mean square is calculated according to the definition:

$$x_{rms} = \sqrt{\frac{1}{N}\sum_{n=1}^{N} |x_n|^2} \tag{3.6}$$

where N is the total number of time instants and x_n indicates the fluctuating component of the generic parameter under examination. In this case, the equation is applied to the quantities u, v and w that correspond respectively to the velocity components in the x, y and z direction. For simplicity, the symbols $-$ and $'$ are used in the maps to differentiate the mean values from the corresponding r.m.s. Lastly, both terms are divided by the free-stream velocity, obtaining for the fluctuating part the dimensionless parameter known as Turbulence Intensity (TI).

Figure 3.7 shows the results of the mean streamwise and upwash velocity components by comparing the trend of the solid model, on the left, with that of the porous model, on the right. Figure 3.7(a) shows that $\bar{u}$ for the solid airfoil is approximately equal to U_∞ far upstream of the airfoil and rapidly decreases near the leading edge. For the porous configuration, the velocity gradient is found to be reduced, resulting in lower $\bar{u}$ for $x/r_{LE} < 4$. Moreover, the streamwise velocity does not vanish at the wall in this case due to the possibility for the flow to penetrate the airfoil. Also, the streamwise velocity profiles in the boundary layer around the airfoil are affected by porosity, which seems to induce an increase in the boundary layer thickness. With regards to the mean upwash velocity component in Figure 3.7(b), the $\bar{v}$ field that is defined in the stagnation region is characterized by a perfect symmetry between the suction and the pressure side, maintained in both configurations. The difference between the two cases concerns the greater extension of the regions where the maximum and minimum values are reached around the surface in the porous airfoil. In reality, an attenuation of the mean upwash velocity component would have been expected similarly to what occurs for $\bar{u}$.

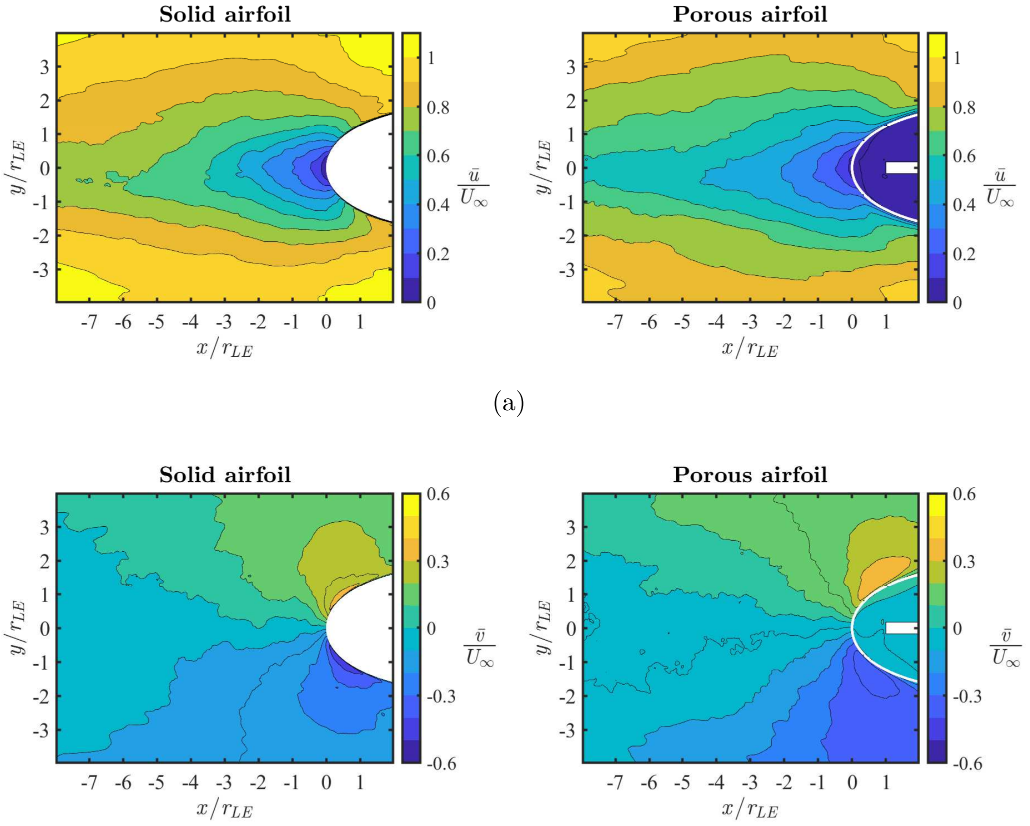

(a)

(b)

Figure 3.7: Mean velocity for the solid and the porous airfoil in the stagnation region, extracted at the midspan. The streamwise $\bar{u}$ (a) and the upwash $\bar{v}$ (b) component are made dimensionless by the free-stream velocity, U_∞.

Once the main differences concerning the mean values have been underlined, it is important to examine the trend of velocity fluctuations that are related to the pressure fluctuations and, therefore, to the generation of aeroacoustic noise. Figure 3.8 shows the maps of the fluctuating streamwise and upwash velocity components, always compared between the two configurations. First, it is observed that the quantity v' takes on higher values than u' and this is due to the shed vortices, which characterize the wake of the rod and determine the velocity fluctuations that interact with the airfoil.

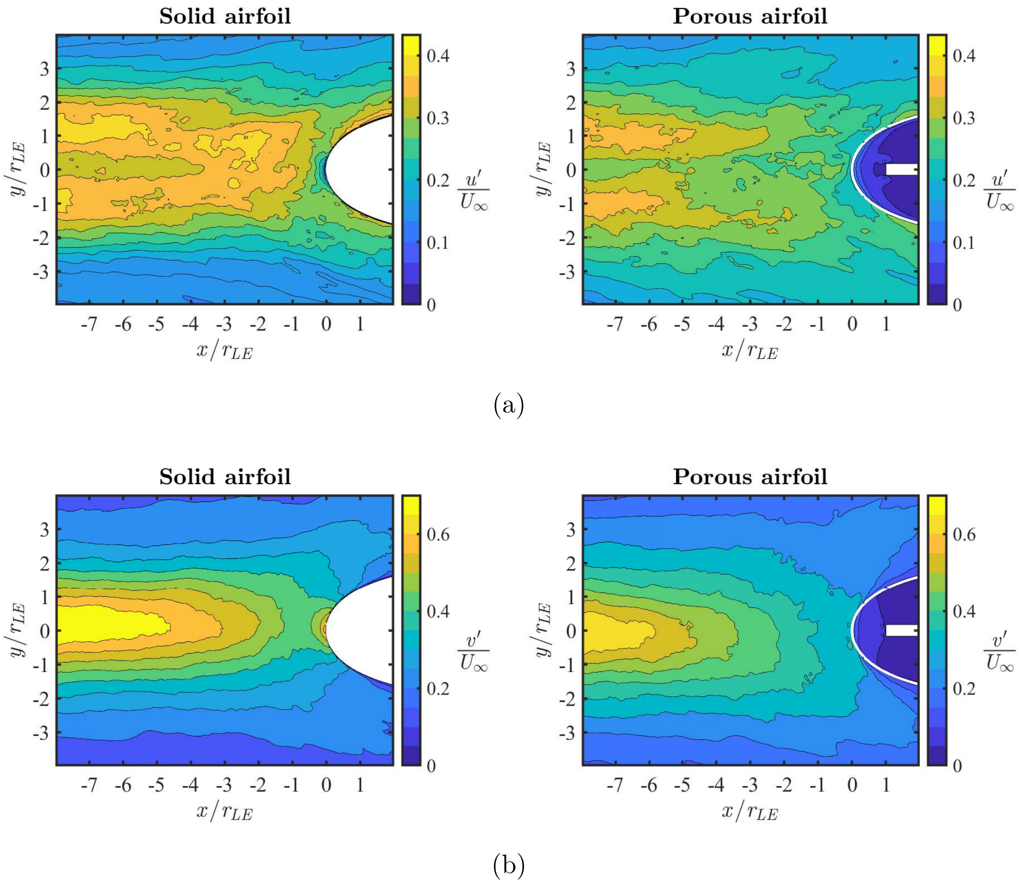

Figure 3.8: Turbulence intensity for the solid and the porous airfoil in the stagnation region, extracted at the midspan. The streamwise u' (a) and the upwash v' (b) component are made dimensionless by the free-stream velocity, U_∞.

Both for the streamwise and the upwash component, porosity induces an evident decrease in the stagnation region which involves lower values already at $x/r_{LE} = -6$. In the solid model, u' reaches zero exactly at the stagnation point, creating a region around it where the slowdown is sudden. In contrast in the porous case, as already said, the streamwise fluctuations have a lower intensity but do not completely cancel out at $x/r_{LE} = 0$, given the possibility for the flow to partially penetrate inside the airfoil: indeed, it is observed that zero is reached only by the impact with the internal centerplane. Along the surface of the porous airfoil, in Figure 3.8(a) it is also noted that the value of u' grows more slowly than in the solid case, an aspect attributable to the same explanation. For the upwash velocity fluctuations in Figure 3.8(b), there is a similar argument:

around the stagnation point, in the solid configuration v' rises until it assumes very high values, while in the porous one there is no increase in that small area and again it is completely canceled out near the centerplane. The analysis of the velocity fluctuations maps provides qualitative information on the behavior of the flow for the two configurations in the stagnation region, which will be further investigated by extracting the values of u' and v' along the stagnation streamline.

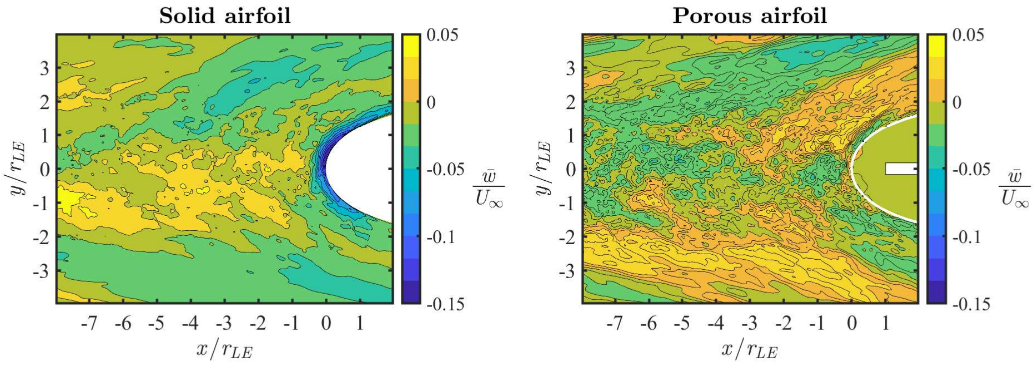

(a)

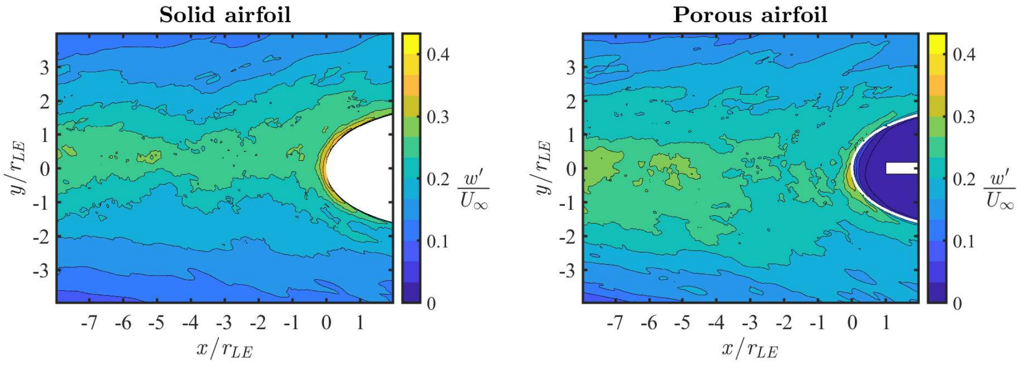

(b)

Figure 3.9: Spanwise component of mean velocity (a) and turbulence intensity (b) for the solid and porous airfoil in the stagnation region, extracted at the midspan. The $\bar{w}$ and the w' are made dimensionless by the free-stream velocity, U_∞.

Lastly, the spanwise velocity component is analyzed, always splitting the mean part from the fluctuating one: in this case, the goal is to verify that the contribution of w is negligible with respect to the other two components since the flow is two-dimensional. From the results shown in Figure 3.9, it can be seen that in both configurations the stagnation region is characterized by values of $\bar{w}$ very close to zero. The only difference is found around the stagnation point where the mean component assumes negative values in the solid case, while in the porous one it remains zero; the range of variation is however minimal, therefore it can be assumed negligible. Concerning the fluctuating component, it is observed that the w' field remains almost the same between the solid and the porous airfoil, consequently it can be safely ignored for the following analysis. Moreover, the contours of the lines are not well defined in all the maps presented, because it would be necessary a greater number of time instants to obtain smoother curves.

As mentioned above, to obtain a quantitative evaluation of the variations encountered by u' and v', it was decided to plot the corresponding values for both configurations along the stagnation streamline, as shown in Figure 3.10. Both porous trends were normalized using the ratio between the respective values of the solid and porous cases, extracted at $x/r_{LE} = -4$.

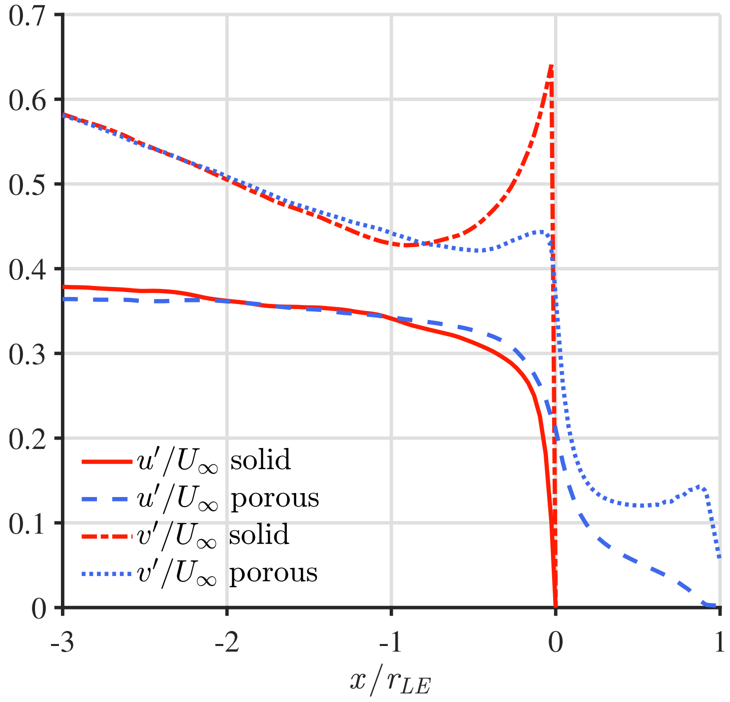

Figure 3.10: Turbulence intensity for the solid (red lines) and the porous airfoil (blue lines) extracted along the stagnation streamline. The streamwise u' and the upwash v' component are made dimensionless by the free-stream velocity, U_∞.

In confirmation of what is observed in Figure 3.8(a), the streamwise velocity fluctuations decrease drastically as they approach the leading-edge, due to the presence of the airfoil. If for $x/r_{LE} < -1$ the trend of the solid model is slightly higher, the situation is reversed near the surface and there is a less slowdown in the porous case: indeed, u' does not cancel out at the stagnation point but, being able to penetrate within the airfoil, continues to decrease until it reaches the centerplane.

On the other hand, from the trends, it is immediate to notice how the upwash velocity fluctuations are considerably dampened by the porosity when approaching the leading-edge, again following what is commented in Figure 3.8(b). The significant amplification experienced around the stagnation point is mitigated by the porosity and this reduction is similarly observed in the Turbulent Kinetic Energy (TKE), reported in Figure 3.11 and defined as:

$$TKE = \frac{u' + v' + w'}{3} \tag{3.7}$$

The attenuation experienced by v' represents the central point to explain how the porous treatment affects the turbulence distortion, since according to Amiet's theory [2] the generation of aeroacoustic noise is linked to this fluctuating velocity component. As for the streamwise fluctuations, also the upwash ones cancel out at $x/r_{LE} = 0$ in the solid case due to the non-penetration condition, while it is observed that inside the porous airfoil they continue to decrease until they reach the centerplane, where there is a slight increase given by the impact with it.

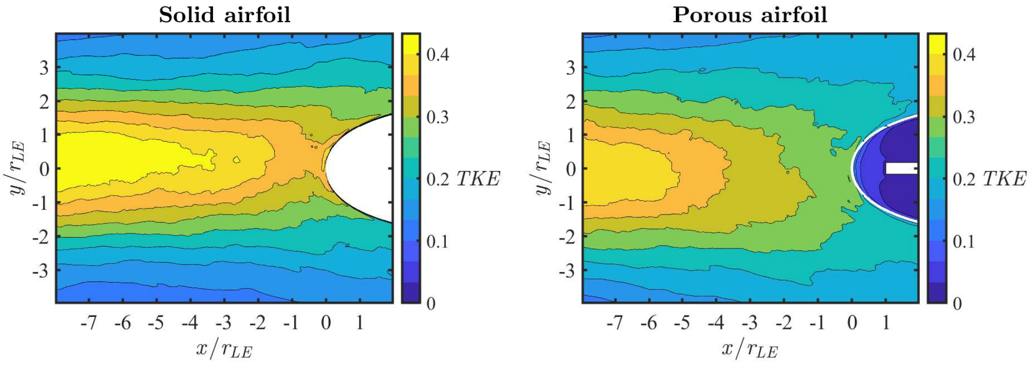

Figure 3.11: Turbulent kinetic energy for the solid and the porous airfoil in the stagnation region, extracted at the midspan and made dimensionless by the free-stream velocity, U_∞.

The trends of u' and v' shown in Figure 3.10 appear smoother than the velocity maps, because for this graph the numerical data obtained from the simulation on the horizontal plane at $y = 0$ have been used: since the flow field has proved to be two-dimensional, all the spanwise values have been averaged over the quantities at the same x/r_{LE} coordinate in order to increase the number of samples with which to compute and plot the results.

3.2.2 Comparison between the power spectral densities of velocity and pressure fluctuations

After studying in the stagnation region the trend of the three different velocity components both in their mean and fluctuating contribution, the most important analysis is represented by the evaluation of the Power Spectral Density (PSD) that is the signal power distribution as a function of frequency. Each word expresses a fundamental property of this function: *power* indicates that the PSD amplitude corresponds to the root mean square value of the analyzed signal, *spectral* specifies that it is a function of frequency according to Fourier's analysis and *density* refers to the fact that the amplitude is normalized to a single Hz band. Therefore, this tool is useful for understanding at which frequency range the signal variations are stronger and where they are weaker. In this case, the PSD function is applied to the turbulent velocity components u' and v' and to the wall-pressure fluctuations, in order to compare these quantities and find analogies between them. The Welch method has been employed to process the values, with blocks of 512 samples windowed using the Hamming function that is characterized by a 50% data overlap.

The PSDs of the instantaneous velocity fluctuations have been computed extracting the data from the three horizontal planes located at $y = 0$ in Figure 3.13(a), at $y = 0.17d$ in Figure 3.13(b) and at $y = 0.23d$ in Figure 3.13(c). As explained in Section 2.4.2 about the numerical methodology, these planes extend up to the surface of the airfoil and the points closest to it have been used to evaluate the PSD. Their specific locations are determined by the coordinates listed in Table 3.3. On the other hand, in order to correctly compare the graphs, the wall-pressure fluctuations were taken in the three points closest to those indicated above and their positions are reported in Table 3.4.

Table 3.3: Points closest to the surface of the airfoil, extracted from the three horizontal planes to compute the PSDs of turbulent velocity components.

	y=0	**y=0.17d**	**y=0.23d**
x/r_{LE}	-0.026	0.044	0.34
y/r_{LE}	0.0088	0.34	0.79

Table 3.4: Positions along the suction side of the airfoil considered to compute the PSDs of wall-pressure fluctuations.

	y=0	**y=0.17d**	**y=0.23d**
x/r_{LE}	-0.0084	0.062	0.13
y/r_{LE}	0.026	0.36	0.50

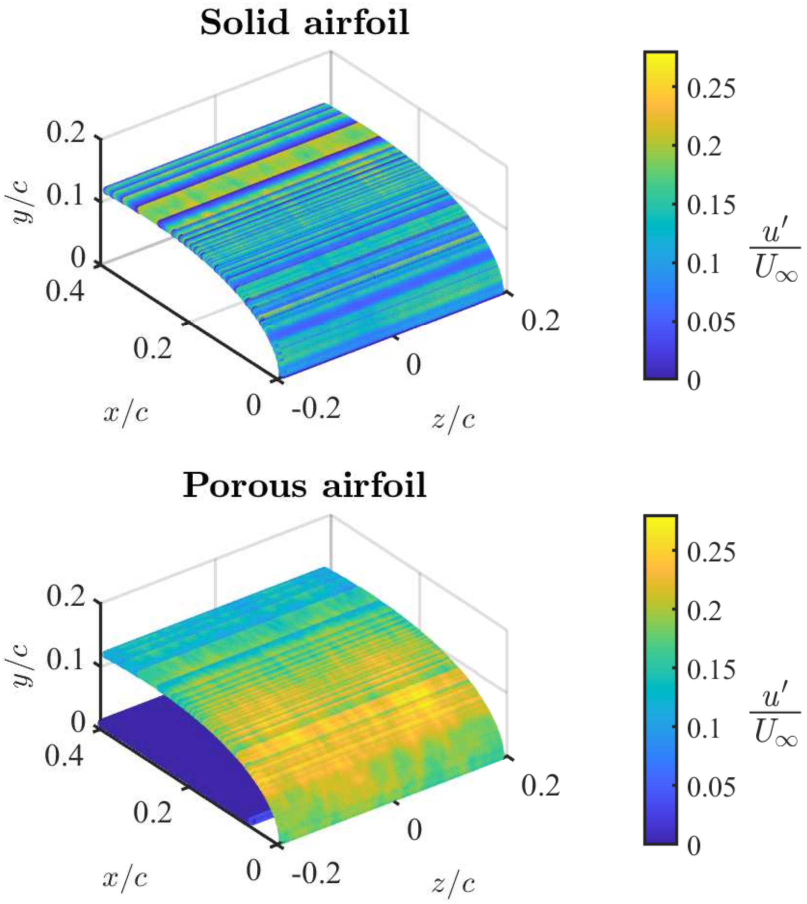

Figure 3.12: Streamwise component of velocity fluctuations on the surface of the solid and porous airfoil in the leading-edge region. The u' is made dimensionless by the free-stream velocity, U_∞.

The u' e v' values directly obtained on the surface of the airfoils were not used, because from Figure 3.12 it was noted that the streamwise fluctuations do not cancel out on the wall. If it does not raise any doubts in the porous case where the flow can penetrate inside the structure, for the solid one this behavior disagrees with the no-slip condition, which states that the velocity must be zero at the wall. It was not possible to give a reliable explanation for this inconsistency, which therefore remains unclear and which was bypassed for the calculation of the PSDs, where the values belonging to the three horizontal planes were used.

The power spectra are presented in dB/St and the frequency is expressed by the Strouhal number, based on the cylindrical rod diameter d and the free-stream velocity U_∞. Again the St estimated for the vortex-shedding frequency is 0.2, as can be seen from the peaks present in the trends of all three analyzed quantities. In order to compare correctly the trends, it is necessary to normalize the velocity fluctuations: u' and v' values used for the calculation of the PSD of the porous airfoil have been multiplied by the same correction factor already introduced for the evolution of turbulence intensity along the stagnation streamline, which is based on the quantities extracted at $x/r_{LE} = -4$. The result of this normalization is reported in Figure 3.13, where (a) represents the trends for $y = 0$, (b) for $y = 0.17d$ and (c) for $y = 0.23d$.

As previously analyzed, at the stagnation point the $\text{PSD}_{u'u'}$ is higher for the porous case in accordance with the trend shown in Figure 3.10 along the stagnation streamline, where the reduction of u' is more significant for the solid airfoil; furthermore, in neither configuration, the flow is characterized by the peak relative to the vortex-shedding frequency. Moving further downstream of the leading-edge, the power spectrum of the streamwise component of the velocity fluctuations in the porous airfoil remains higher, without exhibiting the vortex-shedding peak that instead appears in the trend of the solid one. This can suggest a better damping of the vortical structures once they impact a porous surface, also explaining the important noise reduction that occurs in the low-frequency range. Finally, in Figure 3.13(c), the deviation between the curves is reduced and at $St = 0.2$ also the porous configuration shows a peak that is anyway smaller than the solid one, demonstrating that the benefit of porosity is still present. On the other hand, starting from the stagnation point, the $\text{PSD}_{v'v'}$ for the two models converge to the same trend and show an appreciable alteration of the vortex-shedding peak for the porous case in all three analyzed positions. From the comparison of the graphs in Figure 3.13(b), it seems that the greatest reduction due to porosity occurs at $y = 0.17d$, i.e. at the location where the wall-pressure fluctuations are maximum.

To confirm what has just been described, it is sufficient to analyze the trends of the $\text{PSD}_{p'p'}$ in Figure 3.13: the most important variation in the power spectra of the pressure fluctuations due to the porous material is confined to the low Strouhal number region, like for both components of the velocity fluctuations.

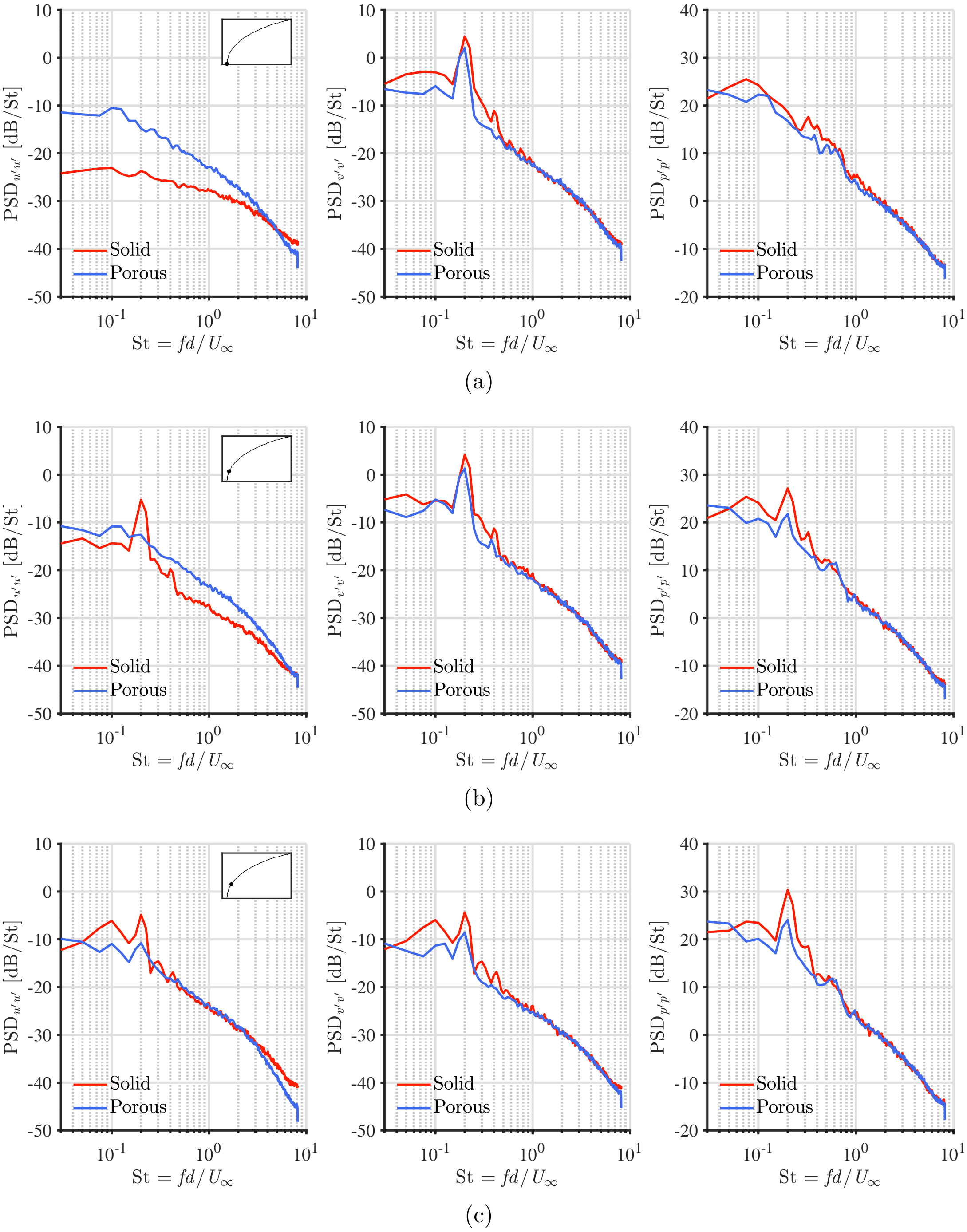

(a)

(b)

(c)

Figure 3.13: Normalized PSD of the streamwise component (on the left) and the upwash component (in the center) of the velocity fluctuations, compared with the PSD of the wall-pressure fluctuations (on the right) for the solid (red lines) and the porous (blue lines) case. The velocity data were normalized with the respective values at $x/r_{LE} = -4$ before computing the Power Spectral Density.

For each position, the trends of the solid and porous configurations are influenced by the respective curves of u' and v'. In fact, at the stagnation point in Figure 3.13(a) both cases do not show the peak at $St = 0.2$ as occurs for the streamwise velocity component, but at the same time the $\mathrm{PSD}_{p'p'}$ for the porous airfoil converges to the solid one as occurs in the upwash velocity component. This may be linked to the fact that, since the pressure is oriented perpendicular to the surface of the airfoil, at $y = 0$ the normal direction coincides with the x axis and consequently the influence of u' is preponderant.

Proceeding along with the leading-edge, the influence of the upwash component of the velocity fluctuations increases, bringing out the vortex-shedding peaks in the PSDs of the wall-pressure fluctuations for both the solid and porous cases. The difference between the two curves is evident and is even more pronounced at $y = 0.23d$, where the maximum attenuation of 6 dB is achieved. In conclusion, the beneficial effect of the porous treatment also occurs beyond the point of maximum p'_{rms} and the analysis on the wall-pressure fluctuations confirms that the porosity determines not negligible mitigation of the aeroacoustic leading-edge noise at low frequencies, which depends on the turbulence distortion phenomenon.

3.2.3 Vorticity and Γ_2 function

With the instantaneous velocity data, it is still possible to carry out a final analysis that is linked to the turbulence, present in the flow field and generated by the rod upstream of the airfoil. The vortex structures that detach alternately from the upper and lower part of the rod surface, due to the separation of the boundary layer, constitute the turbulent flow that interacts with the NACA-0024 model located downstream. The vorticity can be explained as the tendency of a turbulent stream to bend, rotate and contort instead of continuing in a straight line, forming eddies that can have different sizes. Mathematically, the vorticity is defined as the rotor of the flow velocity vector:

$$\omega_z = \nabla \times \mathbf{U} \tag{3.8}$$

where the subscript z indicates the direction along which ω develops.

Using the *curl* function already implemented in MATLAB for the calculation of vorticity, which requires as input the spatial coordinates of the midspan plane and the instantaneous values of the components u and v, the results shown in Figure 3.14 are obtained. In this case, different time instants between the two configurations were used so that similar vorticity-field conditions were represented: indeed, the purpose of this analysis is to capture the shape of the eddies approaching the airfoil leading-edge, verifying the turbulent nature of the incoming flow.

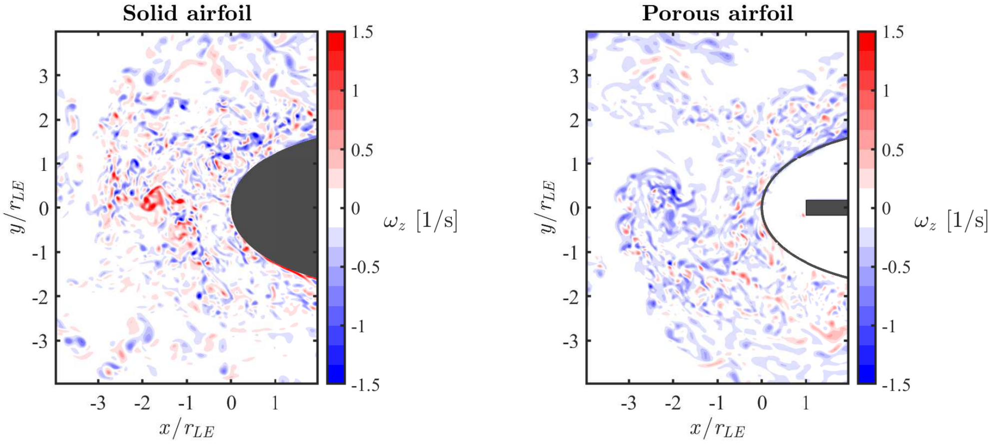

Figure 3.14: Instantaneous fluctuating z-vorticity in the stagnation region for both solid and porous configurations, taking into account two different time instants.

In both maps, the vortex core is clearly observed, which in the solid case assumes a positive value while in the porous one it is negative. The choice of pointing out the different sign of ω_z with the two-color scale is not fortuitous: indeed, given the periodic alternation with which the vortex structures are detached from the surface of the rod, also the downstream wake is characterized by this ordered succession of eddies that is reflected in the alternating approach of positive and negative vorticity towards the airfoil. If in the time instant captured for the solid model the vortex core, characterized by the red circular zone, is clearly evident, for the porous one the clockwise rotation of the approaching turbulence is also denoted through the white region, that surrounds the central part and seems to follow the flow direction. This detail allows for the association between the direction of rotation and the sign of the vorticity: the red positive sign corresponds to the vortices that rotate counterclockwise, while the blue negative sign indicates those that rotate clockwise.

Having available 1270 time instants for both numerical simulations, it was also possible to evaluate the mean value of vorticity and compare the results between the solid and the porous cases. Figure 3.15 shows the $\bar{\omega}_z$ maps near the leading-edge, because it is around the surface of the airfoil that the most relevant differences are observed. On the solid surface, the mean vorticity distribution is concentrated in a confined region unlike what occurs around the porous airfoil, where instead the same quantity seems to spread over a wider area. It is assumed that this aspect depends on the different thickness of the boundary layer, already observed in the mean streamwise velocity maps in Figure 3.7(a): the thicker boundary layer induced by porosity determines a greater $\bar{\omega}_z$ diffusion in the area surrounding the leading-edge. Furthermore, it is evident that the mean vorticity on the outer surface is not transmitted through the porous material inside the wing profile structure, even if it reappears along the solid centerplane.

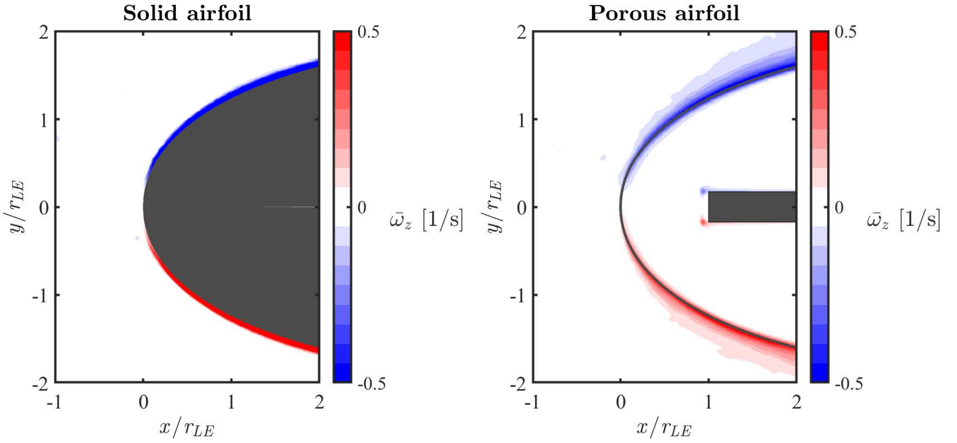
Solid airfoil

Porous airfoil

Figure 3.15: Mean value of z-vorticity in the stagnation region for both solid and porous configurations, obtained by averaging the instantaneous ω_z over 1270 time instants.

To complete the turbulence analysis, the Γ_2 scalar function proposed by Graftieaux et al. [17] has been implemented, to define further geometric characteristics of the large-scale eddies. In fact, it is a vortex core identification algorithm that derives from the velocity field and which allows focusing exclusively on the large scale, leaving out the information contained in the smaller vortices. The equation, with which the Γ_2 function is determined, is the following:

$$\Gamma_2(P) = \frac{1}{S}\int_{M\in S} \frac{[PM \wedge (U_M - \bar{U}_P)] \cdot z}{|PM| \cdot |U_M - \bar{U}_P|}\, dS \tag{3.9}$$

where P is a fixed point in the measurement domain, S is a two dimensional area surrounding P and containing the other point M and PM indicates the radius vector between them. U_M and $\bar{U}_P$ are respectively the instantaneous velocity vector at point M and a local convection velocity, which is calculated as

$$\bar{U}_P = \frac{1}{S}\int_S U\ dS \tag{3.10}$$

For practical applications, the Γ_2 function is approximated by considering S as a rectangular area of fixed size and centered at the point P:

$$\Gamma_2(P) = \frac{1}{N}\sum_S \frac{[PM \wedge (U_M - \bar{U}_P)] \cdot z}{|PM| \cdot |U_M - \bar{U}_P|} \tag{3.11}$$

where N is the number of points M inside S and plays the role of a spatial filter.

Figure 3.16 shows the results obtained after implementing the Equation 3.11 again with the MATLAB script. In the present case, the measurement domain is defined by 500 points per side and the area S is a 90x90 points square: the more this size increases, the more it is possible to better capture the boundaries of the large-scale eddies. Moreover, the same time instants used to plot ω_z field and also the same *colorbar* have been chosen, in order to maintain the same color convention to indicate the vortex direction of rotation.

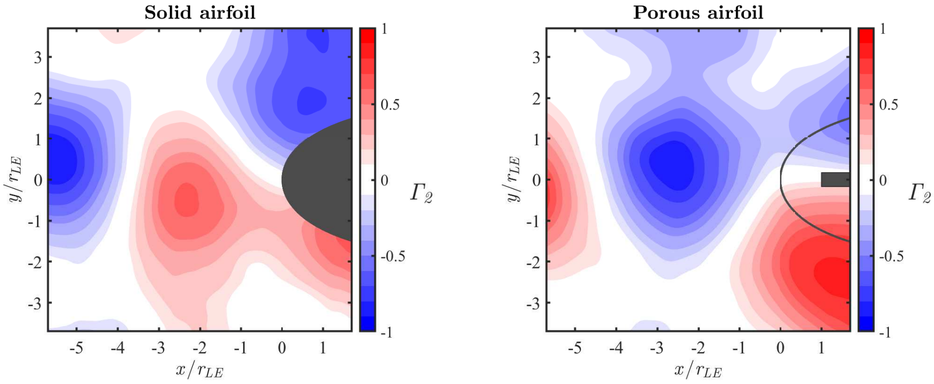

Figure 3.16: Instantaneous Γ_2 function in the stagnation region for both solid and porous configurations. The plotted time instants are the same as those used in the ω_z maps.

As for the vorticity, also for the Γ_2 algorithm, the aim is to provide additional information on the characteristics of the turbulence without making a direct comparison between the two airfoil configurations. This function varies in the range between -1 and 1 and the contours marked in the maps represent the distinct levels of rotational intensity, which characterize an eddy. The more intense color identifies the center, while the lighter one that emerges from the white background can be assimilated to the outer boundary of the vortex structure. From the frames plotted in Figure 3.16, it is observed that the large-scale eddies do not break when they impact the leading-edge, but they are deformed around the surface of the airfoil. Furthermore, it seems that the counterclockwise structures always go downward along the pressure side, while the clockwise ones go upward along the suction side.

In conclusion, the analysis of vorticity and Γ_2 function provides a clear and immediate visualization of the vortices present within the turbulent flow. The main variations between the solid and porous model were found for the $\bar{\omega}_z$ distribution around the surface of the airfoil, due to the higher boundary layer thickness linked to the porous treatment. Surely the current setting of the function is not the optimal one, but the situation could improve by varying the number of points and the size of the area S, two important parameters that in this case have been adapted to the available LES numerical data.

3.3 Calculation of surface-normal velocity

From Figure 3.13 it is found that the power spectra of the wall-pressure fluctuations depend on u' and v' in different degrees according to the position considered along the surface of the airfoil. In particular, it seems that the contribution of each component of velocity fluctuations is related to their value assumed in the direction normal to the wall. This has led to thinking, following Amiet's theory [2], that it would be more suitable to compare the trend of the p'_{rms} directly with the fluctuations of the surface-normal velocity component. This quantity represents the link between the analysis carried out so far with the pressure and velocity data.

The normal velocity is calculated as a vectorial sum starting from the three instantaneous velocity components extracted from the horizontal planes at the point closest to the surface of the airfoil, i.e. in the same positions indicated in Table 3.3. The procedure to determine this parameter is as follows:

$$U = \sqrt{u^2 + v^2} \tag{3.12}$$

$$V = U \sin\theta \tag{3.13}$$

From Figure 3.17 it can be clearly seen how the various quantities appearing in the equations above are directed and what each of them represents. The red arrow corresponds to the normal velocity V, while the blue one indicates the instantaneous velocity U calculated for one of the points of the surface through its components u, v and w. Actually, the spanwise contribution is not used, since it has been verified that it is negligible for the results as already discussed in Section 3.2.1. Once the instantaneous velocity is obtained, this is multiplied by the sine of the angle θ that U forms with the grey line, which is the tangent to the airfoil at that point; therefore, the desired normal component is easily computed.

To carry out what has just been explained, a new MATLAB function implemented by Taylor et al. [45] has been used, which is called *findPointsNormal*: it requests as input the spatial coordinates of the suction side and the components u, v and w and returns all the information relating to the vector V, which are intensity and direction. Since the function is based on instantaneous data, what is achieved is the instantaneous surface-normal velocity that can be divided again into its mean and fluctuating contributions through Reynolds decomposition. This operation is necessary because the main interest is related to the trend of the V' fluctuations, which is expected to be intermediate between that of u' and v'.

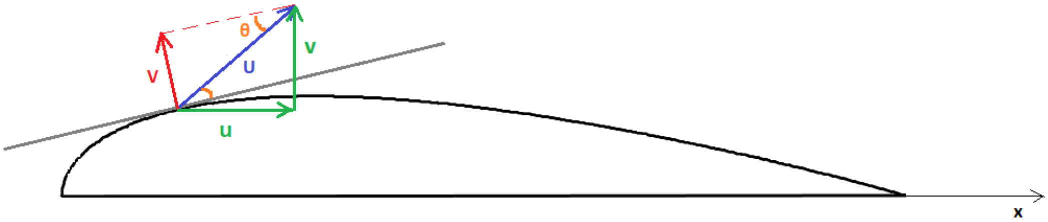

Figure 3.17: Representation of the surface-normal velocity at a generic point along the suction side of the NACA-0024 wing profile.

3.3.1 Comparison between the power spectral densities of normal velocity and pressure fluctuations

As previously mentioned, the normal velocity fluctuations are computed using the data belonging to the three horizontal planes available from the numerical simulations and, in particular, the values of the points closest to the surface of the airfoil, whose coordinates are already reported in Table 3.3. Now the purpose is precisely to evaluate the PSD of the velocity fluctuations in the normal direction and compare it with that already obtained of the wall-pressure fluctuations. Therefore, it is necessary to consider the same positions as before and the motivation for choosing points on the horizontal planes and not on the surface itself is the same already expressed in Section 3.2.2.

The power spectra of the normal velocity fluctuations ($\text{PSD}_{V'V'}$) are computed with the Welch method and with the same window and overlap parameters used for pressure data. Furthermore, the comparison between normal velocity and wall-pressure fluctuations is evaluated for both solid and porous cases in the usual three specific locations, i.e. $y = 0$ (a), $y = 0.17d$ (b) and $y = 0.23d$ (c). The results shown in Figure 3.18 constitute the heart of this work, because they confirm the physics behind the leading-edge noise reduction due to the implementation of porous materials: for the first time, the hypothesis that turbulence distortion may be one of the physical mechanisms responsible for the noise reduction seems to be demonstrated.

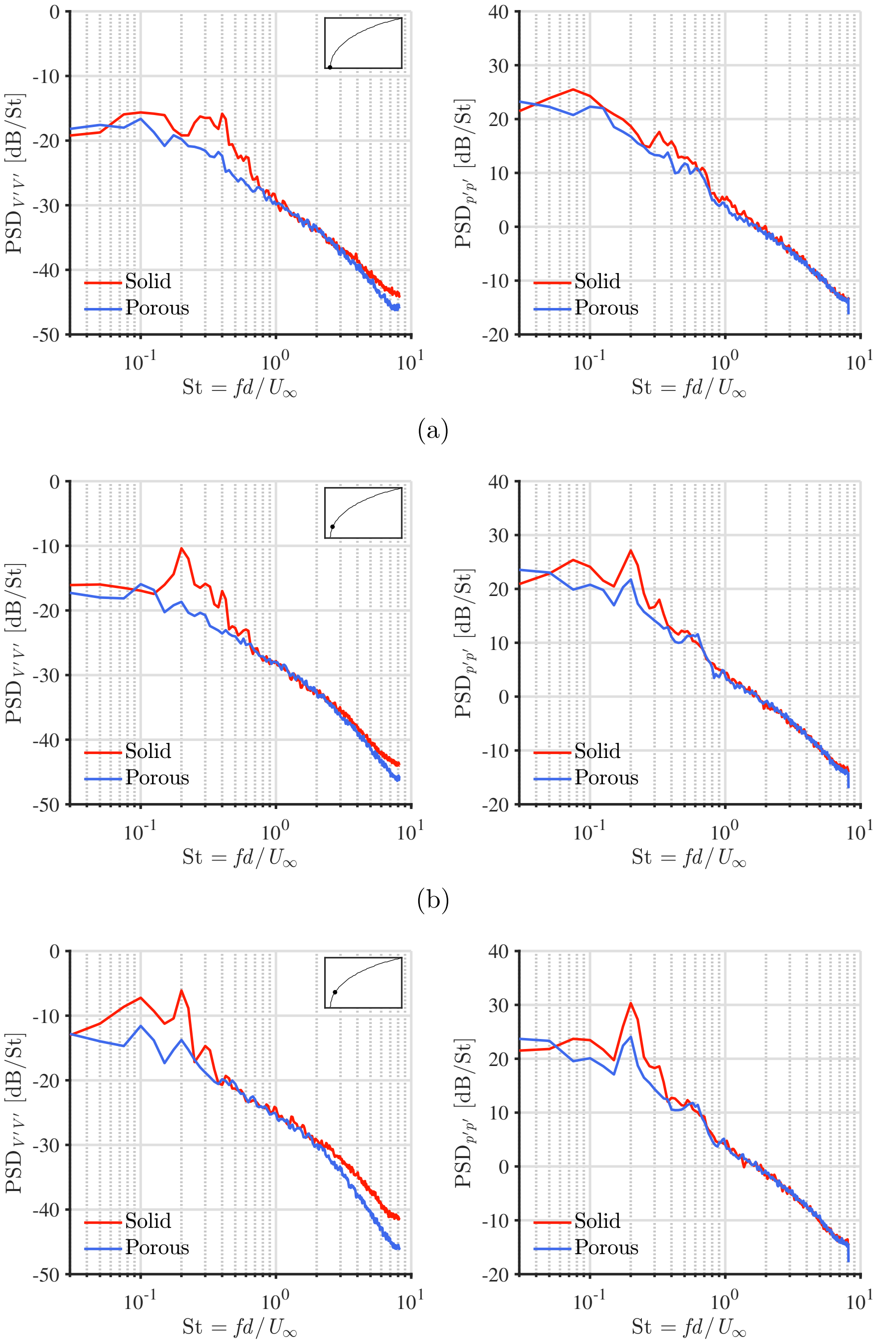

(a)

(b)

(c)

Figure 3.18: Normalized PSD of the surface-normal velocity fluctuations (on the left) compared with the PSD of the wall-pressure fluctuations (on the right) for the solid (red lines) and the porous (blue lines) case.

Since, as expected, the surface-normal component depends on the contribution of u' and v' fluctuations, the not-overlapping problem between the curves of the two configurations was again found in these power spectra. Therefore, it was necessary to introduce a specific corrective factor that would eliminate this discrepancy and allow to plot the velocity trends correctly. In Figure 3.18 the $\text{PSD}_{V'V'}$ already normalized are shown directly in comparison with the PSD of the wall-pressure fluctuations. It is immediate to observe that surface-normal velocity and wall pressure have similar PSD trends, for both solid and porous airfoil at each analyzed position. The fact that the trend of their fluctuations is almost identical along the whole range of frequencies considered is a confirmation of the dependence between these two quantities: thus, the normal velocity component is the one connected to the pressure.

The aspect on which more attention needs to be focused, however, is as always the difference between the PSDs of the two configurations, which provide important information on the effects due to the porous treatment. Both surface-normal velocity fluctuations and wall-pressure fluctuations show a decrease between the solid and the porous case that mainly affects the low frequencies and in particular the range at $St < 0.4$, whereas at higher Strouhal numbers the trends overlap perfectly. At the stagnation point (Figure 3.18(a)) neither of the two curves shows the vortex-shedding peak, but there is already an evident reduction for the porous airfoil. Instead, in Figure 3.18(b) the $\text{PSD}_{V'V'}$ for the solid case is characterized by the peak at $St = 0.2$ which is totally absent in the porous one, causing a greater attenuation precisely in the point where the noise sources should be. Finally, even at $y = 0.23d$, the porous configuration seems to efficiently dampen the surface-normal velocity fluctuations, since the slight increase that stands out around the vortex-shedding frequency remains, in any case, lower than for the solid one. As deduced from the streamwise and upwash velocity fluctuations and from the pressure fluctuations, the mitigation due to porosity also continues downstream of the maximum p'_{rms} point and is confirmed by the analysis of V'.

Therefore, the use of a porous insert in the wing profile structure produces a reduction of the surface-normal velocity in the low-frequency range, which is linked to the attenuation of the turbulence distortion [50]. In fact, according to Hunt's theory [21], the two ways in which a body can modify the turbulence of the incoming flow that interacts with it are the pressure exerted on the flow itself and the distortion of the vorticity field. As demonstrated by the results obtained in Figure 3.10, due to the penetration of the flow inside the porous structure of the airfoil, both the streamwise and the upwash fluctuations do not reach a zero value at $x/r_{LE} = 0$; this aspect leads to the conclusion that a porous body exerts less pressure on the incoming stream, which is reflected in a variation of u', v' and consequently of the surface-normal velocity fluctuations. Moreover, in

Section 3.2.3, it was seen how porosity influenced the mean vorticity distribution on the surface of the porous airfoil, spreading it over a wider region around the leading-edge than in the solid case.

In conclusion, the attenuation of turbulence distortion due to porosity is linked to the reduction of $\mathrm{PSD}_{V'V'}$ trends, which occurs in the same St range in which wall-pressure fluctuations are mitigated. Thus, it is possible to assume that the abatement of the leading-edge noise is partly due to the mechanism of distortion of turbulent eddies. This result is encouraging and could be the starting point for future studies in this field.

3.3.2 Cross-coherence between V' and p'

After having demonstrated, through the PSDs, that pressure and normal velocity fluctuations are characterized by a similar attenuation in the same frequency range, it was decided to apply other correlations to these data and subsequently compare the results of the two configurations. The cross-coherence is the first analysis carried out by taking the values of V' and p' at the usual three positions along with the wing profile. Its definition is similar to Equation 3.4, with which the spanwise coherence of the wall-pressure fluctuations is computed in Section 3.1.2: in this case, however, the CPSD is evaluated with the data of the two different quantities referred to the same spatial point and the denominator reports the product between the PSDs of V' and p'. The *mscohere* MATLAB function is used to calculate the cross-coherence, which requires as input not only the fluctuations data but also specific parameters such as the sampling frequency and the Hamming function with a window of 512 samples and a default overlap of 50%. Since the values involved are few and the motion field is two-dimensional, the cross-coherence is computed for all the points along the spanwise direction at the x/r_{LE} and y/r_{LE} coordinates set in Table 3.3 and 3.4 and later averaged to obtain smoother curves.

The purpose of this function is to examine the relation between two signals, here the surface-normal velocity and the wall-pressure fluctuations, and the results are shown in Figure 3.19, proceeding as always from the stagnation point at $y = 0$ (a), to $y = 0.17d$ (b), and finally to $y = 0.23d$ (c). The indication on the level of compatibility between the two quantities is given by the cross-coherence value that is returned: the closer it is to unity, the stronger is the relationship between them. Now the focus is on the low-frequency range, where the greatest attenuation of aeroacoustic noise has been observed and where it is expected to find a significant difference between the trend of the solid airfoil and that of the porous one; indeed, at high St values, the two curves are overlapped and in all three locations their cross-coherence is equal to approximately 0.35.

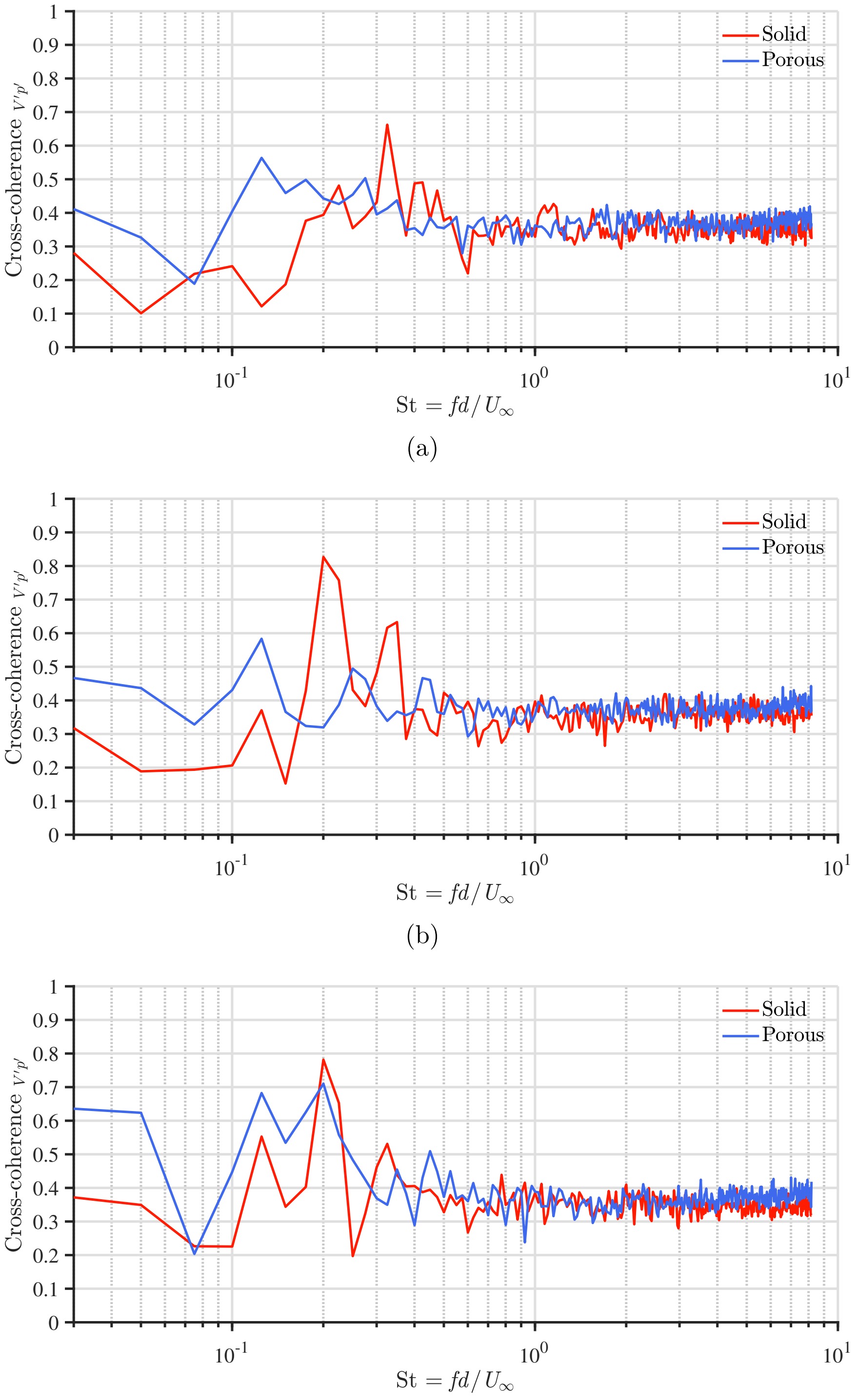

(a)

(b)

(c)

Figure 3.19: Cross-coherence between wall-pressure fluctuations and surface-normal velocity fluctuations for the solid (red line) and the porous (blue line) airfoil. The results are extracted at three different locations along the leading-edge curvature, i.e. (a) $y = 0$, (b) $y = 0.17d$ and (c) $y = 0.23d$.

At the stagnation point, the cross-coherence value is not particularly high and, around the vortex-shedding frequency, it oscillates between 0.4 and 0.5 for both configurations. Moreover, it appears that V' and p' have a stronger relation in the porous case, as observed from the top curve. Moving along the leading-edge, at the position where the pressure fluctuations are maximum, a different trend can be observed. While in the porous case the cross-coherence does not undergo particular variations, the solid one shows a maximum at $St = 0.2$ that exceeds the value of 0.8. This represents the biggest difference between the solid and porous case, suggesting that pressure and normal velocity lose their correlation around the vortex-shedding frequency as a consequence of the porous treatment, similarly to what is observed in the spanwise coherence of p'. Lastly, at $y = 0.23d$ there is almost a total cancellation of the deviation between the two curves, which depends on the increase of the analyzed parameter in the porous model since in the solid one it remains almost equal to that at $y = 0.17d$.

Therefore, from all three graphs in Figure 3.19, it can be observed that also the cross-coherence as the PSDs of the surface-normal velocity and wall-pressure fluctuations shows a greater reduction always at $y = 0.17d$ and especially in the same low-frequency range. It remains to be understood what is the link between mitigation of aeroacoustic noise, attenuation of turbulence distortion, and reduction of cross-coherence between V' and p'. Surely both quantities are varied by the penetration condition due to porosity, but the reason for the loss of cross-coherence remains unclear.

3.3.3 Causality correlations between V' and p'

The latest analysis carried out between wall-pressure and surface-normal velocity fluctuations corresponds to a particular correlation used by Henning et al. [18], which is called *causality correlation* and is defined by the following equation:

$$R_{V'p'}(\mathbf{xy}, \tau) = \frac{\Phi_{V'p'}(\mathbf{x}, \mathbf{y}, \tau)}{V'_{rms}(\mathbf{x})p'_{rms}(\mathbf{y})} = \frac{|V'(\mathbf{x}, t) \cdot p'(\mathbf{y}, t+\tau)|}{\sqrt{|V'(\mathbf{x}, t)|^2 \cdot |p'(\mathbf{y}, t)|^2}} \tag{3.14}$$

where $\Phi_{V'p'}$ represents the CPSD between V' and p', which is normalized by the product of the root mean square values of the same fluctuations, denoted with the subscript rms. The normal velocity data are measured at the position $\mathbf{x}$ at instant t, while the pressure data are relative to position $\mathbf{y}$ and instant $t + \tau$ where τ corresponds to the time shift between the two signals.

This correlation was introduced in the study mentioned before to investigate the link between the near-body velocity and the far-field pressure information. Among the various cases discussed in this work, there is also the rod-airfoil configuration: the authors studied the trend of p' fluctuations, acquired through microphones positioned at a certain distance from the airfoil to acquire far-field noise, and that of u' and v' fluctuations in the leading-edge region measured through the PIV technique. However, in the present case, Equation 3.14 has been implemented for the evaluation of the causality correlation between surface-normal velocity and wall pressure in order to achieve results similar to those of Henning et al. [18], because it is expected that far-field noise depends on the wall-pressure fluctuations.

The graphs in Figure 3.20 show the results obtained with the LES numerical values in the usual three positions along the surface of the NACA-0024 wing profile. From what is highlighted in the reference article, at the stagnation point the coefficient $R_{V'p'}$ should be characterized by an oscillating trend with a sinusoidal shape that reaches its maximum with a value of $|0.3|$ in correspondence with $\tau = 0$ ms. Moreover, the distribution as a function of the time shift appears symmetrical with respect to the maximum point and without skewness. From what is plotted in Figure 3.20(a), in this case, at $y = 0$ the situation does not seem to respect what has just been described and verified by the previous studies, because neither the solid nor the porous curve define a sine-type oscillation: their trend is totally random along the τ range and the porous one reaches greater positive and negative peaks than in the solid case. The difference could be due to consideration of wall-pressure fluctuations rather than in the far-field, but the total absence of a maximum at $\tau = 0$ ms raises many doubts.

Moving along the airfoil, a change in the curves of the solid model is observed which assumes a trend that increasingly resembles the sinusoidal one, especially at $y = 0.23d$: the maximum point emerges at $\tau = 0$ ms and a more symmetrical distribution is noted. The most important detail that catches the attention, however, is the progressive increase in the amplitude of the curves, which go from a maximum of $|0.3|$ up to $|0.5|$ for both configurations. Indeed, although the porous case continues to show the same random trend as the one at the stagnation point, it is characterized by this gradual increase in values too.

Since the results described by Henning et al. [18] are limited to the stagnation point only, it is not possible to make a direct comparison with what is obtained in Figure 3.20 but some interpretations can still be drawn, which may be deepened in future studies. The fact that for the porous configuration the trends always remain similar to each other, with a simple increase in amplitude moving around the leading-edge, can be seen as a confirmation that the correlation between surface-normal velocity and wall-pressure fluctuations does not undergo strong variations due to porosity, unlike what happens for the solid structure. Furthermore, as already discussed in all previous analysis, the greatest effect of the porous treatment always occurs at $y = 0.17d$ and $y = 0.23d$: the absence of a sine-type distribution could be linked to a weaker correspondence between the p' and V' trends, which is reflected in the minor cross-coherence in Figure 3.19.

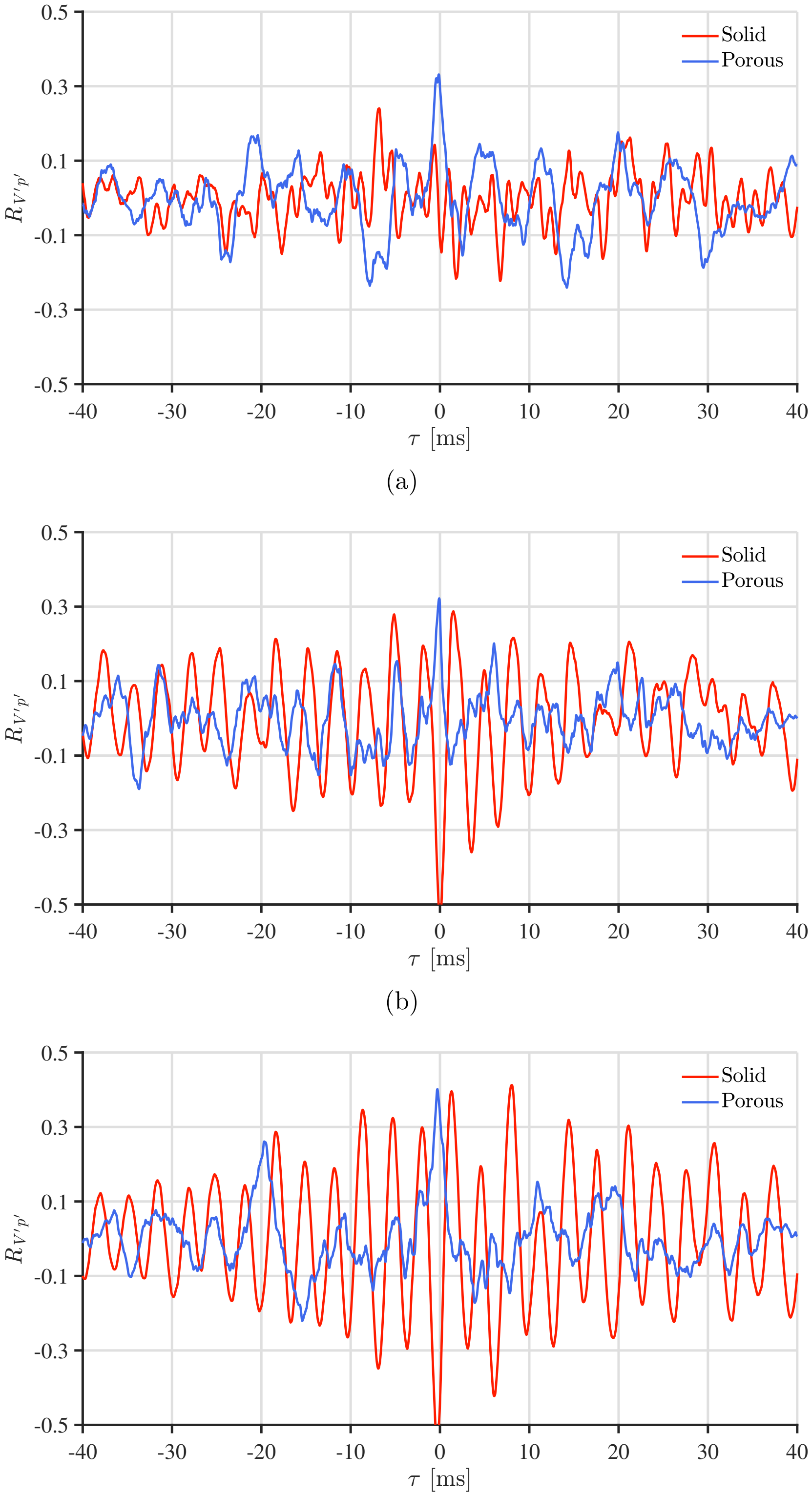

(a)

(b)

(c)

Figure 3.20: Causality correlation coefficient $R_{V'p'}$ between wall-pressure fluctuations and surface-normal velocity fluctuations for the solid (red line) and the porous (blue line) airfoil. The results are related to three different locations along the suction side, i.e. (a) $y = 0$, (b) $y = 0.17d$ and (c) $y = 0.23d$.

Chapter 4

Experimental activity

This chapter describes the work carried out in one of the VKI facilities and shows the results obtained: as already mentioned in the introductory part, the aim was to experimentally verify the analysis conducted on the numerical LES data by testing a NACA-0024 wing profile model in the wind tunnel. Unfortunately, due to the ongoing global health emergency, the laboratory activity was postponed for a few months and the time available was not sufficient to solve the problems in the microphones calibration and then to continue with the experimental campaign. Therefore, what is shown below are the achievements concerning the calibration chain designed and implemented at the von Karman Institute.

4.1 Experimental setup

The idea of mounting a series of microphones on an airfoil model to measure pressure fluctuations is totally innovative, but requires a reliable and robust calibration chain that provides the Transfer Function (TF) to eliminate the resonance phenomena, induced by the cavities hosting the microphones. Before commenting on the results of the experimental activity, it is necessary to indicate which instruments were used for the measurements and how they were included in the calibration procedure, also reporting a brief description of the overall operating principle.

4.1.1 Airfoil NACA-0024 model

As indicated in Chapter 2, the large-eddy simulations are based on an experimental setup already prepared and tested at the VKI, from which all the geometric information then used in the numerical work has been extrapolated, starting from the dimensions of the airfoil models. Indeed, because of the previous study [50], both the solid and the porous configuration of a symmetric NACA-0024 wing profile model were created: in that case, only velocity measurements were made using the hot wire anemometry and no microphones were installed along the surface to detect the instantaneous pressure, from which to calculate the fluctuations.

The airfoil models are characterized by a chord length of 157 mm and a span of 200 mm, with a maximum thickness of 38 mm. Figure 4.1 shows the solid model, which is the only one used in the laboratory since the calibration procedure of the microphones would have been the same for both configurations. In any case, the porous version has already been designed following the indications resulting from the analysis of the possible materials.

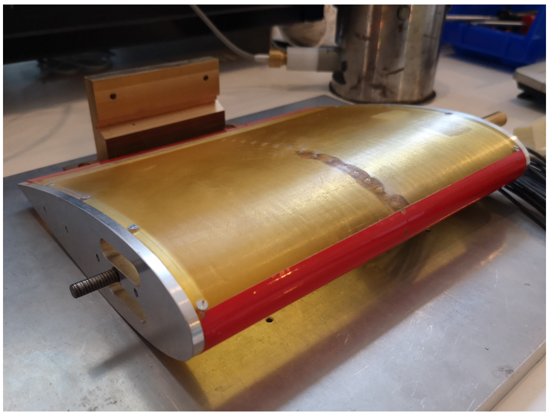

Figure 4.1: Solid model of the NACA-0024 airfoil used for the microphones calibration.

The choice of the porous material with which to create the wing profile model required a careful analysis of all the parameters that characterize the porosity, such as:

- *Static air-flow resistivity* σ, which is a measure of the resistance that the air encounters as it passes through the material, defined as the ratio between the pressure drop across a porous sample and the product of flow velocity with sample thickness.

- *Porosity* φ, defined as the ratio between the volume of the fluid contained in the open pores and the total volume occupied by the sample.

- *Tortuosity* α, which describes the complexity of the path connecting two points within the porous material.

Those shown in the list above are only the most important parameters for the definition of a porous material. Taking them into account, the melamine foam was chosen to fill the internal part of the porous airfoil model and its characteristics are reported in Table 4.1.

Table 4.1: Porous parameters characterizing the melamine foam integrated in the porous airfoil model.

$\boldsymbol{\sigma}$ $[\mathbf{Pa \cdot s \cdot m^{-2}}]$	$\boldsymbol{\varphi}$ $[-]$	$\boldsymbol{\alpha}$ $[-]$
8.683×10^3	0.986	1.02

Both versions of the model consist of a hard plastic exoskeleton in order to maintain the NACA-0024 shape integrity and a metallic wire mesh, added as an external layer to ensure the same surface roughness in the two cases. These two elements are characterized by a static air-flow resistivity that can be considered negligible compared to that of melamine foam, hence only the latter material affects the properties of the porous configuration. In the internal part of the porous structure, in addition to the melamine foam that fills most of the volume, a hard plastic centerplane is also installed along the chord line to avoid the cross-flow between the pressure and suction side: this expedient ensures that the aerodynamic properties remain unchanged, even when the airfoil is positioned with a no-zero angle of attack with respect to the incoming flow. The centerplane is installed starting from the trailing-edge but does not extend up to the leading-edge leaving a distance equal to a radius of curvature, so that the air stream can partially enter the structure at the stagnation point.

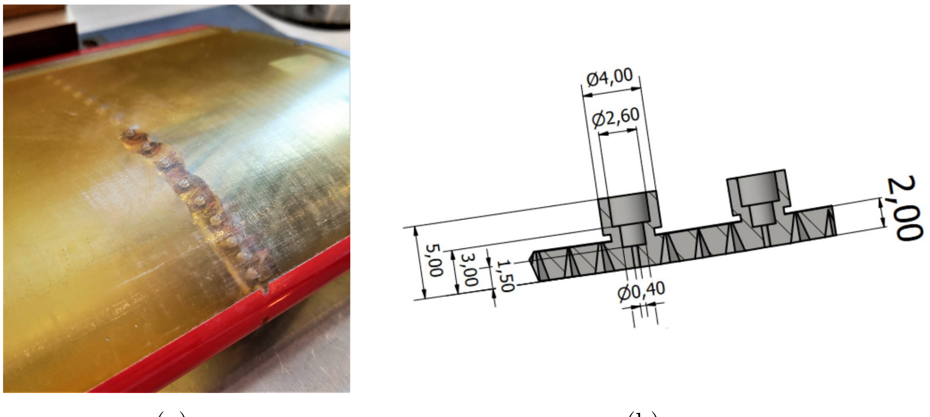

(a) (b)

Figure 4.2: Electret microphones embedded on the surface of the airfoil model, positioned along both sides at the midspan (a): the detailed CAD section of the microphones housing (b) is necessary to apply the Bergh and Tijdeman model.

Compared to the model used for the tests with hot wire anemometry, the one designed for this study involves the addition of the microphones necessary to measure the wall pressure. These microphones are mounted exactly in the middle of the span as shown in Figure 4.2(a), both on the pressure and suction side of the airfoil, starting from the leading-edge and proceeding downstream. In total 21 microphones are embedded on the surface, one of which is positioned precisely at the stagnation point and the others distributed over and under but not symmetrically, otherwise it would not be useful since the chosen wing profile is already symmetrical. Therefore, several cavities are drilled in the hard plastic exoskeleton to accommodate the microphones, as shown in Figure 4.2(b): the CAD section assumes that the external part is at the bottom, since the cavity observed on the surface is precisely the one with the smallest diameter, while the inside of the structure faces upwards where the largest cavity that houses the microphone is located.

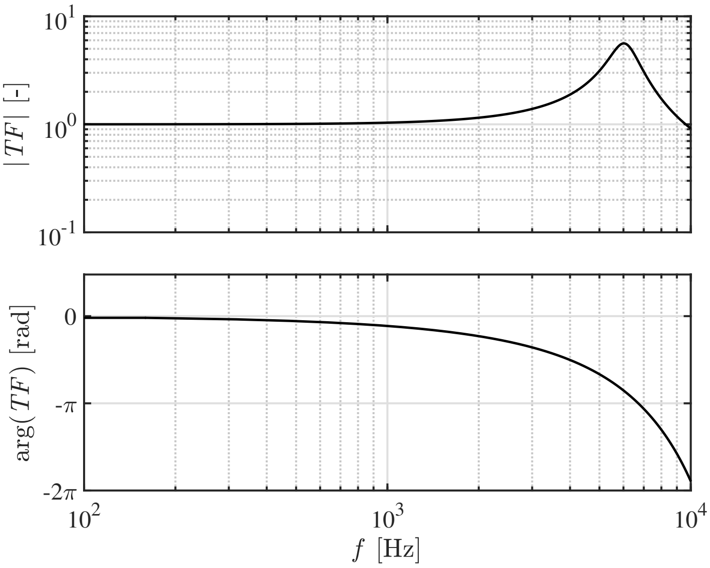

Figure 4.3: Theoretical estimation of the frequency response for the cavity of microphones embedded on the airfoil surface. The Bergh and Tijdeman model has been used considering the geometrical parameters that characterize the microphones housing.

The frequency response of a sequence of channels and cavities can be predicted by a theoretical tool implemented according to the work of Bergh and Tijdeman [7]: the model is based on the Navier-Stokes equations, assuming small sinusoidal disturbances, laminar flow and a long aspect ratio of the tubes considered. Figure 4.3 shows the transfer function obtained with the geometrical parameters of microphones housing indicated in Figure 4.2(b). The model predicts a dynamic response dominated by a resonance peak, that occurs at $f \simeq 6$ kHz. The location of this maximum point is highly dependent on the volume of the cavity facing the microphone, which means that any slight gap in the installation of the microphones would generate a different resonance frequency. Precisely for this reason, through the calibration chain, it is necessary to find the correct transfer function that suppresses the peak present in the frequency response and removes any errors induced by resonance phenomena.

4.1.2 Instrumentation

The calibration chain requires different instruments to generate, measure, and acquire the acoustic signals necessary for the evaluation of the final transfer function.

- *Cylindrical calibrator*

  This device consists of a steel cylinder that presents drilled channels inside the structure and it features a loudspeaker on its top. The largest channel with a diameter of 13 mm allows the acoustic waves, emitted by the loudspeaker, to reach a microphone installed directly in front of it and another one prepared on the cylinder side. Given the geometric configuration of the calibrator used, plane wave propagation is ensured up to the cut-off frequency of 15.152 kHz. It is used in the first two steps of the calibration chain, positioning it as shown in Figure 4.4 on the calibration plate in correspondence with the microphones involved in the measurement.

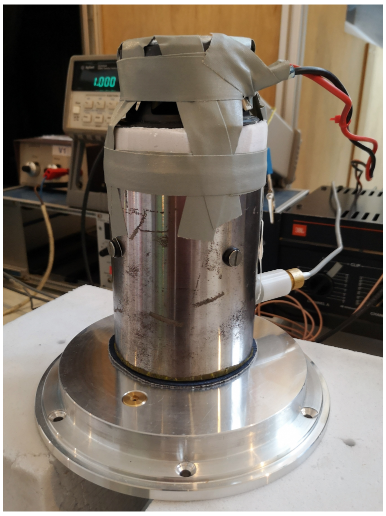

Figure 4.4: Cylindrical calibrator used in steps 0 and 1 of the microphones calibration chain.

- *Conical calibrator*

  This second device is necessary to calibrate the microphones embedded on the surface. Basically, it is a similar version of the cylindrical calibrator, where the full steel structure surrounding the inner channels has been removed and the cavity diameter has been reduced to 3 mm. When applied to the last step of the calibration chain, this calibrator must be used together with an appropriate mask, designed to surround the airfoil and maintain the calibrator in position during the acquisitions. This mask features holes through which the calibrator can be centered above all microphones embedded on the surface to calibrate them, as can be seen in Figure 4.5(b).

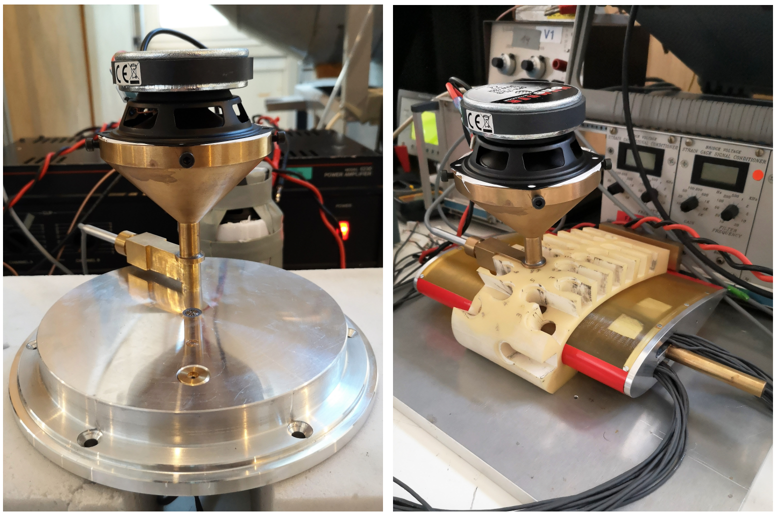

(a) (b)

Figure 4.5: Conical calibrator used in step 2 (a) and step 3 (b) of the microphones calibration chain. The mask placed on the airfoil model is used to keep the calibrator firm during the acquisition.

- *Bruel & Kjaer (B&K) microphone - Type 4938*

  This microphone is characterized by a diameter equal to 1/4 of an inch and it is highly accurate over a wide range of frequencies, defined approximately between 4 Hz and 70 kHz. These devices are used in each step of the calibration chain, because they are those installed on the side microphones of the calibrators and on the calibration plate, one flush mounted and the other pinhole. Before proceeding with the measurements, this type of microphone is calibrated through a Pistonphone Type 4228.

- *Knowles electret microphone - Model FG23329-P07*

  This is the type of microphone equipped along the surface of the airfoil model, as it is characterized by its limited intrusiveness given the diameter of only 2.59 mm. The electret microphones provide a reliable response in the frequency range between 100 Hz and 10 kHz, but before being acquired the output signal must be modified by an amplifier with a suitable gain. Moreover, a special adapter manufactured at VKI is used to reduce electromagnetic noise, which can alter the final result.

- *Calibration plate*

  The circular plate is used in the first three steps of the calibration chain and 5 different types of microphones are installed on it, as this instrument is designed for several experiments. However, in the present study, only two of these are necessary for the procedure and are indicated with an arrow in Figure 4.6: the one with a larger diameter corresponds to the reference B&K microphone, with respect to which the transfer function is evaluated, while the smaller hole with a diameter of 2 mm constitutes the pinhole configuration of another B&K microphone used in steps 1 and 2.

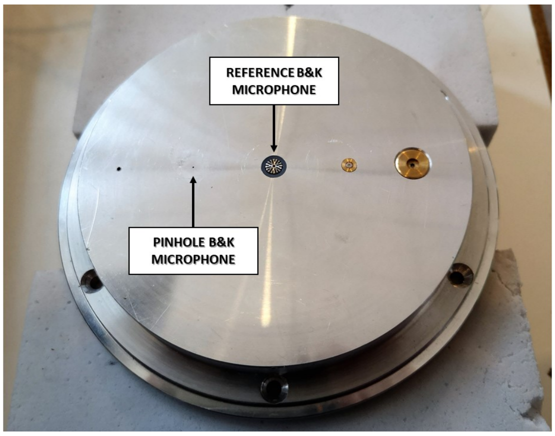

Figure 4.6: Calibration plate where both the reference microphone and the one mounted in pinhole configuration are installed.

Those just described constitute the specific instruments for the calibration procedure of the microphones embedded on the surface of the airfoil model, but to generate the initial signal and acquire the response of the microphones it is necessary to prepare an appropriate acquisition chain, such as the one schematized in Figure 4.7.

The *Agilent 33120A signal generator* is the main device for creating and defining the characteristic parameters of the acoustic signal that is fed to the loudspeakers on top of the calibrators. Different types of signals, such as white noise or sweep, can be chosen and then it is possible to change the values of amplitude, duration of a period, initial and final frequency, etc. The Agilent generator is connected to the *JBL UREI 6230 power amplifier*, which allows finding the right balance between maximizing the signal to the acquisition and avoiding the microphones saturation.

All the microphones used in each step generate output signals that must be processed by a specific amplifier, depending on the microphone model: indeed, for the B&K type the *NEXUS Charge amplifier - Type 2692A* is introduced, while for the electret of the airfoil a special amplifier designed at the VKI is used to process the signal of these microphones. Finally, these devices are connected to the acquisition system *NI-PXI 1082 chassis* through a number of channels equal to the microphones involved in the calibration chain. This instrument is connected to the PC where the *LabView software* is installed, which allows the visualization of the acoustic signals detected by the microphones and sets the acquisition parameters, such as the sampling frequency and the acquisition time, before starting the measurement.

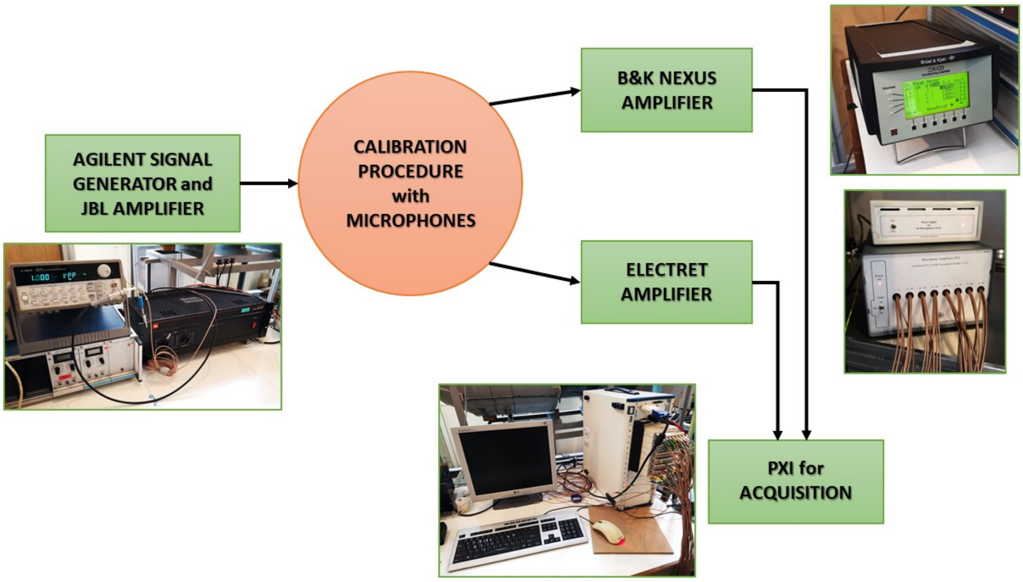

Figure 4.7: Acquisition chain for the acoustic signal detected by microphones involved in the calibration procedure.

4.1.3 Calibration chain

The proposed calibration is defined as a multi-step procedure, which aims to calculate the transfer function between a reference B&K microphone and the electret microphones embedded on the surface of the airfoil. First of all, as explained in Section 4.1.1, calibration is necessary to eliminate the resonance phenomena introduced by the pinhole configuration with which the microphones are installed in the airfoil model: the presence of cavities and channels generates some errors in the acquired electrical signals, which alter the measurement and also the final results. Furthermore, since the information reaches the PXI as signals expressed in Volt, by multiplying the transfer function of each step by the appropriate sensitivity values of the instruments, the final TF will have the V/Pa as the unit of measurement, which allows a transformation from electrical signals to real pressure values.

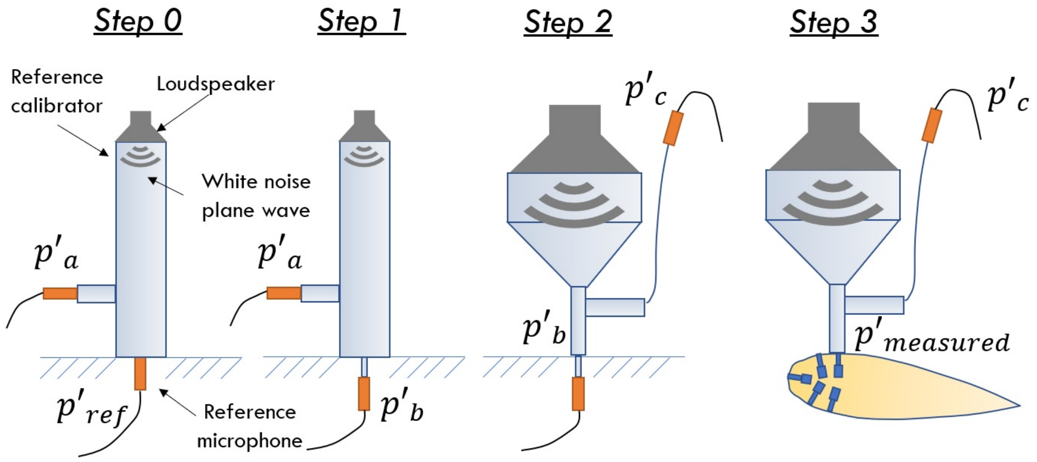

Figure 4.8: Sketch representing the different steps composing the calibration chain of the microphones embedded on the airfoil model. (Tamaro [44])

Being a preliminary work to the subsequent measurements in the wind tunnel, the calibration chain must be fast, robust and easily repeatable. Moreover, to minimize movements and any temperature changes that could affect the final result, the ideal would be to perform an in-situ calibration. These constraints introduce a high level of complexity, but they can be satisfied by the calibration chain implemented and shown in Figure 4.8.

The first thing to do is to set the characteristic parameters of the acoustic signal using the Agilent generator and the JBL amplifier: once the most suitable one has been chosen, it is sent to the loudspeaker positioned on the top of both calibrators, which emits the sound along the internal channel. In this way, both the side microphone and the one placed at the bottom of the cavity receive the signal and record it during acquisition. The first two steps involve the use of the cylindrical calibrator, which is first positioned above the reference B&K microphone flush-mounted on the calibration plate (step 0) and then moved to the other B&K microphone set up in a pinhole configuration always on the same calibration plate (step 1). However, in the last two steps, the conical calibrator is used for the same pinhole B&K microphone (step 2) and finally for the electret microphones embedded on the airfoil model (step 3), keeping it firmly in position through a mask designed for the insertion of the terminal part. The output signals from the various microphones pass through their respective amplifiers, before reaching the PXI where they are acquired using the *LabView* software managed by the user on the PC.

The calibration chain described above allows to calculate the final transfer function between the reference microphone and one of those embedded on the surface of the airfoil model, multiplying the terms that define the transfer functions of each step as shown by the following relation:

$$\underbrace{\frac{\cancel{fft(p'_a)}}{fft(p'_{ref})}}_{Step\ 0} \times \underbrace{\frac{\cancel{fft(p'_b)}}{\cancel{fft(p'_a)}}}_{Step\ 1} \times \underbrace{\frac{\cancel{fft(p'_c)}}{\cancel{fft(p'_b)}}}_{Step\ 2} \times \underbrace{\frac{fft(p'_{electret})}{\cancel{fft(p'_c)}}}_{Step\ 3} = \frac{fft(p'_{electret})}{fft(p'_{ref})} \tag{4.1}$$

As can be seen, each term representative of the transfer function is defined by the ratio between the fast Fourier transforms of the pressure fluctuations measured by the microphones involved in each step. Indeed, in analogy with Figure 4.8, p'_{ref} is the signal from the reference B&K microphone, p'_a is the signal from the side microphone on the cylindrical calibrator, p'_b is the signal from the microphone installed with the pinhole configuration, p'_c is the signal from the side microphone on the conical calibrator and finally, $p'_{electret}$ is the signal from the electret microphone embedded on the airfoil model. It is important to remember that the simplification of the terms can only occur under the assumption that the acoustic fields generated in each step are the same. Therefore, the first evaluation that must be done during the post-processing of the experimental data concerns the verification of this equality of the acoustic fields.

Regarding the present study, the choice of the best parameters for the calibration signal is made as a consequence of the analysis of the results obtained from several tests. The signal sent to the loudspeakers above the calibrators must excite a wide range of frequencies within the operating intervals of the microphones involved. One of the valid options tested in the laboratory corresponds to the white noise, which is characterized by the absence of periodicity over time and by the constant amplitude over a very wide frequency spectrum. The alternative is the use of sweep signals that are always continuous, but they have a frequency that varies linearly or logarithmically along one period, unlike what happens for white noise: for this type of acoustic signal, the initial and final value of the frequency testing range is established, as well as the time duration of a single period. The main advantage of the sweep is the ability to impose the alignment of the calibration signals between subsequent steps in the post-processing analysis, so that their coherence is maximized.

In this work, a linear sweep with a period of 3 s is used since the acquisition manages to converge within 30 s: a report of the final signal parameters, adopted for the realization of the results described in Section 4.2, are shown in Table 4.2. Moreover, the transfer functions are calculated using the *tfestimate* MATLAB function which again is based on the Welch method, since these quantities are defined as the ratio between the CPSD of the two signals Φ_{xy} and the PSD of the input, indicated with x:

$$TF(f) = \frac{\Phi_{xy}(f)}{\Phi_{xx}(f)} \tag{4.2}$$

This method consists of dividing the time series into overlapping segments over which the spectra are computed and averaged, in order to improve accuracy. The parameters used for the calculation of the transfer functions, in addition to the sampling frequency of 51200 Hz chosen during acquisition, include a number of samples equal to f_s multiplied by the duration time of the acoustic signal, windowed using the Hamming function with a 50% data overlap.

Table 4.2: Properties of calibration signal chosen for the microphones calibration procedure through a sensitivity analysis.

Parameter	**Value**
Type	Sweep
Mode	Linear
Start Frequency	100 Hz
Stop Frequency	15 kHz
Period	3 s
Acquisition Time	30 s

4.2 Results

This section reports and comments on all the results achieved from the calibration of the microphones embedded on the airfoil model, starting from the alignment of the signals up to the calculation of the complete transfer function according to Equation 4.1. The implemented calibration chain must provide a transfer function that removes the resonance phenomena related to microphones housing, following the theoretical trend predicted by the Bergh and Tijdeman model. As previously announced, the final result is not satisfactory yet and the problems encountered will be discussed below.

4.2.1 Alignment of signals

As mentioned in Section 4.1.3, the transfer function between the reference microphone and the electrets on the surface of the airfoil can be computed by multiplying the transfer functions relative to each step, as seen in Equation 4.1. The simplification of the terms involved can only occur if the acoustic field, generated in each step, is always the same. Therefore, this condition must be verified before proceeding with the multiplication, so that the procedure can be considered effectively correct. To check the equality of the acoustic fields, the cross-coherence function already adopted for the comparison between the surface-normal velocity and wall-pressure fluctuations is exploited. In this case, the *mscohere* MATLAB function is applied to the output signals from the Agilent generator; in particular, the analysis is repeated two by two, inserting the data acquired in two subsequent steps as input.

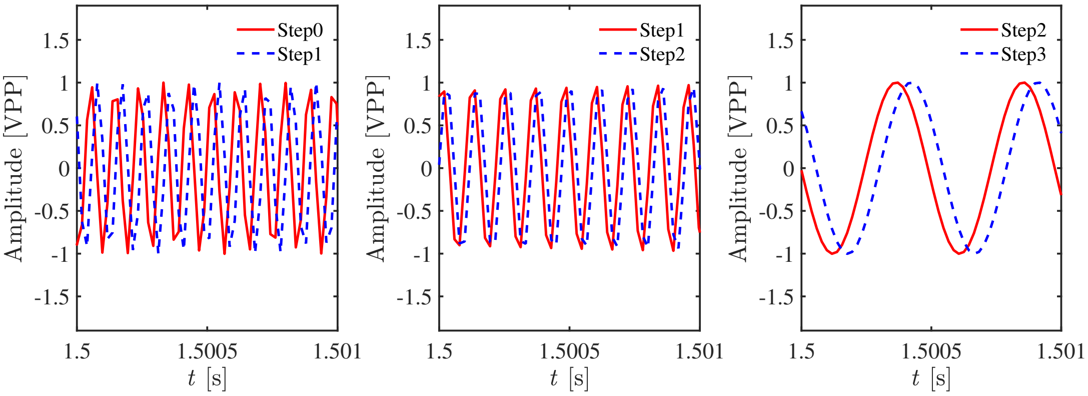

Figure 4.9: Time difference of the output signal from the Agilent generator between successive steps.

Figure 4.9 shows the voltage trends as a function of time, observing that the amplitude always varies between -1 and 1 VPP (Peak-to-Peak Voltage) as initially set in the signal generator. Each graph shows the comparison between the signals of two successive steps and, if the shape is approximately the same, in each of them there is a difference between the two curves which varies according to the case. The delay observed is due to the totally random time instant in which the data acquisition begins: the sweep signal covers a frequency range from 100 Hz up to 15 kHz, but the user is unable to start the acquisition always when the minimum frequency is listened to. Despite trying to select the same time instant, an error is always made and is reflected in the misalignment of the plotted signals.

If the cross-coherence is calculated using the original signals as they were acquired, the result obtained varies considerably and reaches the value 1 only for some frequencies, as shown in Figure 4.10. The unitary value indicates the equality of the acoustic fields produced by the loudspeakers in subsequent steps and the fact that it does not remain constant over the entire frequency range means that the necessary condition to be able to simplify the terms is not satisfied. Therefore, with the raw signals, it is not possible to proceed with the application of Equation 4.1. In order to solve this problem, it is necessary to align the signals of the Agilent generator between different steps, so that the curves overlap and the acquisition data processed by the *mscohere* function start at the same frequency.

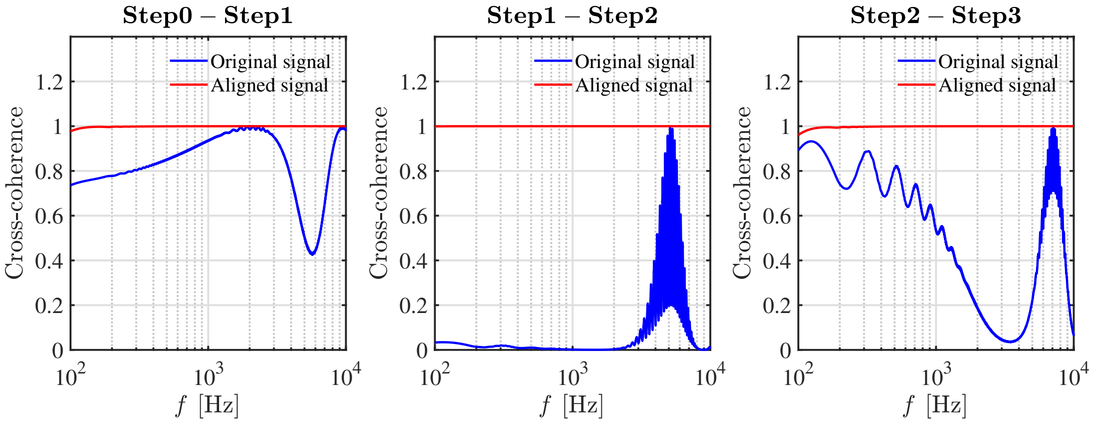

Figure 4.10: Cross-coherence of original (blue line) and aligned (red line) signals between successive steps. Thanks to the alignment operation, the cross-coherence improves tending towards the unitary value and eliminating the oscillations present in the original signals.

Once the initial frequencies are matched, the signals are aligned and their cross-coherence is equal to 1 over the entire frequency range considered, as observed in Figure 4.10. In conclusion, this improvement indicates that the calculation of the transfer functions of each step must be based on the aligned acquisition data to obtain terms which, multiplied together, can be simplified providing the final transfer function while respecting the equality between acoustic fields.

4.2.2 Single steps

Since the transfer functions of each step are required to calculate the final one between the reference B&K microphone and the electret microphones positioned along the surface of the airfoil model, the individual results are presented below to point out the peculiarities of these trends. The *tfestimate* MATLAB function used to compute these quantities returns a complex number, as the transfer function is characterized by both the absolute value and the phase. Since the calibration procedure with the same signal parameters has been repeated four times, for every step the transfer function absolute value and phase are plotted separately in terms of mean value and variance. The variance, indicated in grey, identifies an interval within which the data can deviate from its mean: if it does not stand out in the graphs, it means that the different measurements are almost identical and the step has a good repeatability.

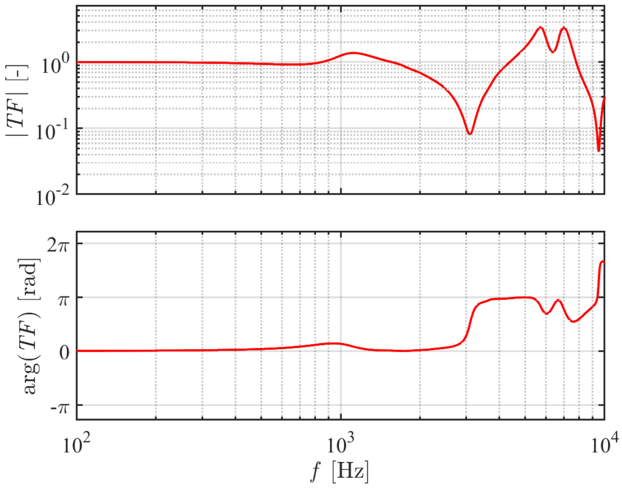

Figure 4.11: Transfer function between the reference microphone and the side one on the cylindrical calibrator. The mean value (red line) and the variance (grey area) computed from four different measures are plotted together to define the level of repeatability.

According to the sequence of the calibration chain, Figure 4.11 shows the transfer function trend of step 0, between the reference flush-mounted microphone installed on the calibration plate and the side one of the cylindrical calibrator. Both are B&K microphones with a 1/4 of an inch diameter and, consequently, their signal is processed by the Nexus amplifier before being acquired by the PXI. Analyzing the plotted trends, it is observed that both the absolute value and the phase do not show the variance interval, indicating a good correspondence of the results between the four acquisitions. Moreover, these parameters remain constant up to $f = 1$ kHz and then undergo significant variations: at a frequency of 3 kHz a drop occurs in the magnitude, which is reflected in a phase change from 0 to $+\pi$.

The result of step 1 corresponds to the transfer function between the side microphone of the cylindrical calibrator and another B&K microphone installed on the calibration plate through a pinhole cavity. This second device constitutes the element with which the conical calibrator, required for the microphones on the airfoil surface, is introduced in the next step. Figure 4.12 reports the trends of the absolute value and of the phase, which again show a full satisfaction of the repeatability criterion since the grey area seems negligible compared to the mean value. If compared with step 0, the trend shows opposite peaks in similar frequency ranges except for the anomalous drop which appears at 1 kHz, where a more constant value would be expected. This partial symmetry with the previous step is necessary for the opposite peaks to compensate each other with the final multiplication: remember that the trend of the complete transfer function should tend to the theoretical one predicted by the Bergh and Tijdeman model [7].

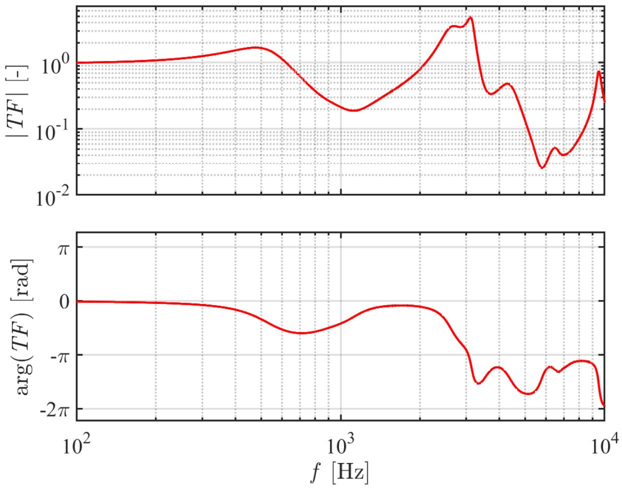

Figure 4.12: Transfer function between the side microphone on the cylindrical calibrator and the one installed on the calibration plate through a pinhole cavity. The mean value (red line) and the variance (grey area) computed from four different measures are plotted together to define the level of repeatability.

Figure 4.13 shows the transfer function of step 2 between the B&K microphone, mounted on the calibration plate through a pinhole, and the side one of the conical calibrator. In this case, both the absolute value and the phase feature a wider variance interval which represents a slightly lower level of repeatability than in the two previous steps. This problem can be linked to the instability of the conical calibrator once positioned on the calibration plate: the weight of the loudspeaker must be supported by the bottom part with a smaller diameter and finding the right position to keep it in balance is rather difficult. For the magnitude trend, around 1 kHz it is observed a growth of the signal that should compensate for the drop produced in the curve of step 1 at the same frequency range. Moreover, at $f \simeq 9$ kHz there is a significant decrease similar to that of step 0, in line with the theoretical result in Figure 4.3.

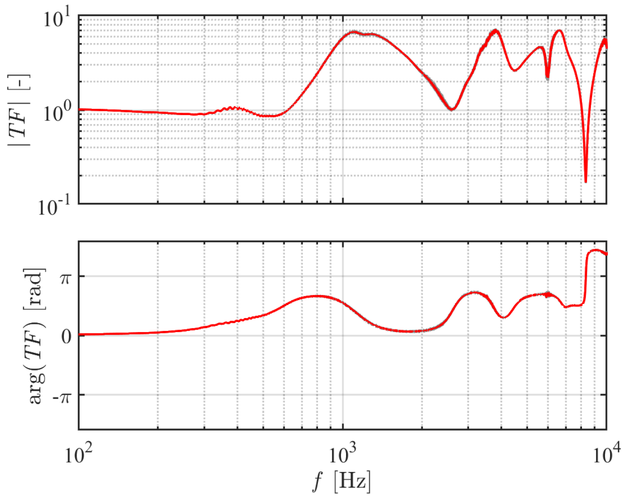

Figure 4.13: Transfer function between the microphone installed on the calibration plate through a pinhole cavity and the side one on the conical calibrator. The mean value (red line) and the variance (grey area) computed from four different measures are plotted together to define the level of repeatability.

Finally, step 3 is used to calculate the transfer function between the side B&K microphone of the conical calibrator and the electret microphones embedded on the surface of the airfoil: this procedure must be repeated 21 times, i.e. for each microphone in the model. In reality, it was not possible to acquire the electret signal positioned exactly at the stagnation point, as the calibrator must be manually supported during the measurement due to the impractical geometric configuration.

Figure 4.14 shows the result for one of the microphones located along the leading-edge curvature, where a greater uncertainty would be expected; instead, the absolute value and phase trends are not characterized by high variance. On the contrary, they demonstrate a high level of repeatability which confirms the reliability and robustness of this calibration chain: the transfer function of this step remains constant up to 3 kHz and then exhibits a clear peak at $f \simeq 9$ kHz. The fact that the trend appears so smooth along with the entire frequency range is linked to the good precision with which the microphone was centered by the corresponding hole created in the calibration mask.

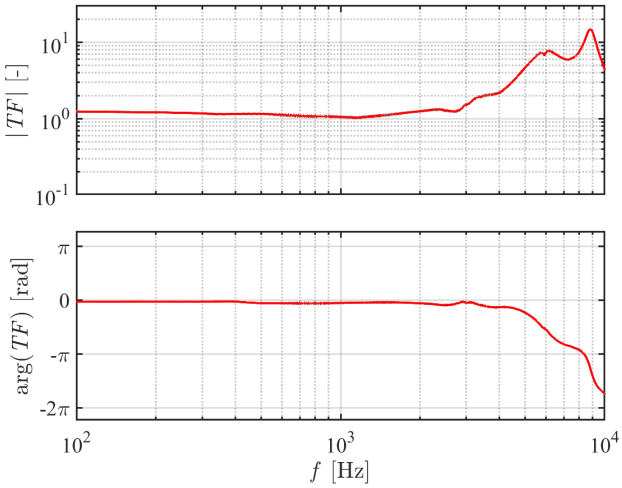

Figure 4.14: Transfer function between the side microphone on the conical calibrator and a microphone embedded on the surface of the airfoil model, positioned close to the stagnation point. The mean value (red line) and the variance (grey area) computed from four different measures are plotted together to define the level of repeatability.

4.2.3 Final Transfer Function

The separate analysis of the transfer functions of each step provides a general idea of the repeatability and shows the characteristics of these trends, which however must be compared together if a prediction of the final transfer function is desired. Indeed, since every contribution is multiplied with the others, the presence of symmetries between the various curves helps to compensate for the differences in order to tend to the theoretical result.

In Figure 4.15 all four calibration steps are plotted, always referring to the microphone along the leading-edge curvature considered above. It is possible to notice that many portions of a curve find a symmetric counterpart in the trend of another step with regards to the $|\mathrm{TF}| = 1$ line for the absolute value and $\arg(\mathrm{TF}) = 0$ rad for the phase: for example, around 1 kHz it seems that step 1 and step 2 have opposite peaks that once multiplied should cancel out and return a transfer function value close to 1, as expected. Similar behavior occurs at high frequencies where, exceeding the frequency of 2 kHz, all the curves increase with respect to the unit value of the magnitude, except for step 1 which presents an important drop.

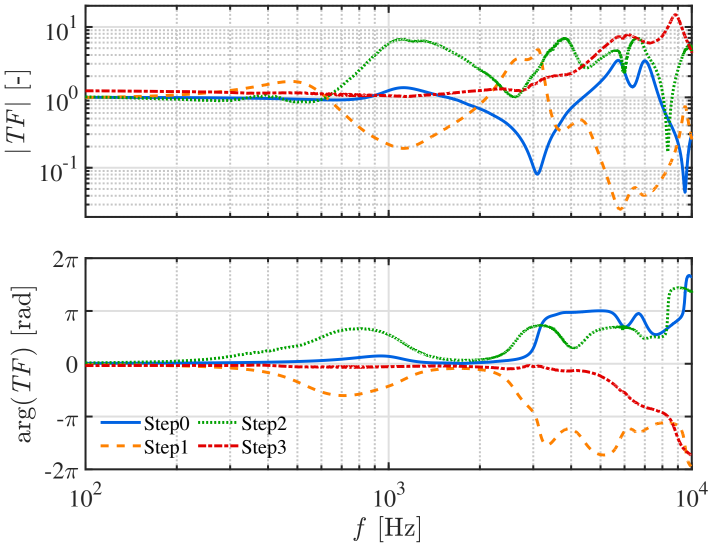

Figure 4.15: Transfer functions obtained in all the steps of the calibration chain.

The final result obtained by applying Equation 4.1 is plotted in Figure 4.16, comparing it with the theoretical trend computed according to the Bergh and Tijdeman model [7]. The estimation of the cavity frequency response is useful to provide an idea of how the final result should look like. From a direct comparison of the experimental transfer function with the theoretical estimation, it is possible to observe that from the multiplication process between the different steps the result achieved is characterized by many wiggles not present in the hypothetical trend.

The absolute value shows a first problem in the range between 400 and 800 Hz, where the curve, instead of remaining constant, undergoes an oscillation first upwards and then downwards, indicating that the trends of steps 1 and 2 have not completely compensated each other at those frequencies. Continuing to higher f values, it seems that the magnitude increases in line with the theoretical estimation, but the peak at 6 kHz is not noticed. On the contrary, a not negligible drop is created which, observing Figure 4.15, seems to be fed in particular by the step 0 and 2. Lastly, if after the peak the theoretical transfer function tends to decrease slowly up to $|\mathrm{TF}| = 1$, the experimental result is characterized by a sudden collapse at about 8 kHz which is quickly recovered before reaching $f = 10$ kHz. On the other hand, the phase trend appears more similar to the theoretical behavior, even if the slow decrease begins at higher frequencies since arg(TF) remains equal to 0 in a greater frequency range. The only significant difference occurs between 8 and 9 kHz where the experimental result goes from $-\pi$ to 0, instead of continuing towards the value of -2π.

However, the main issue remains linked to wiggles, which may be due to various aspects that do not allow the definition of a clear explanation. The doubt about the equality of the acoustic fields generated in each step has been resolved by the analysis in Section 4.2.1; therefore, it cannot be attributed as a possible cause of the problem. An attempt was also made by replacing the B&K microphone installed pinhole on the calibration plate with an electret microphone mounted on another device: obviously, the transfer functions of steps 1 and 2 change, but the final result obtained from the multiplication does not show improvements nor for the absolute value neither for the phase. The only solutions that could be implemented to solve the wiggles problem involve replacing the conical calibrator with another instrument that has greater stability when positioned on the microphones or the introduction of an additional step.

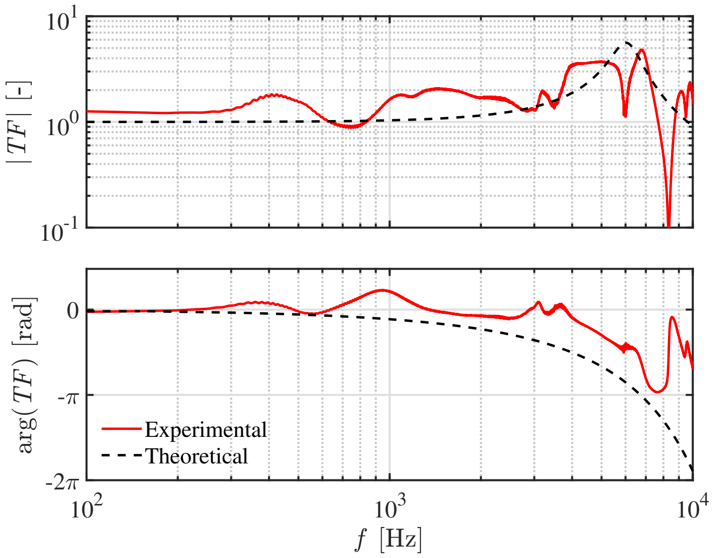

Figure 4.16: Transfer function between the reference microphone and microphone 21 on the surface of the airfoil model, obtained by multiplying all the intermediate steps. The experimental trend (red line) is compared with Bergh and Tijdeman theoretical model (dashed black line), based on geometrical parameters.

Since the problems seem to lie mainly in the use of the conical calibrator, it is calculated the contribution of this instrument by multiplying the transfer functions of the two steps in which it is involved. The operation has been repeated for the 10 microphones positioned along with one of the airfoil sides and their results are shown in Figure 4.17: the trends represent the transfer functions between the B&K microphone installed pinhole and the electret embedded on the surface. From the graph, it can be seen that the curves are all similar to each other, with the only exception of the mic 22 response which has higher values. Moreover, for mic 28 and 29 there is a disturbance around 800 Hz in the results of both magnitude and phase, probably due to background noise. The trends are characterized by strong oscillations and applying a theoretical prediction to identify how the correct shape should be is inconvenient.

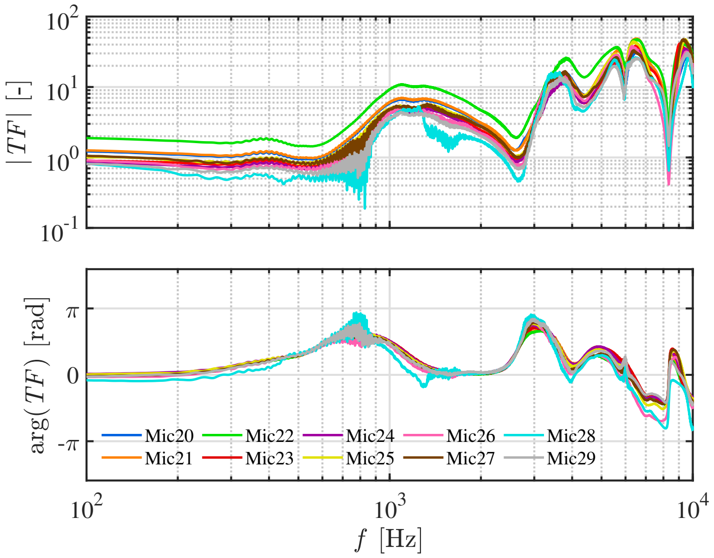

Figure 4.17: Transfer function between the microphones embedded on one of the airfoil model sides and the one installed on the calibration plate through a pinhole cavity, obtained by multiplying steps 2 and 3.

Chapter 5

Conclusions and future work

The present study, carried out during the internship period at the von Karman Institute for Fluid Dynamics in Brussels, aims to investigate the effects of porosity on a NACA-0024 wing profile immersed in a turbulent flow.

From the interaction between a body and the vortical structures of the incoming flow, a partial conversion of kinetic energy into sound occurs, which radiates throughout the surrounding motion field. The turbulence-interaction noise, generated by the distortion of the eddies approaching the surface, is a problem that recurs in many industrial applications and numerous researches have been developed in recent years to explain this phenomenology and find an adequate solution. In the particular case of an airfoil, the sound emitted at the leading-edge is the predominant one when the flow is strongly turbulent and the strategies proposed for its attenuation are various, such as the structural modification of the leading-edge shape or the introduction of porous media in the internal volume. The current investigation focuses on the latter solution, which from previous studies shows promising results: indeed, far-field noise mitigation was observed both numerically and experimentally testing several airfoil models, where porous treatments were implemented. At the moment, however, the physical mechanism responsible for the leading-edge noise reduction has not been identified yet and this represents the first challenge faced in the discussion.

A possible explanation has been provided by Zamponi et al. [50], who hypothesized the relation between the radiated sound attenuation and the variation in turbulence distortion due to porosity. Since this assumption has not been demonstrated, the main purpose of the present study is to find the link between these two phenomena, in order to give for the first time a definitive explanation of the physical noise mitigation mechanism. The investigation is divided into two parts, one numerical and the other experimental, both focused on the analysis of wall-pressure fluctuations as they are considered responsible for the dominant dipolar source according to Curle's analogy [10].

The numerical study involves the post-processing activity carried out on the pressure and velocity data, obtained through large-eddy simulations by a research group of the RWTH Aachen University. The simulations are based on the same experimental setup designed and already implemented at VKI for the previous work of Zamponi et al. [50], characterized by a rod-airfoil configuration for the generation of the incoming turbulent flow: the same setting is repeated both for the solid airfoil version and for the one on which the porous treatment is applied. From the analysis of the unsteady wall-pressure fluctuations, a strong reduction is observed for the porous case in the area of maximum p'_{rms}, which is not located exactly at the stagnation point. The calculation of the spatial coherence along with the $y = 0.17d$ coordinate of the surface shows how, in the porous case, the pressure fluctuations lose their coherence more rapidly than the solid one around the vortex-shedding frequency: this suggests that turbulent flow structures are less coherent in the spanwise direction due to porosity. Moreover, reproducing on the surface of the airfoil the distribution of the pressure fluctuations phase, a greater variation is evident for the porous configuration. This trend induces a more intense destructive phase interference, which is reflected in the mitigation of the radiated sound.

From the LES data on the midspan plane, the maps of the three velocity components in the stagnation region were plotted, evaluating both the mean value and the fluctuations. Since the flow can partially penetrate inside the porous airfoil structure, there are clear differences with the motion field around the solid NACA-0024 wing profile. In particular, the reduction experienced by the fluctuating upwash velocity component in the presence of porosity indicates an attenuation of the turbulence distortion process, responsible for the leading-edge noise production of noise, according to Amiet's theory [2]. Furthermore, by calculating the vorticity as the rotor of the velocity vector, it was possible to compare the distribution of this quantity along the leading-edge of the two airfoils: it emerged that, given the higher boundary layer thickness induced by the porous treatment, the mean vorticity is spread over a wider region than in the solid case.

The most important post-processing analysis is related to the comparison between the PSDs of the velocity fluctuations and those of the wall-pressure fluctuations. Indeed, from the spectra of u', v' and p', a significant reduction is observed in the low-frequency range for the simulation with porous configuration, especially in the two positions downstream of the leading-edge. Around the vortex-shedding peak estimated at $St = 0.2$, the attenuation of the emitted sound is about 6 dB and the fact that it occurs at the same frequency as the velocity components mitigation indicates the presence of a relation between the noise reduction and the distortion variation of the turbulent vortices. The link, that demonstrates the turbulence distortion attenuation as the leading-edge noise reduction mechanism using porous materials, was found by calculating the velocity component normal to the surface of the wing profile. This quantity is the one that most closely resembles the pressure, as both act in the direction perpendicular to the surface: indeed, from the comparison between the respective power spectra, a similar attenuation emerges in the same low-frequency range which confirms the above hypothesis. Therefore, after verifying that the insertion of porosity in the airfoil structure determines a variation of the distortion suffered by the eddies approaching the surface, for the first time it is numerically demonstrated that this phenomenon constitutes one of the physical leading-edge noise mitigation mechanisms.

Despite this important discovery, many other aspects related to turbulence-interaction noise have remained unclear and require further research to be investigated. First of all, it would be interesting to evaluate the position and the intensity of the dipole distribution along the surface of the airfoils, being the dominant acoustic source according to Curle's analogy [10]. Furthermore, in future studies it would be necessary to verify the effective contribution of the monopolar source for the porous configuration: since the velocity does not completely cancel out on the surface due to the flow penetration into the pores, it is not certain that the term that appears in Curle's equation is negligible. Eventually, given the wall-pressure fluctuations data, it would be useful to implement Amiet's theory [2] to predict the far-field noise.

As regards the experimental activity carried out in the VKI facility, the ultimate goal concerns the evaluation of the unsteady wall-pressure fluctuations on a NACA-0024 wing profile immersed in a turbulent flow. The experimental setup involves two airfoil models on whose surface a series of microphones have been mounted for the detection of pressure fluctuations. The models have the same dimensions, but the porous one is made with melamine foam covered with a hard plastic exoskeleton to maintain the shape during the tests. A solid centerplane has been installed in the center of the inner volume to avoid cross-flow that would deteriorate the aerodynamic characteristics. Since cavities are manufactured on the surface for the microphones housing, their contribution can generate resonance phenomena that must be eliminated in order not to pollute the acoustic signals; for this reason, it is necessary to calibrate these microphones before the acquisitions in the wind tunnel.

The calibration chain implemented at VKI consists of four subsequent steps and is used to calculate the transfer function between a reference microphone and those embedded on the surface of the airfoil model. Each step involves the use of other additional microphones and the individual TFs are then multiplied with each other to obtain the final one, through a simplification that assumes the equality of the acoustic fields between the different steps. Despite the alignment of the acquired signals in order to respect the necessary condition for this simplification, the results show evident problems in the procedure, as the transfer functions are characterized by strong fluctuations and deviate from the theoretical trend predicted by the Bergh and Tijdeman model [7]. The complete transfer functions obtained are not smooth enough to be applied in quantitative analysis and for this reason, it was not possible to continue with the experimental campaign, testing the airfoil models in the wind tunnel.

In order to overcome the limitations encountered in this investigation, it is necessary to obtain less fluctuating trends from the calibration. Actually, the implemented procedure provides promising results in terms of repeatability and robustness, in addition to the fact that it is easily applicable in-situ; therefore, the problem is to be found in the instrumentation used. A solution that could be tested in future studies concerns the integration of an additional step, which facilitates the cancellation of intermediate terms in the multiplication of transfer functions. The other option involves replacing the conical calibrator, used in the last two steps of the calibration chain, with a similar device that has greater stability during acquisition: indeed, the shape and weight of the conical calibrator together with the loudspeaker do not currently allow a reliable measurement of the acoustic signals for the microphone positioned in the stagnation point. In the future, the refinement of the calibration procedure will allow performing innovative experimental campaigns on solid and porous airfoil models to inspect the unsteady wall-pressure fluctuations.

Bibliography

[1] B.R. Agrawal and A. Sharma. Numerical analysis of aerodynamic noise mitigation via leading edge serrations for a rod-airfoil configuration. *International Journal of Aeroacoustics*, 15:734-756, 2016.

[2] R.K. Amiet. Acoustic radiation from an airfoil in a turbulent stream. *Journal of Sound and Vibration*, 41:407-420, 1975.

[3] F. Avallone, D. Casalino and D. Ragni. Impingement of a propeller-slipstream on a leading edge with a flow-permeable insert: a computational aeroacoustic study. *International Journal of Aeroacoustics*, 17:687-711, 2018.

[4] L.J. Ayton, M.J. Colbrook, T. Geyer, P. Chaitanya and E. Sarradj. Reducing aerofoil-turbulence interaction noise through chordwise-varying porosity. *Journal of Fluid Mechanics*, 906, 2021.

[5] G. Bampanis and M. Roger. On the turbulence-impingement noise of a NACA-12 airfoil with porous inclusions. In *26th AIAA/CEAS Aeroacoustics Conference*, Virtual event, June 2020.

[6] P.W. Bearman. Some measurements of the distortion of turbulence approaching a two-dimensional bluff body. *Journal of Fluid Mechanics*, 53, 1972.

[7] H. Bergh and H. Tijdeman. Theoretical and experimental results for the dynamic response of pressure measuring systems. Technical Report NLR-TR F.238, National Aeronautical and Astronautical Research Institute, 1965.

[8] J. Boudet, N. Grosjean and M.C. Jacob. Wake-airfoil interaction as broadband noise source: a large-eddy simulation study. *International Journal of Aeroacoustics*, 4:93-116, 2005.

[9] P. Chaitanya, P. Joseph, T.P. Chong, M. Priddin and L.J. Ayton. On the noise reduction mechanisms of porous aerofoil leading edges. *Journal of Sound and Vibration*, 485, 2020.

[10] N. Curle. The influence of solid boundaries upon aerodynamic sound. *Proceedings of the Royal Society of London. Series A, Mathematical and Physical Sciences*, 231:505-514, 1955.

[11] L.D. de Santana, C. Schram and W. Desmet. An experimental procedure for the determination of wake-airfoil interaction noise parameters. In *19th AIAA/CEAS Aeroacoustic Conference*, Germany, May 2013.

[12] L.D. de Santana, J. Christophe, C. Schram and W. Desmet. A Rapid Distortion Theory modified turbulence spectra for semi-analytical airfoil noise prediction. *Journal of Sound and Vibration*, 383:349-363, 2016.

[13] W.J. Devenport, J.K. Staubs and S.A. Glegg. Sound radiation from real airfoils in turbulence. *Journal of Sound and Vibration*, 329:3470-3483, 2010.

[14] T. Geyer, E. Sarradj and J. Giesler. Application of a beamforming technique to the measurement of airfoil leading edge noise. *Advances in Acoustics and Vibration*, 1-16, 2012.

[15] T.F. Geyer, A. Lucius, M. Schrödter, M. Schneider and E. Sarradj. Reduction of turbulence interaction noise through airfoils with perforated leading edges. *Acta Acustica united with Acustica*, 105:109-122, 2019.

[16] J. Gill, X. Zhang and P. Joseph. Symmetric airfoil geometry effects on leading edge noise. *The Journal of the Acoustical Society of America*, 134:2669-2680, 2013.

[17] L. Graftieaux, M. Michard and N. Grosjean. Combining PIV, POD and vortex identification algorithms for the study of unsteady turbulent swirling flows. *Measurement Science and Technology*, 12:1422-1429, 2001.

[18] A. Henning, L. Koop and K. Ehrenfried. Causality correlation in aeroacoustic experiments by means of simultaneous PIV and microphone-array measurements. In *Berlin Beamforming Conference*, Germany, February 2010.

[19] A. Henning, L. Koop, K. Ehrenfried, A. Lauterbach and S. Kroebery. Simultaneous multiplane PIV and microphone-array measurements on a rod-airfoil configuration. In *15th AIAA/CEAS Aeroacoustic Conference*, Germany, May 2009.

[20] A. Hirschberg. Introduction to aero-acoustics of internal flows. *Basics of Aeroacoustics and Thermoacoustics*, Lecture series 2007-09, von Karman Institute for Fluid Dynamics, 2007.

[21] J.C.R. Hunt. A theory of turbulent flow round two-dimensional bluff bodies. *Journal of Fluid Mechanics*, 61:625-706, 1973.

[22] M.C. Jacob, J. Boudet, D. Casalino and M. Michard. A rod-airfoil experiment as benchmark for broadband noise modeling. *Theoretical and Computational Fluid Dynamics*, 19:171-196, 2005.

[23] D. Kim, G.S. Lee and C. Cheong. Inflow broadband noise from an isolated symmetric airfoil interacting with incident turbulence. *Journal of Fluids and Structures*, 55:428-450, 2015.

[24] J.W. Kim, S. Haeri and P.F. Joseph. On the reduction of aerofoil-turbulence interaction noise associated with wavy leading edges. *Journal of Fluid Mechanics*, 792:526-552, 2016.

[25] R.A. Kroeger, H.D. Grushka and T.C. Helvey. Low speed aerodynamics for ultra-quiet flight. Technical Report AD893426, Air force flight dynamics laboratory Wright-Patterson Air Force Base, Ohio, 1972.

[26] M. Kuczmarski and J. Johnston. Acoustic absorption in porous materials. Technical Report NASA/TM-2011-216995, NASA Glenn Research Center, 2011.

[27] S. Lee. Reduction of blade-vortex interaction noise through porous leading edge. *AIAA Journal*, 32:480-488, 1994.

[28] M.J. Lighthill. On sound generated aerodynamically I. General theory. *Proceedings of the Royal Society of London. Series A, Mathematical and Physical Sciences*, 211:564-587, 1952.

[29] R. Maryami, S.A. Showkat Ali, M. Azarpeyvand and A. Afshari. Turbulent flow interaction with a circular cylinder. *Physics of Fluids*, 32, 2020.

[30] P.F. Mish and W.J. Devenport. An experimental investigation of unsteady surface pressure on an airfoil in turbulence-Part 1: Effects of mean loading. *Journal of Sound and Vibration*, 296:417-446, 2006.

[31] S. Moreau and M. Roger. Effect of angle of attack and airfoil shape on turbulence-interaction noise. In *11th AIAA/CEAS Aeroacoustics Conference*, California, May 2004.

[32] S. Moreau and M. Roger. Back-scattering correction and further extensions of Amiet's trailing-edge noise model. Part 2: application. *Journal of Sound and Vibration*, 323:397-425, 2009.

[33] S. Oerlemans and P. Migliore. Aeroacoustic wind tunnel tests of wind turbine airfoils. In *10th AIAA/CEAS Aeroacoustics Conference*, United Kingdom, 2004.

[34] W. Olsen and J. Wagner. Effect of thickness on airfoil surface noise. *AIAA Journal*, 20:437-439, 1982.

[35] R. Paterson and R. Amiet. Acoustic radiation and surface pressure characteristics of an airfoil due to incident turbulence. In *3rd Aeroacoustics Conference*, California, July 1976.

[36] G.K. Batchelor and I. Proudman. The effect of rapid distortion of a fluid in turbulent motion. *The Quarterly Journal of Mechanics and Applied Mathematics*, 7:83-103, 1954.

[37] M. Roger and S. Moreau. Back-scattering correction and further extensions of Amiet's trailing-edge noise model. Part 1: theory. *Journal of Sound and Vibration*, 286:477-506, 2005.

[38] M. Roger, C. Schram and L. De Santana. Reduction of airfoil turbulence-impingement noise by means of leading-edge serrations and/or porous material. In *19th AIAA/CEAS Aeroacoustic Conference*, Germany, May 2013.

[39] M. Roger and S. Moreau. Airfoil turbulence-impingement noise reduction by porosity or wavy leading-edge cut: experimental investigations. In *45th International Congress and Exposition on Noise Control Engineering*, Germany, August 2016.

[40] E. Sarradj and T. Geyer. Noise generation by porous airfoils. In *13th AIAA/CEAS Aeroacoustics Conference*, Italy, May 2007.

[41] E. Sarradj and T. Geyer. Symbolic regression modeling of noise generation at porous airfoils. *Journal of Sound and Vibration*, 333:3189-3202, 2014.

[42] S. Satcunanathan, M.H. Meinke and W. Schröder. Prediction of noise mitigation by porous media based on a direct-hybrid CFD/CAA method. In *25th AIAA/CEAS Aeroacoustics Conference*, The Netherlands, 2019.

[43] T. Sinnige, B. Della Corte, R. De Vries, F. Avallone, R. Merino-Martínez, D. Ragni, G. Eitelberg and L.L.M. Veldhuis. Alleviation of propeller-slipstream-induced unsteady pylon loading by a flow-permeable leading edge. *Journal of Aircraft*, 56:1-17, 2019.

[44] S. Tamaro. Experimental investigation of the interaction between turbulence and a porous surface in the framework of leading-edge noise mitigation. Project Report 2020-26, von Karman Institute for Fluid Dynamics, 2020.

[45] Z. Taylor, J. Nieto and D. Johnson. Multi-modal sensor calibration using a gradient orientation measure. *Journal of Field Robotics*, 32:675-695, 2015.

[46] F. Tong, W. Qiao, W. Chen, H. Cheng, R. Wei and X. Wang. Numerical analysis of broadband noise reduction with wavy leading edge. *Chinese Journal of Aeronautics*, 31:1489-1505, 2018.

[47] N. Van de Wyer, A. Zapata, D. Nogueira and C. Schram. Development of a test rig for the measurement of turbulent boundary layer wall pressure statistics. In *2018 AIAA/CEAS Aeroacoustics Conference*, Georgia, June 2018.

[48] M. Wang, S. Moreau, G. Iaccarino and M. Roger. LES prediction of wall-pressure fluctuations and noise of a low-speed airfoil. *The Journal of the Acoustical Society of America*, 8:177-198, 2009.

[49] R. Zamponi, D. Ragni, N. Van de Wyer and C. Schram. Experimental investigation of airfoil turbulence-impingement noise reduction using porous treatment. In *25th AIAA/CEAS Aeroacoustics Conference*, The Netherlands, 2019.

[50] R. Zamponi, S. Satcunanathan, S. Moreau, D. Ragni, M. Meinke, W. Schröder and C. Schram. On the role of turbulence distortion on leading-edge noise reduction by means of porosity. *Journal of Sound and Vibration*, 485, 2020.